Dendrite branching receptor HPO-30 uses two novel mechanisms to regulate actin cytoskeletal remodeling

Daniel A. Kramer[1], Heidy Y. Narvaez-Ortiz[2], Rebecca Shi[3,4], Kang Shen[3,5], Julien Roche[1], Brad J. Nolen[2], and Baoyu Chen[1#]

Affiliations:

[1]Roy J Carver Department of Biochemistry, Biophysics, and Molecular Biology, Iowa State University, Ames, IA 50014, USA.

[2]Department of Chemistry and Biochemistry, Institute of Molecular Biology, University of Oregon, Eugene, OR 97403, USA.

[3]Department of Biology, Stanford University, Stanford, CA, 94305, USA

[4]Neurosciences IDP, Stanford University, Stanford, CA, 94305, USA

[5]Howard Hughes Medical Institute, Stanford University, Stanford, CA, 94305, USA

[#]Correspondence to: stone@iastate.edu

Abstract

Dendrite morphogenesis is essential to neural circuit formation, but the molecular mechanisms controlling the growth of complicated dendrite branches are not well understood. Prior studies using the highly branched *C. elegans* PVD sensory neuron identified a membrane co-receptor complex that transmits extracellular cues to intracellular actin remodeling machinery to promote high-order dendrite branching. In this complex, the transmembrane protein HPO-30 recruits the WAVE regulatory complex (WRC) from the cytosol to dendrite branching sites, where WRC stimulates the Arp2/3 complex to polymerize actin. Here we report biochemical and structural characterization of this interaction, revealing that the intracellular domain (ICD) of HPO-30 uses two novel mechanisms to regulate the actin cytoskeleton. First, the unstructured HPO-30 ICD likely undergoes dimerization and induced folding to bind the WRC, with the binding simultaneously promoting WRC activation by the GTPase Rac1. Second, the dimerized HPO-30 ICD directly binds to both the sides and barbed end of actin filaments. The barbed end binding activity resembles that of the actin capping protein CapZ and prevents both actin polymerization and depolymerization. The novel dual functions of this dendrite receptor provide an intriguing model of how membrane proteins can use distinct mechanisms to fine-tune local actin dynamics.

Introduction

While neurons have vastly different shapes, they all share a similar architecture—one cell body, a long primary axon, and many branching protuberances called dendrites, along which are numerous micron-sized projections called spines (Burianek and Soderling, 2013; Jan and Jan, 2003; Lefebvre et al., 2015). The formation of dendrites and spines is critical for the development of the nervous system, as they form the majority of post-synaptic connections in animals and directly determine the complex wiring of neural circuits (Hotulainen and Hoogenraad, 2010; Scott and Luo, 2001; Tavosanis, 2012). Dendrite development requires actin and microtubule filaments to drive the initiation and outgrowth of newly formed neurites (Cheng and Poo, 2012; Zhao et al., 2017). Defects in actin cytoskeletal regulation alter dendrite morphology and neural connections and contribute to many neurodevelopmental disorders, such as autism, mental retardation, and schizophrenia (Yan et al., 2016).

A central mechanism by which neurons control actin polymerization is through the Arp2/3 complex, a seven-protein complex that binds to the sides of existing actin filaments and initiates the formation of branched actin filament networks (Goley and Welch, 2006; Machesky et al., 1994; Pollard, 2007). Intrinsically inactive, the Arp2/3 complex requires activation by a group of proteins called nucleation promoting factors (NPFs). The Wiskott-Aldrich Syndrome Protein (WASP) family proteins are a major group of NPFs (Alekhina et al., 2017; Kramer et al., 2022; Pollitt and Insall, 2009; Takenawa and Suetsugu, 2007). They all contain a conserved WCA (WH2-central-acidic) sequence at their C terminus, which can directly bind to and activate Arp2/3, while their N-terminal sequences vary greatly and define their regulatory mechanism and cellular function (Alekhina et al., 2017; Kramer et al., 2022; Machesky and Insall, 1998).

Among the WASP-family proteins, WAVE (Wiskott-Aldrich Verprolin homology) exists in a multi-protein complex named the WAVE regulatory complex (WRC), which contains five subunits: Sra1, Nap1, Abi2, HSPC300, and WAVE (or their corresponding orthologs in vertebrates) (Chen et al., 2010; Eden et al., 2002; Gautreau et al., 2004; Polesskaya et al., 2021; Rottner et al., 2021). Enriched in neurons, the WRC and Arp2/3 complex promote actin polymerization downstream of membrane signaling to drive various neuronal activities, including growth cone formation, axon branching, dendrite branching, synapse formation, and axon guidance and projection (Chia et al., 2014; Chou and Wang, 2016; Pilpel and Segal, 2005; Racz and Weinberg, 2008; Soderling et al., 2007; Stephan et al., 2011; Tahirovic et al., 2010;

Yamazaki et al., 2005; Yokoyama et al., 2011). Disrupting the WRC in animals profoundly impacts the nervous system, leading to altered spine morphology and density, intellectual disability, as well as embryonic death (Dahl et al., 2003; Soderling et al., 2003). Mutations in WAVE and other subunits of the WRC lead to a variety of neurodevelopmental disorders in human patients, including neurodevelopmental disorder with absent language and variable seizures (NEDALVS), developmental and epileptic encephalopathy-65 (DEE-65), and Alzheimer's disease (Begemann et al., 2021; Conway et al., 2018; Ito et al., 2018; Kirkpatrick et al., 2017; Kramer et al., 2022; Kumar et al., 2013; Olive et al., 2020; Rottner et al., 2021; Shimojima Yamamoto et al., 2021; Sims et al., 2017; Srivastava et al., 2021; Zhao et al., 2021; Zweier et al., 2019).

The WRC keeps WAVE basally inhibited by sequestering its C-terminal WCA to a conserved surface formed by both the Sra1 and WAVE subunits (Chen et al., 2017, 2010a; Eden et al., 2002; Kramer et al., 2022) . Through direct interactions, various molecules can recruit the WRC to the membrane and/or simultaneously activate it, which releases the WCA to promote Arp2/3-mediated actin polymerization. These ligands include small GTPases (e.g., Rac1 and Arf), acidic phospholipids (e.g., PIP_3), various adaptor proteins, and over 100 different membrane proteins that contain a 6 amino acid peptide motif named the WIRS motif (WRC interacting receptor sequence, defined as Φ-x-T/S-F-x-x, where Φ is a bulky hydrophobic residue and x is any residues) (Chen et al., 2017, 2014a, 2010a; Eden et al., 2002; Kobayashi et al., 1998; Koronakis et al., 2011; Lebensohn and Kirschner, 2009; Rottner et al., 2021). Many WIRS-containing membrane proteins, such as SYG-1, Robo, Neogenin, TMEM132, neuroligins, and various protocadherins, are important neuronal receptors and have been shown to rely on the WIRS-WRC interaction to regulate various processes in neural development (Chaudhari et al., 2021; Chia et al., 2014; Fan et al., 2018; Lee et al., 2016; Wang et al., 2021; Xing et al., 2018).

Previous studies identified the claudin-like dendrite receptor HPO-30 as a novel WRC binding protein, and this interaction was essential to higher-order dendrite branching. HPO-30 acts as a co-receptor of the cell adhesion molecule DMA-1 in the PVD sensory neuron in *C. elegans*. The extracellular domain of DMA-1 forms a multi-ligand complex with the secreted protein LECT-2 and the extracellular domains of the epidermis cell receptors SAX-7 and MNR-1 (Zou et al., 2016). These interactions provide the spatial cue for initiating dendrite branching (Dong et al., 2013; Zou et al., 2016, 2018). The intracellular domain (ICD) of HPO-30 directly

binds the WRC, while the ICD of DMA-1 binds the Rac guanine nucleotide exchange factor (GEF) TIAM-1, which can increase the local concentration of activated Rac1—the canonical activator of WRC (Tang et al., 2019). Together, HPO-30 and DMA-1 organize a multi-protein complex to spatiotemporally coordinate extracellular cues with the intracellular actin remodeling essential to high-order dendrite branching (Zou et al., 2018).

It is unclear how the HPO-30 ICD interacts with the WRC. It is also unknown if, in addition to binding to the WRC, the HPO-30 ICD has other functions. The HPO-30 ICD does not contain a WIRS motif and must use a non-WIRS mechanism to interact with the WRC. Previous studies showed that deleting the C-terminal part of the HPO-30 ICD strongly affected WRC binding *in vitro* and high-order dendrite branching *in vivo*, but it was unclear whether the HPO-30 ICD used a linear peptide motif analogous to WIRS to bind the WRC (Zou et al., 2018). Furthermore, although HPO-30 is homologous to the tight junction claudin proteins in mammals, its ICD sequence is only conserved in nematode worms. Nevertheless, this ICD binds to both *C. elegans* and human WRC, suggesting that the interaction mechanism is conserved in other animals (Zou et al., 2018). It is likely that humans have an unidentified membrane protein that uses the same interaction surface to regulate the WRC. Thus, it is important to understand the mechanism underlying the interaction between HPO-30 and WRC.

Here we report biochemical and structural analysis of the HPO-30-WRC interaction. We find that, unlike other WRC-interacting receptors known to date, the HPO-30 ICD requires dimerization and folding into a three-dimensional structure to bind the WRC. Furthermore, to our surprise, we find the HPO-30 ICD directly interacts with actin filaments, also in a dimerization-dependent manner. The dimeric form binds to both the side and barbed end of actin filaments and inhibits both actin polymerization and depolymerization, resembling the activity of the actin capping protein CapZ. The dual activities of HPO-30 ICD provide an intriguing example of how a membrane receptor can regulate actin dynamics by simultaneously controlling the localization of a central actin nucleation factor and modulating local actin networks to promote an important biological process.

Results

HPO-30 ICD may use a folded structure, instead of a short peptide motif, to bind the WRC

The HPO-30 ICD (or ICD for short hereafter) does not contain a WIRS motif. Therefore, we first hypothesized it might use a distinct linear motif to bind the WRC. To identify this sequence motif, we mutated every five residues to alanine throughout the ICD and used GST pull-down assays to evaluate how they disrupted WRC binding (**Figure 1A**). Interestingly, we found that mutating nearly any five amino acids (a.a.), except for the fourth and tenth region, significantly reduced the binding to WRC, with the middle region of the ICD showing the strongest effect (Δ5, 6, 7 in **Figure 1A,B**, lanes 7-9). This is consistent with the previous qualitative data obtained in a less ideal pull-down condition (Zou et al., 2018). It was intriguing that none of these 5-a.a. mutations completely abolished the binding to WRC, unlike WIRS-mediated binding, where mutating the WIRS motif readily diminished the interaction (Chen et al., 2014a). This is consistent with our quantitative measurement of the binding affinity using equilibrium pull-down (EPD) assays, in which the wild type (WT) ICD had a dissociation constant (K_D) of ~1.69 μM (**Figure 1D,** black). Alanine mutant Δ5, which had the strongest effect in the non-equilibrium pull-down assays (**Figure 1A,B,** lane 7), increased the K_D only mildly to ~5.06 μM, still maintaining significant binding (**Figure 1D**, purple) (Chen et al., 2017; Kuzmic, 1996; Pollard, 2010). By contrast, replacing either the entire N-terminal or C-terminal sequences, or two consecutive 5-a.a. mutations with a (GGS) sequence almost completely abolished the binding (**Figure 1A,C** Δ11-14). Note that while most mutants contain a GST-tag at the N-terminus, the 5-a.a. mutations located at the C-terminus of the ICD contain a GST-tag at the C-terminus (Δ8-10 in **Figure 1**, lanes 10-13 in **Figure 1B**), which we found was necessary to protect the mutant ICDs from degradation (data not shown).

Nearly all of the 5-a.a. alanine scan mutants affected WRC binding. This is distinct from WIRS-containing proteins, where only mutations in the WIRS motif disrupted binding (Chen et al., 2014a). We hypothesized that, instead of using a short linear peptide motif like WIRS, either the HPO-30 ICD folds into a three-dimensional structure and uses the folded structure to bind the WRC, or the entire sequence binds as a long linear peptide that interacts extensively with the WRC. We favor the first hypothesis because it is supported by both secondary structure analysis from various programs, including JPred, PredictProtein, PSIPred, and SABLE, and *ab initio* tertiary structure prediction by many different algorithms, including LOMETS, QUACK,

RaptorX, Rosetta, AlphaFold 2.0, and RoseTTAFold, (**Figure 1E; Figure 1—figure supplement 1)** (Adamczak et al., 2004; Bernhofer et al., 2021; Bonneau et al., 2001; Drozdetskiy et al., 2015; Jumper et al., 2021; Källberg et al., 2012; McGuffin et al., 2000; Minkyung et al., 2021; Wu and Zhang, 2007). Nearly all predictions suggest the ICD contains a short alpha helix at the N-terminus followed by two beta strands, which together could adopt various three-dimensional structures. The predicted structures vary depending on the program used and the context of ICD sequence (isolated vs. within the full-length HPO-30), suggesting the ICD structure is likely unstable and can adopt diverse conformations (**Figure 1E; Figure 1—figure supplement 1)**. Together, the above mutagenesis and structural analysis suggest that HPO-30 ICD likely uses a folded tertiary structure, instead of a linear peptide motif, to bind to the WRC.

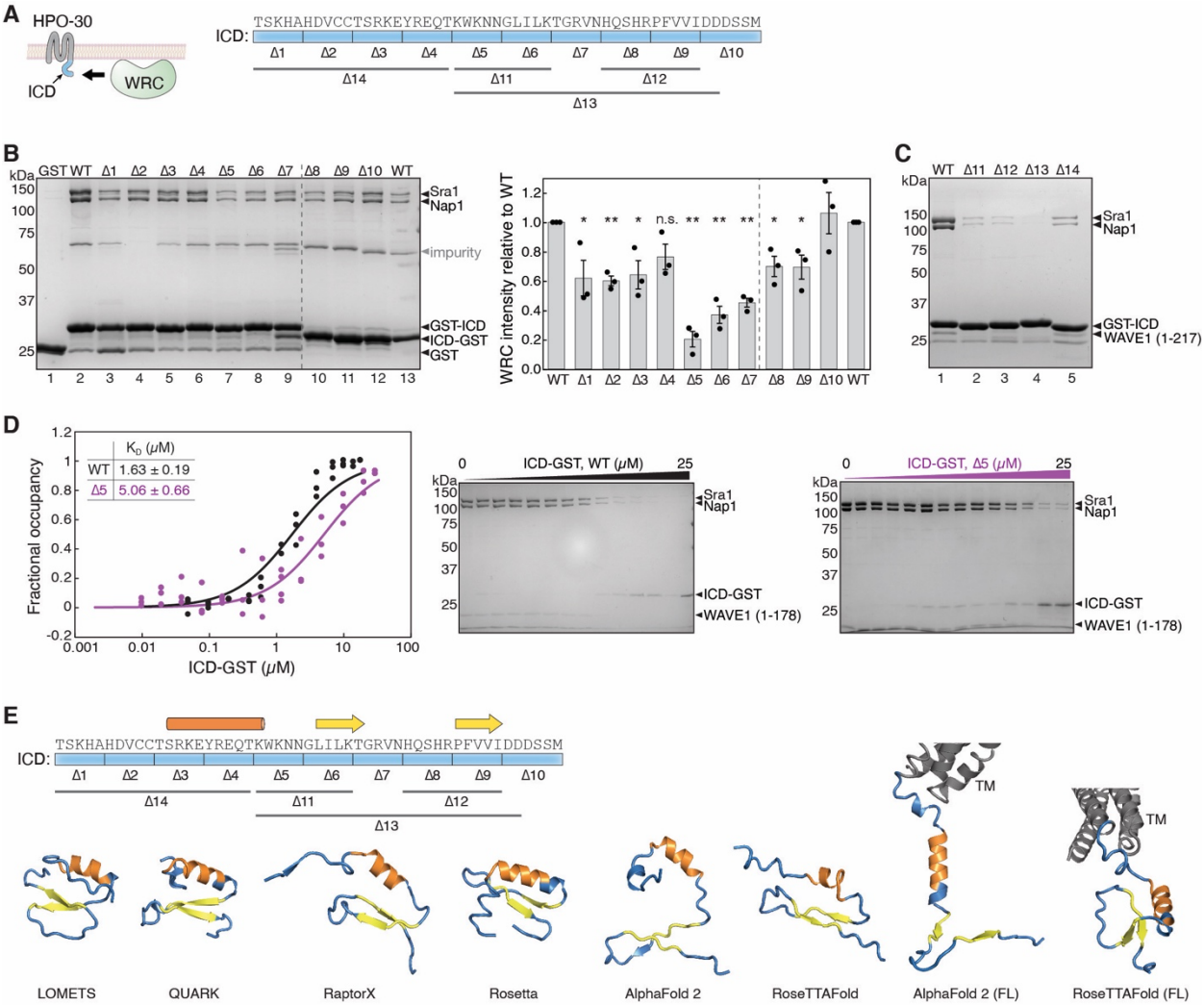

Figure 1. HPO-30 binds to WRC likely using a folded domain, rather than a linear peptide motif. (A) Left: cartoon representation of HPO-30 as a four-pass transmembrane protein, with the ICD binding to the WRC. Right: annotation of HPO-30 ICD sequence and mutants used in this study. Each mutant replaces the corresponding amino acids to alanines (for Δ1-10) or (GGS)n (for Δ11-14). **(B)** Representative Coomassie blue-stained SDS PAGE gel (left) and quantification (right) of three independent experiments showing GST-ICD (lane 2-9, 200 pmol) and ICD-GST (lane 10-13, 200 pmol) pulling down $WRC^{230\Delta WCA}$ (150 pmol). Sra1/Nap1 band intensity was used to quantify the pull-down signals of WRC. Signals from GST-ICD or ICD-GST pull-downs were normalized to corresponding ICD WT (lane 2 and 13, respectively). Error bars represent standard error, * $p < 0.05$, ** $p < 0.005$ from Student's paired t-test. **(C)** Coomassie blue-stained SDS PAGE gel showing GST-ICD Δ11-14 mutants (200 pmol) pulling down $WRC^{217\Delta WCA}$ (300 pmol). **(D)** EPD assay to measure the dissociation constant (K_D) of the interaction between ICD-GST and WT. Left: data pooled from three independent repeats were fitted to a one-site binding model using DynaFit. Right: representative Coomassie blue-stained SDS PAGE gels used for quantification. **(E)** Consensus secondary structure (top) and tertiary structures of HPO-30 ICD predicted by indicated programs (bottom, same color scheme as the secondary structure annotation). "FL" indicates structural predictions of ICD in the context of full length (FL) HPO-30.

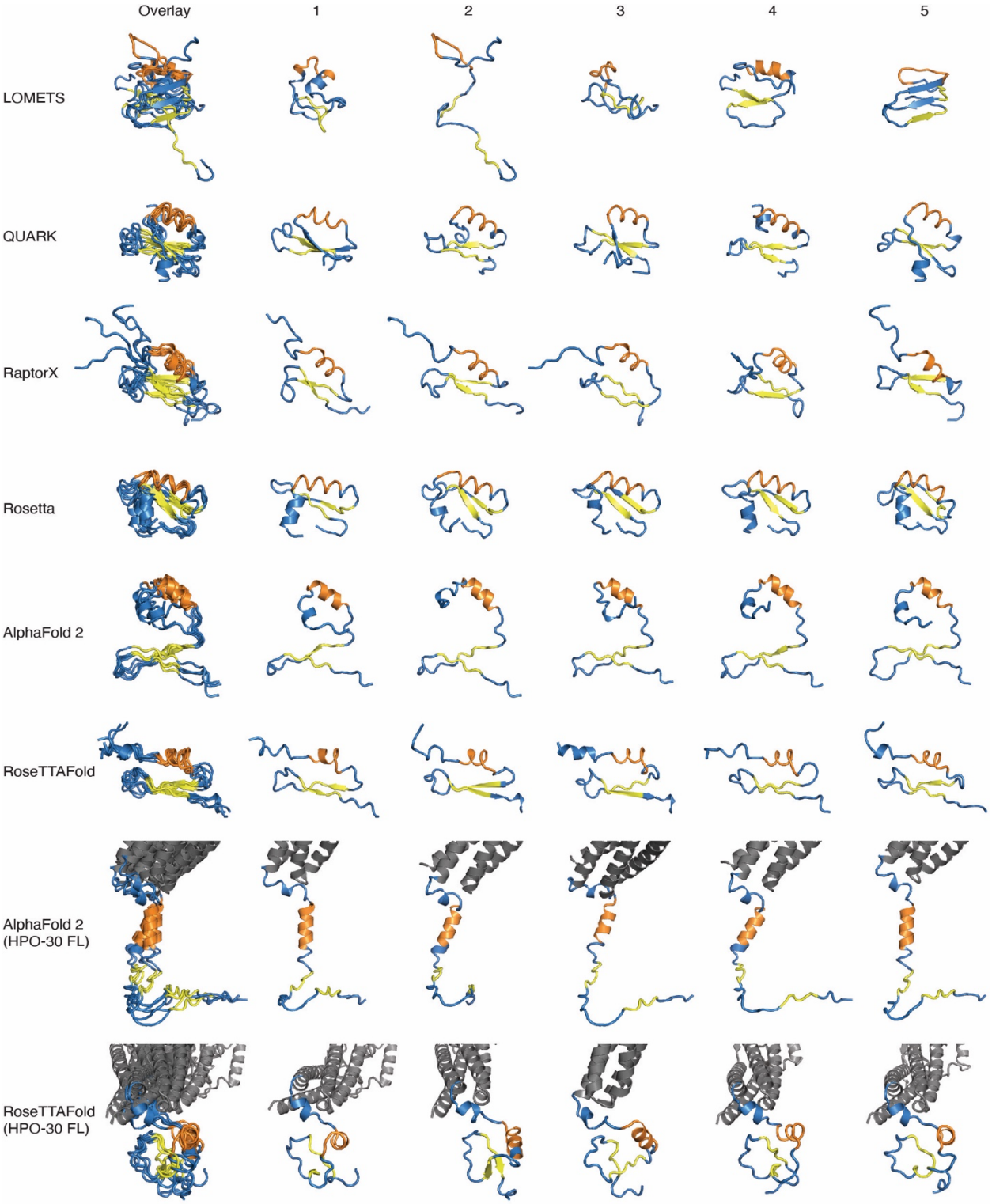

Figure 1—figure supplement 1. Top five predicted structures of HPO-30 ICD by the indicated programs.

HPO-30 ICD is disordered in solution

We tried several approaches to determine the structure of the HPO-30 ICD in isolation. The ICD did not grow crystals either by itself or when attached to solubility tags, or as a co-crystal with the WRC. However, due to its small size and our improved protocol to purify the isotope-labeled ICD in high concentration, we were able to use solution nuclear magnetic resonance (NMR) spectroscopy to obtain well-resolved ^{1}H-^{15}N HSQC spectra of untagged ^{15}N-labeled ICD (**Figure 2A**). From the spectra of the untagged ICD, we could readily identify 50 distinct amide crosspeaks out of the 51 we predicted to observe. The narrow ^{1}H chemical shift dispersion suggests that the HPO-30 ICD is predominantly disordered in solution, with little indications of secondary structure formation. To further increase the stability and yield of untagged ICD, we switched to using GB1-ICD (GB1 is a monomeric, small soluble tag commonly used in NMR) (Zhou and Wagner, 2010). Comparison of the 2D ^{1}H-^{15}N TROSY-HSQC spectra collected for GB1-ICD with the isolated ICD **(Figure 2B**, blue**)** and with the isolated GB1 **(Figure 2C**, red**)** showed no significant chemical shift changes. This suggests that HPO-30 ICD remains largely disordered even when it is linked to a well-folded protein like GB1. Furthermore, the NMR spectra were nearly identical at different protein concentrations (50 – 700 μM) and different temperatures (283 K – 298 K), suggesting the ICD alone does not undergo structural changes in a concentration-dependent manner (data not shown).

This result was consistent with the circular dichroism (CD) spectrum of the ICD, in which no major peaks at either the beta-sheet wavelength (positive at 195 nm and negative at 217 nm) or the alpha-helix wavelengths (positive at 193 nm and negative at 218 and 222 nm) were observed, in contrast to the spectrum of bovine serum albumin (BSA) obtained in the same conditions, which shows clear peaks associated with both structural elements (**Figure 2E**). Addition of an osmolyte, trimethylamine N-oxide (TMAO), which is commonly used to promote protein folding, did not cause a significant change to the CD spectrum or enhance the ICD-WRC interaction (**Figure 2—figure supplement 1**) (Baskakov et al., 1999). Together, these data suggest the purified ICD is unstructured in solution.

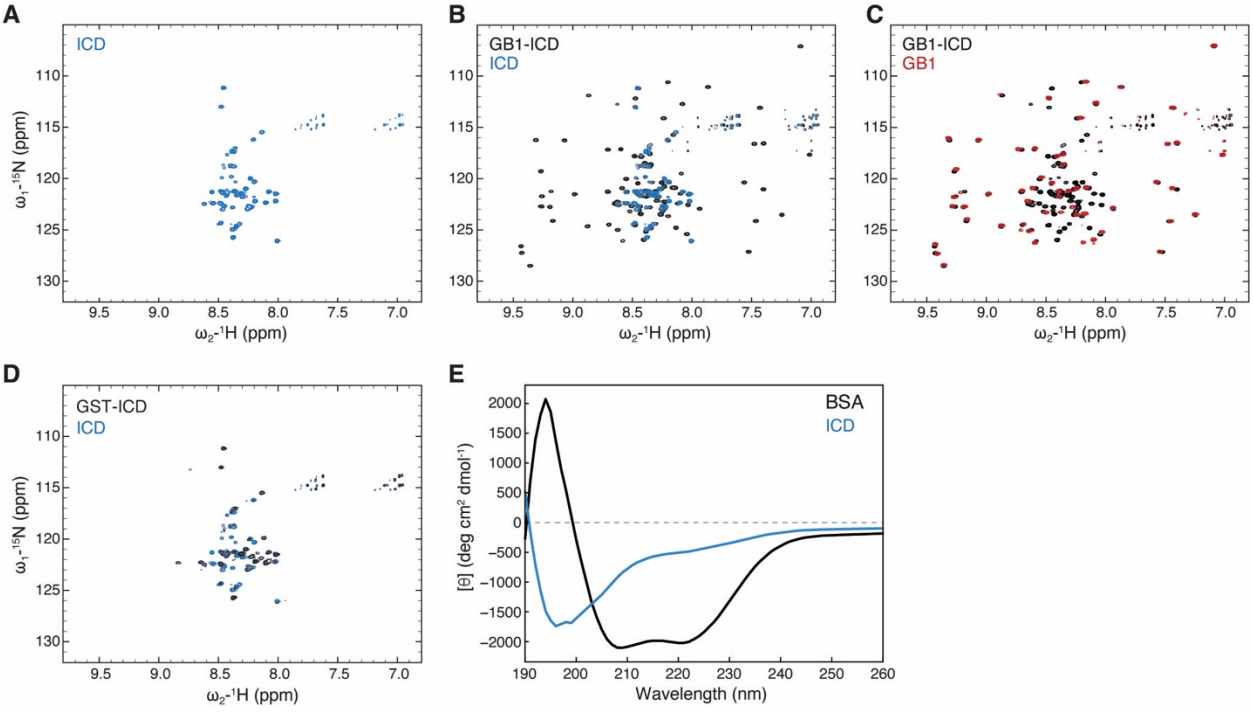

Figure 2. HPO-30 ICD alone is unstructured. (A-D) 2D TROSY spectra of untagged HPO-30 ICD (A), GB1-ICD (B), GB1 (C) and GST-ICD (D) in the same buffer condition (100 mM NaCl, 10 mM HEPES pH 7.0, and 5% glycerol). **(E)** CD spectrum of 2 mg/mL untagged HPO-30 ICD or BSA in 50KMEH5Gd (see Methods and Materials).

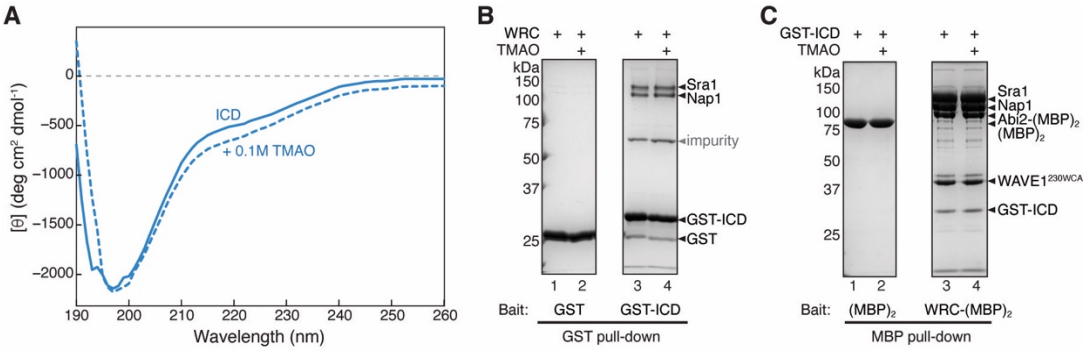

Figure 2—figure supplement 1. (A) CD spectrum of 2 mg/mL HPO-30 ICD in the absence or presence of 0.1 M TMAO. **(B-C)** Coomassie blue-stained SDS PAGE gels showing GST-ICD (200 pmol) pulling down WRC$^{230\Delta WCA}$ (150 pmol) (B) or WRC-$(MBP)_2$ (60 pmol) pulling down GST-ICD (600 pmol) (C) with and without TMAO.

Dimerization is required for HPO-30 ICD to bind WRC

How can the unstructured HPO-30 ICD use a folded structure to bind the WRC? While attempting to solve this conundrum, we realized that the GST-tagged constructs used in our pull-

down assays would dimerize the ICD, as GST is a constitutive dimer (Askelöf et al., 1975). We then hypothesized that the HPO-30 ICD may need to be dimerized for efficient binding to the WRC. To test this hypothesis, we repeated the pull-down assay after switching the GST tag to the monomeric tag MBP (maltose binding protein) (**Figure 3A**). Consistent with our hypothesis, the MBP-tagged ICD indeed showed much weaker binding to the WRC (**Figure 3B**, right). Further supporting the observation that monomeric ICD does not bind to the WRC effectively, GST-ICD binding could not be competed off by a chemically synthesized peptide covering the whole HPO-30 ICD, even when the peptide was added in 5000-fold excess (**Figure 3—figure supplement 1A**).

We next tested several different strategies to further validate if dimerization of the ICD is required for WRC binding. First, we immobilized the WRC to the affinity beads by tethering a dual MBP tag, $(MBP)_2$, to the WRC to pull down different monomeric vs. dimeric forms of HPO-30 ICD. To our surprise, the WRC containing an $(MBP)_2$ tag at the N-terminus of HSPC300, which was previously used to immobilize the WRC and pull down WIRS-containing proteins (Chen et al., 2014a), substantially reduced HPO-30 ICD binding (**Figure 3—figure supplement 1C**, lane 6 vs. 8). Similarly, an $(MBP)_2$ tag at the N-terminus of Abi2 also prevented HPO-30 ICD binding (**Figure 3—figure supplement 1B**). These data suggest tagging $(MBP)_2$ at the N-terminus of HSPC300 or Abi2 may interfere with the HPO-30 ICD binding surface (but not the WIRS binding surface). We eventually used sortase-mediated protein ligation (Chen et al., 2011) to tether an $(MBP)_2$ tag to the C-terminus of Abi2, which produced a WRC that efficiently bound to amylose beads and effectively retained HPO-30 ICD binding **(Figure 3—figure supplement 1C)**. Using this construct, we observed robust binding of all dimeric constructs we tested, including GST-ICD, ICD-GST, and DLC8-ICD (DLC8 is a constitutive dimer from the dynein light chain) (Wang et al., 2003). By contrast, all monomeric constructs, including GB1-ICD, sumo-ICD, and mEGFP-ICD showed very weak, if any, binding (**Figure 3A,C**).

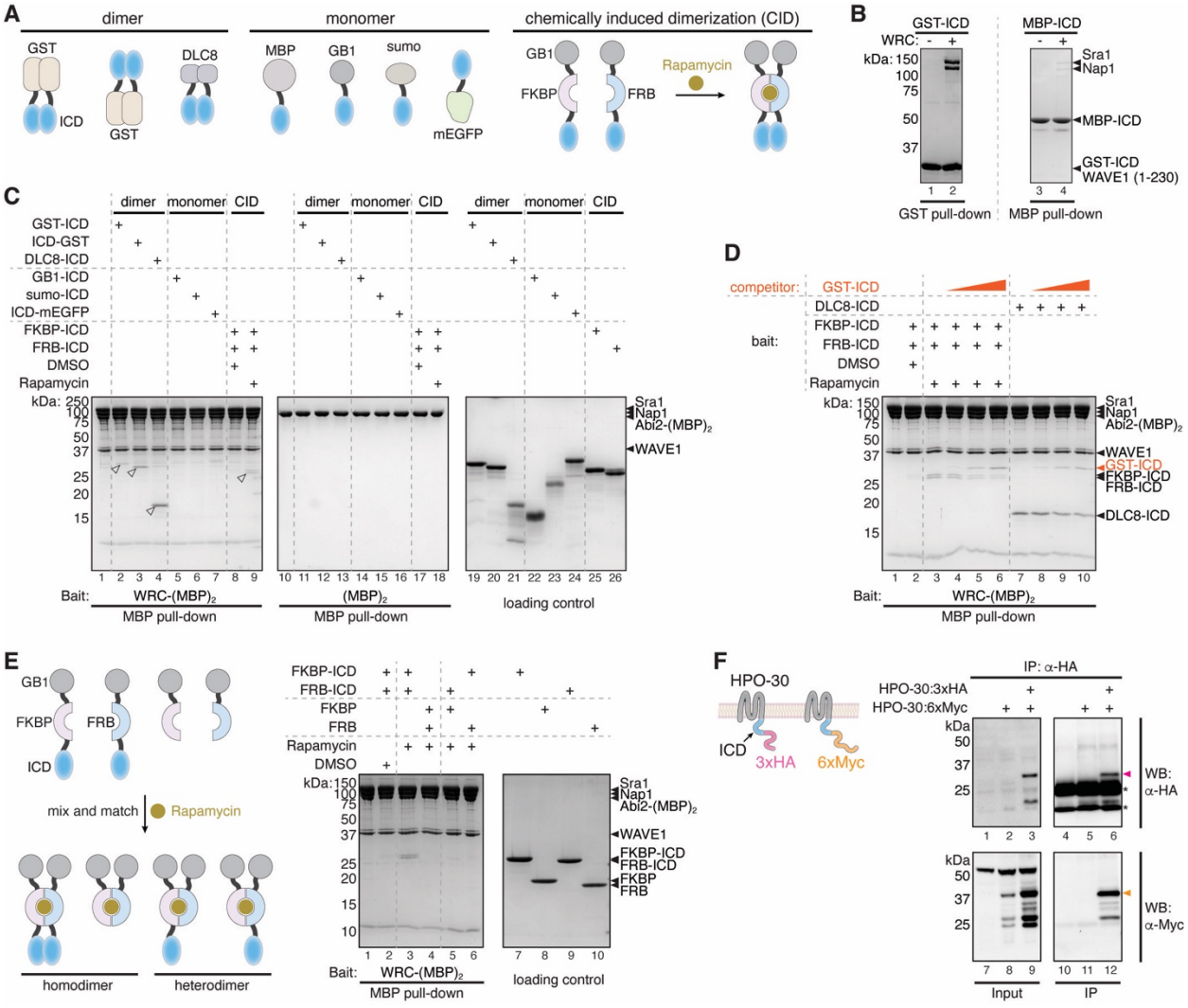

Figure 3. HPO-30 ICD binding to the WRC is enhanced by dimerization. (A) Schematic of HPO-30 ICD constructs used in this study. **(B)** Coomassie blue-stained SDS PAGE gels showing GST-ICD or MBP-ICD (200 pmol) pulling down WRC$^{230\Delta WCA}$ (200 pmol). **(C)** Coomassie blue-stained SDS PAGE gels showing WRC-$(MBP)_2$ or $(MBP)_2$-WRC (60 pmol) pulling down various monomeric and dimeric HPO-30 ICD (600 pmol) indicated in (A). Where it is noted, 5 μM rapamycin (vs. equal volume of DMSO as a negative control) was used to induced dimerization. White arrowheads indicate pull-down signals. For clarity, GB1-FKBP-ICD and GB1-FRB-ICD were referred to as FKBP-ICD and FRB-ICD, respectively. **(D)** Coomassie blue-stained SDS PAGE gels showing WRC-$(MBP)_2$ (60 pmol) pulling down different dimeric HPO-30 ICD (600 pmol) in the presence of GST-ICD as a competitor (600 to 6000 pmol). **(E)** Schematic of the assembly of homo- and heterodimers of HPO-30 ICD (left) and Coomassie blue-stained SDS PAGE gels (right) showing WRC-$(MBP)_2$ (60 pmol) pulling down indicated homo- and heterodimers. In homo- and heterodimers, 1200 pmol of ICD monomeric unit was included to ensure the total amount of ICD remained the same. **(F)** Schematic of full-length HPO-30 constructs co-expressed in *Drosophila* S2 cells (left) and Western blot images (right) showing co-immunoprecipitation of 3xHA-tagged HPO-30 (pink arrowhead) with 6xMyc-tagged HPO-30 (orange arrowhead). Asterisks indicate light and heavy chain of antibody.

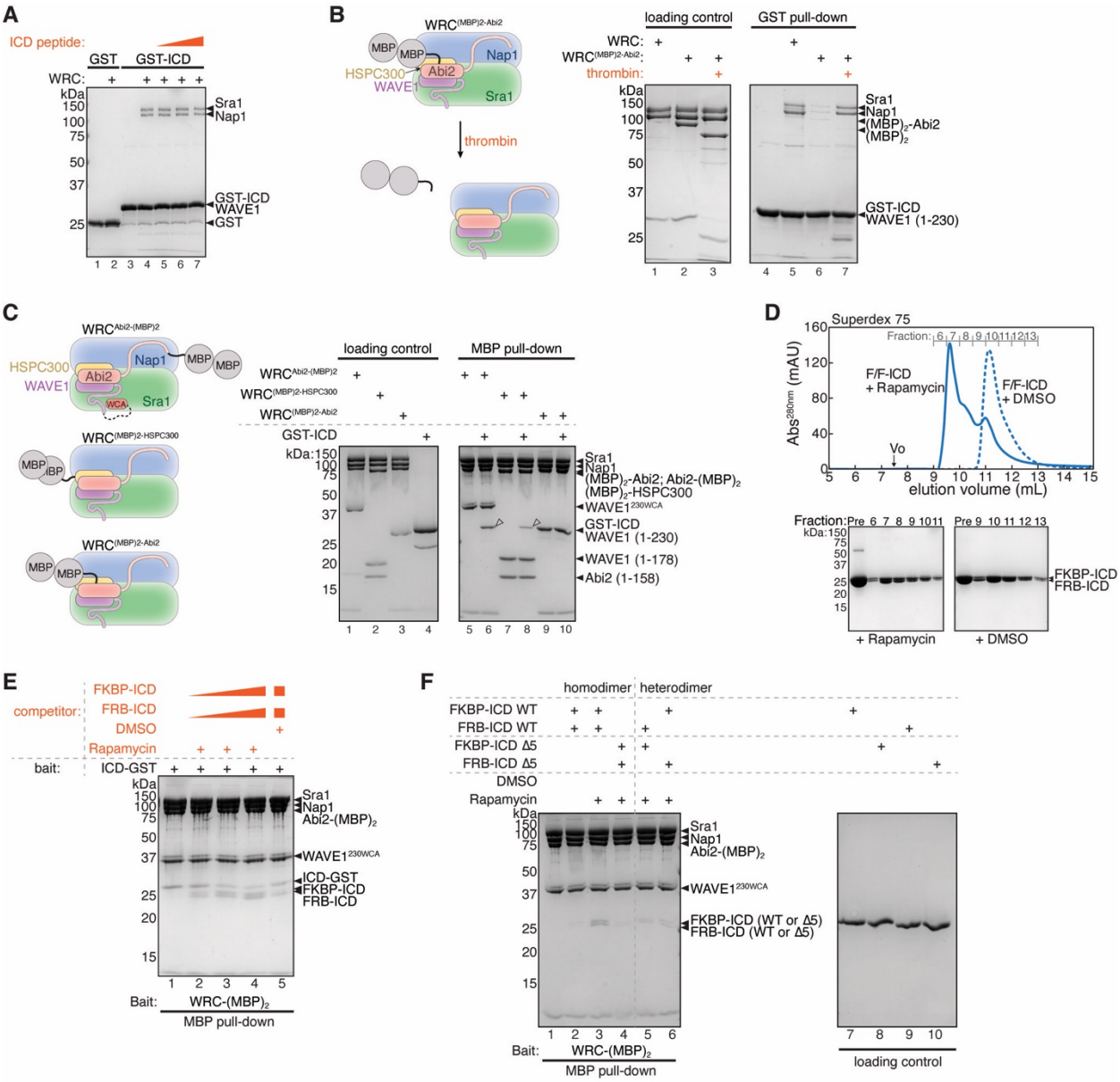

Figure 3—figure supplement 1. Additional data supporting HPO-30 ICD binding to WRC is enhanced by dimerization. (A) Coomassie blue-stained SDS PAGE gel showing GST-ICD (200 pmol) pulling down $WRC^{230\Delta WCA}$ (150 pmol) in the presence of a chemically synthesized HPO-30 ICD peptide as a competitor (18-100 nmol). **(B)** Schematic of removing $(MBP)_2$ tag from $WRC^{(MBP)2\text{-}Abi2}$ by thrombin cleavage (left) and Coomassie blue-stained SDS PAGE gels (right) comparing GST-ICD (200 pmol) pulling down $WRC^{(MBP)2\text{-}Abi2}$ (150 pmol) before or after removal of the $(MBP)_2$ tag. **(C)** Schematic of $(MBP)_2$-tagged WRC constructs (left) and Coomassie blue-stained SDS PAGE gels showing indicated $(MBP)_2$-tagged WRC (60 pmol) pulling down GST-ICD (600 pmol). White arrowheads indicated pull-down signals. **(D)** Top: gel filtration chromatograms of equimolar GB1-FKBP-ICD and GB1-FRB-ICD in the presence or absence of 5 μM rapamycin (or equal volume of DMSO). Bottom: Coomassie blue-stained SDS-PAGE gels of the indicated gel filtration fractions. **(E)** Coomassie blue-stained SDS PAGE gel

showing WRC-$(MBP)_2$ (60 pmol) pulling down ICD-GST (600 pmol) in the presence of FKBP/FRB-ICD as a competitor (600 – 6000 pmol). **(F)** Coomassie blue-stained SDS PAGE gels showing WRC-$(MBP)_2$ (60 pmol) pulling down different combinations of homo- and heterodimers of WT and Δ5 HPO-30 ICD (in which WT ICD monomeric unit was kept at 1200 pmol to ensure the same amount of the WT ICD was included in the reactions).

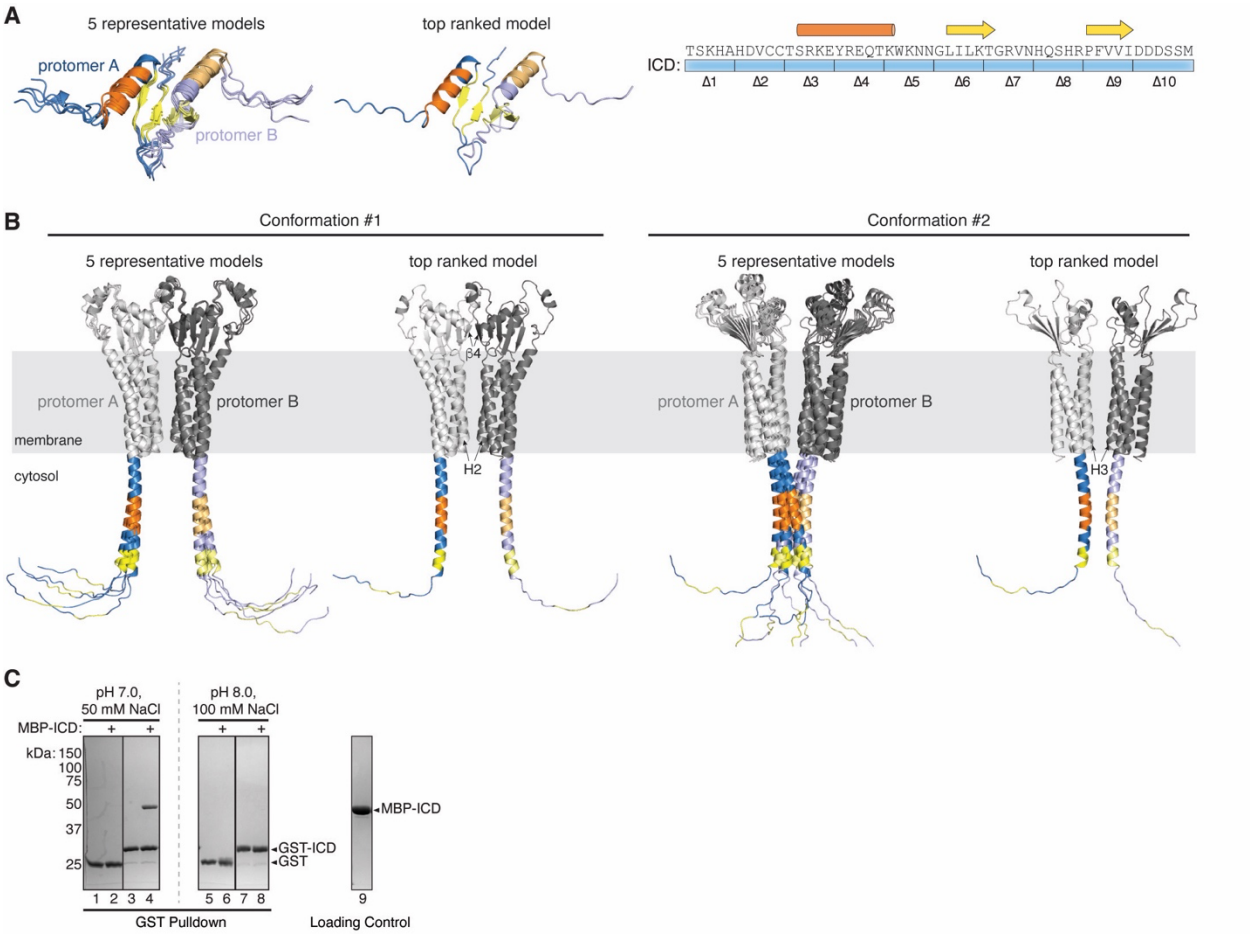

Figure 3—figure supplement 2. HPO-30 can potentially form a dimer. (A) AlphaFold Multimer predictions of the isolated HPO-30 ICD dimer. Promoter A is colored using the same scheme shown on the right (and in Figure 1E), while protomer B is shown in lighter colors. **(B)** Two distinct dimer conformations of the full-length HPO-30 predicted by AlphaFold Multimer. **(C)** Coomassie blue-stained SDS PAGE gels showing GST-ICD (200 pmol) pulling down MBP-ICD (6000 pmol) in indicated buffer conditions.

To further exclude the possibility that the affinity tags nonspecifically affected protein interaction, we introduced the chemically inducible dimerization (CID) tags FKBP and FRB to the ICD, with the GB1 tag at the N-terminus to improve protein expression and solubility (Banaszynski et al., 2005) (**Figure 3A**). In the presence of the dimerizing agent rapamycin, GB1-

FKBP-ICD and GB1-FRB-ICD can readily form a tight heterodimer (**Figure 3A**), as confirmed by size exclusion chromatography in the presence and absence of rapamycin (**Figure 3—figure supplement 1D**). Consistent with results from the above constitutive dimeric tags, the addition of rapamycin to dimerize GB1-FKBP/FRB-ICD (F/F-ICD for short hereafter) clearly promoted HPO-30 ICD binding (**Figure 3C**, lanes 8 vs. 9).

To ensure that the ICDs that contain different dimerization tags bind to the WRC using the same mechanism, we used competition pull-down assays to compare different dimeric constructs. We found GST-ICD effectively competed off both F/F-ICD and DLC8-ICD binding to the WRC in a dose-dependent manner (**Figure 3D**, lanes 4-6 and 8-10). Complementarily, F/F-ICD effectively competed off GST-ICD binding to WRC only in the presence of rapamycin, while in the absence of rapamycin the competition efficiency was significantly reduced (**Figure 3—figure supplement 1E**, lanes 4 and 5). These data further corroborate the notion that dimerized ICD promotes WRC binding, and that all dimeric constructs tested so far bind WRC using the same mechanism.

As an alternative way to validate that dimerization of the HPO-30 ICD is required for WRC binding, we mixed different GB1-FKBP/FRB constructs to produce various heterodimers of the ICD. We found that a heterodimer containing either only one ICD (by mixing with empty GB1-FKBP or FRB tag) or having one WT ICD and an alanine Δ5 mutant ICD failed to support binding to the WRC to the same level as a homodimer containing two WT ICDs (**Figure 3E**; **Figure 3—figure supplement 1F**). Note that in this experiment we kept the total concentration of the WT ICD monomeric unit the same between heterodimers and homodimer. Therefore, the lack of binding from heterodimers was due to lack of the WT ICD dimer, but not reduced WT ICD concentration.

If the ICD needs to be dimerized in order to bind the WRC, we speculated HPO-30 should be able to form dimers in the cell. To test this hypothesis, we expressed 3xHA-tagged and 6xMyc-tagged full-length HPO-30 in *Drosophila* S2 cells and used co-immunoprecipitation to test if HPO-30 interacted with itself (**Figure 3F)**. We found 3xHA-tagged HPO-30 robustly retained 6xMyc-tagged HPO-30, suggesting that full-length HPO-30 is capable of dimerization (or oligomerization) in cells, which could be the functional form of HPO-30. With recent advances in protein structural prediction by AlphaFold, we used AlphaFold Multimer (AFM) to predict whether and how the isolated ICD or the full-length HPO-30 can form a dimer (**Figure**

3—figure supplement 2A,B) (Evans et al., 2022; Jumper et al., 2021). We found the ICD alone was consistently predicted to form a homodimer. Out of 25 prediction solutions, 20 solutions show the same conformation in which dimerization is mediated by a beta sheet formed by the two beta strands from each ICD (**Figure 3—figure supplement 2A**). Consistent with this prediction, purified GST-ICD was able to pull down MBP-tagged ICD in a pH and salt dependent manner, which suggests the dimerization of ICD is mediated through polar interactions (**Figure 3—figure supplement 2C**). The full-length HPO-30 was also predicted to form dimers, but with two distinct conformations. In the first conformation, dimerization was mediated by the interactions between the transmembrane helix 2 (H2) and the beta strand 4 (β4) in the extracellular domain, while in the second conformation, dimerization was mediated by transmembrane helix 3 (H3) and the first helix of the ICD (**Figure 3—figure supplement 2B**). In both conformations, the ICD was predicted to form a long helix, without two beta strands. This contradicts the secondary structural predictions and tertiary structural predictions of the isolated ICD by all other methods, likely because the global prediction of the full-length HPO-30 somehow influenced the prediction of the ICD due to the dominant structures of the N-terminal regions (**Figure 1E**; **Figure 1—figure supplement 1**; **Figure 3—figure supplement 2A**).

Taken together, our data suggest that HPO-30 ICD has the potential to dimerize both *in vitro* and in cells, and the dimerization is required for efficient binding to the WRC.

Dimerization is not sufficient to induce HPO-30 ICD folding

As the dimeric ICD binds to the WRC more strongly than the monomeric form, we used NMR to determine if dimerization could induce structure changes in the HPO-30 ICD. Among various dimerized ICD constructs, only GST-ICD could produce protein at a high enough concentration for NMR measurement. With this material, we managed to obtain well-resolved ^{1}H-^{15}N TROSY-HSQC spectra, which showed ^{1}H chemical shift dispersion nearly identical to the untagged ICD, indicating that dimerization alone was not enough to induce significant ICD folding (**Figure 2D**). Note that we could not see any spectral peaks for the GST tag in this condition due to its large size (~54 kDa as a constitutive dimer) and consequent slow tumbling. Collecting the above evidence, we posit that the HPO-30 ICD needs to undergo both dimerization and induced folding in order to bind to the WRC. This induced folding has been proposed for many DNA-binding proteins and cell-signaling molecules, such as the interaction

between E-cadherin and ß-catenin (Dyson and Wright, 2002; Huber et al., 2001; Huber and Weis, 2001; Turjanski et al., 2008). High-resolution structures of the ICD bound to WRC will be necessary to confirm this hypothesis.

HPO-30 ICD inhibits actin polymerization, but promotes Rac1-WRC activation

Previous studies have shown that Rac1 is the canonical activator of the WRC, and that various WIRS-containing receptors could further fine tune WRC activity, likely through secondary, weak interactions between the WRC and the receptor sequences flanking the WIRS motif (Chen et al., 2014a). After establishing that dimeric ICD robustly binds the WRC, we tested if the interaction could similarly influence WRC activity in promoting Arp2/3-mediated actin polymerization (Cooper et al., 1983; Doolittle et al., 2013a; Kouyama and Mihashi, 1981). While conducting the pyrene-actin polymerization assay, we noticed that buffer conditions had a significant impact on the ICD-WRC interaction. The commonly used pyrene-actin assay buffer for reactions involving WRC, 50KMEI20Gd (50 mM KCl, 2 mM $MgCl_2$, 1 mM EGTA pH 8.0, 10 mM Imidazole pH 7.0, 20% [w/v] glycerol, 1 mM DTT), reduced HPO-30 ICD binding to the WRC. Lowering the concentration of glycerol to 5% and replacing imidazole with HEPES at the same pH rescued binding (**Figure 4—figure supplement 1A**). Using this optimized buffer (50KMEH5Gd, containing 50 mM KCl, 2 mM $MgCl_2$, 1 mM EGTA pH 8.0, 10 mM HEPES pH 7.0, 5% [w/v] glycerol, 1 mM DTT), we tested the effect of monomeric and dimeric HPO-30 ICD on actin polymerization using our chemically inducible dimerization (CID) constructs (shown in **Figure 3A)**, which allowed us to compare the monomeric vs. dimeric ICD directly by switching between DMSO and rapamycin instead of using different solubility tags (**Figure 3—supplement figure 1D**). To our surprise, we observed a strong, dose-dependent inhibition of Rac1-WRC-mediated actin polymerization by HPO-30 ICD (**Figure 4A**, blue vs. orange curves), with the dimerized ICD showing much stronger inhibition (**Figure 4A**, solid vs. dashed curves). By contrast, the dimerized FKBP/FRB tag at the highest concentration only had a mild effect, indicating the inhibition was due to the HPO-30 ICD itself (**Figure 4A**, grey curve). Rapamycin alone had no effect on actin polymerization (**Figure 4—figure supplement 1B**).

Interestingly, we noticed the ICD reduced actin polymerization to a level lower than actin alone. This suggests the inhibitory effect was likely not because of the ICD binding to the WRC and thereby inhibiting WRC activity. Indeed, we found HPO-30 ICD similarly inhibited actin

polymerization induced by the isolated, constitutively active WCA peptide, with the dimerized ICD again showing more potent inhibition (**Figure 4B**). This suggests the inhibitory effect of ICD was not related to WRC, but likely directly related to actin (see below).

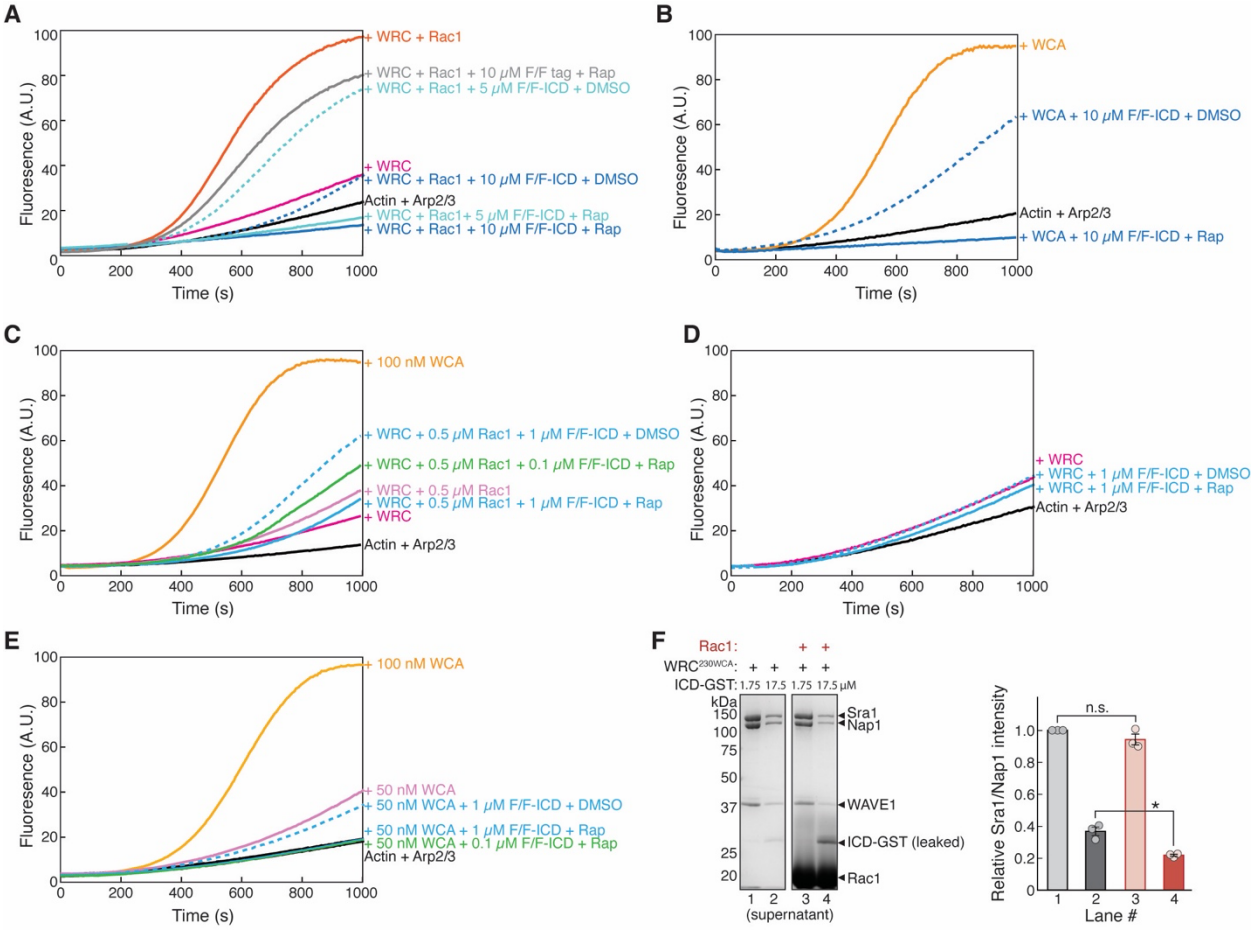

Figure 4. HPO-30 ICD inhibits actin polymerization but promotes Rac1-WRC activation. (A-E) Pyrene-actin polymerization assays of indicated conditions. Reactions contain 2 µM actin (10% pyrene-labeled), 10 nM Arp2/3 complex, 100 nM WRC^{230WCA} or isolated WCA, Rac1^{QP}, indicated concentrations of equimolar GB1-FKBP-ICD and GB1-FRB-ICD, and 5 µM rapamycin or equal volume of DMSO. **(F)** Coomassie blue-stained SDS PAGE gels (left) and quantification from three independent repeats (right) showing equilibrium pull-down of WRC^{230WCA} by two concentrations of ICD-GST in the presence or absence of 40 µM Rac1^{QP}. Error bars represent standard error, * $p < 0.05$, from Student's paired t-test.

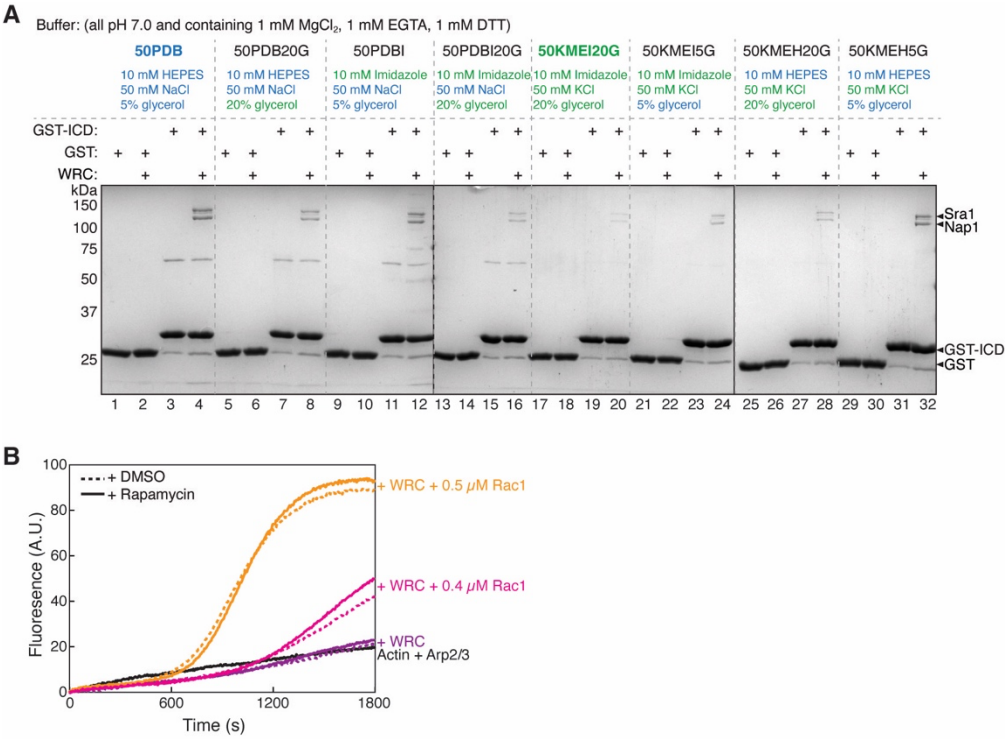

Figure 4—figure supplement 1. Buffer optimization of HPO-30 ICD pyrene-actin polymerization assay. (A) Coomassie blue-stained SDS PAGE gels showing GST-ICD (200 pmol) pulling down $WRC^{230\Delta WCA}$ (150 pmol) in indicated buffer conditions, with 50PDB being the buffer used in the majority of pull-down reactions herein and 50KMEI20G commonly used in pyrene-actin assembly assays in previous studies of the WRC. All buffers contained 1 mM DTT and 0.05% Triton X-100. (B) Pyrene-actin polymerization assays showing rapamycin and DMSO did not affect WRC activity. Reactions contain 4 μM actin (5% pyrene-labeled), 10 nM Arp2/3 complex, 100 nM WRC^{230WCA}, $Rac1^{QP}$, and 5 μM rapamycin or equal volume of DMSO.

The strong, WRC-independent inhibitory effect of the ICD on actin polymerization prevented us from directly examining how ICD binding influenced WRC activity. To overcome this challenge, we reduced the ICD concentration to 1 μM in the actin assays to minimize its inhibitory effect. Interestingly, we found that 1 μM monomeric ICD slightly, but robustly, increased the WRC-mediated polymerization when WRC was activated to a low level by an intermediate concentration of Rac1 (**Figure 4C**, dashed blue vs. solid pink curves). At the same concentration, the dimerized ICD still showed a dominant inhibitory effect (**Figure 4C**, solid blue curve). We hypothesized that in the absence of rapamycin, a small amount of HPO-30 ICD existed in equilibrium as a dimer, which could bind the WRC to promote activation. This is supported by both structural predictions and *in vitro* pulldown results (**Figure 3—figure supplement 2A,C**). To test this hypothesis, we further reduced HPO-30 ICD to a much lower

concentration (0.1 μM) and included rapamycin to ensure dimer formation. At this low concentration, the dimerized ICD similarly promoted Rac1-WRC-medicated actin polymerization (**Figure 4C**, solid green curve). Although we were limited by the strong inhibitory activity of the ICD on actin polymerization and therefore could only measure a mild activating effect by using low ICD concentrations, this effect was specific to Rac1-activated WRC, as neither the WRC in the absence of Rac1 nor the isolated WCA could be further activated by ICD (**Figure 4 D,E**). This effect is similar to the WIRS-containing ICD from the cell adhesion membrane protein protocadherin 10 (PCDH10), in which PCDH10 ICD by itself had no effect on WRC activity, but cooperatively increased WRC activity when WRC was slightly activated by intermediate concentrations of Rac1 (Chen et al., 2014a). This cooperativity effect suggests the HPO-30 ICD should prefer to bind the WRC activated by Rac1. Consistent with this hypothesis, our equilibrium pull-down (EPD) assay showed GST-ICD could indeed pull down more WRC in the presence of saturating concentrations of Rac1 (**Figure 4F**, lane 2 vs. 4—note that in EPD assays, the supernatant of the pull-down reactions was used to quantify the WRC that was not retained by immobilized GST-bait). Interestingly, within the HPO-30-DMA-1 co-receptor complex, DMA-1 directly binds to TIAM-1, a Rac GEF, which could act synergistically with the direct effect of HPO-30 to promote WRC activation by increasing Rac1 activity (Zou et al., 2018).

HPO-30 ICD binds to F-actin and inhibits actin depolymerization, similar to CapZ

We first wondered if the WRC-independent inhibitory effect of HPO-30 ICD was due to the ICD binding to and sequestering free G-actin. However, we observed no detectable binding between GST-ICD or dimerized F/F-ICD and G-actin (**Figure 5—figure supplement 1**). We next wondered if the ICD inhibited actin polymerization by binding to F-actin. In our F-actin co-pelleting assay (Heier et al., 2017), we found that significantly more F/F-ICD indeed bound to F-actin, compared to BSA, F/F tag, and the capping protein CapZ (which binds to the barbed ends of F-actin) (**Figure 5A,B**). Interestingly, both the monomeric and dimeric F/F-ICD showed significant and similar binding to F-actin (**Figure 5A,B**, +DMSO vs. +Rap), although the dimeric ICD showed slightly stronger binding. This suggests that the monomeric ICD, while not as effective in inhibiting actin polymerization as the dimeric form, is also capable of binding to

actin filaments. Together, these data led us to a hypothesis that HPO-30 ICD may bind to actin filaments to prevent actin polymerization.

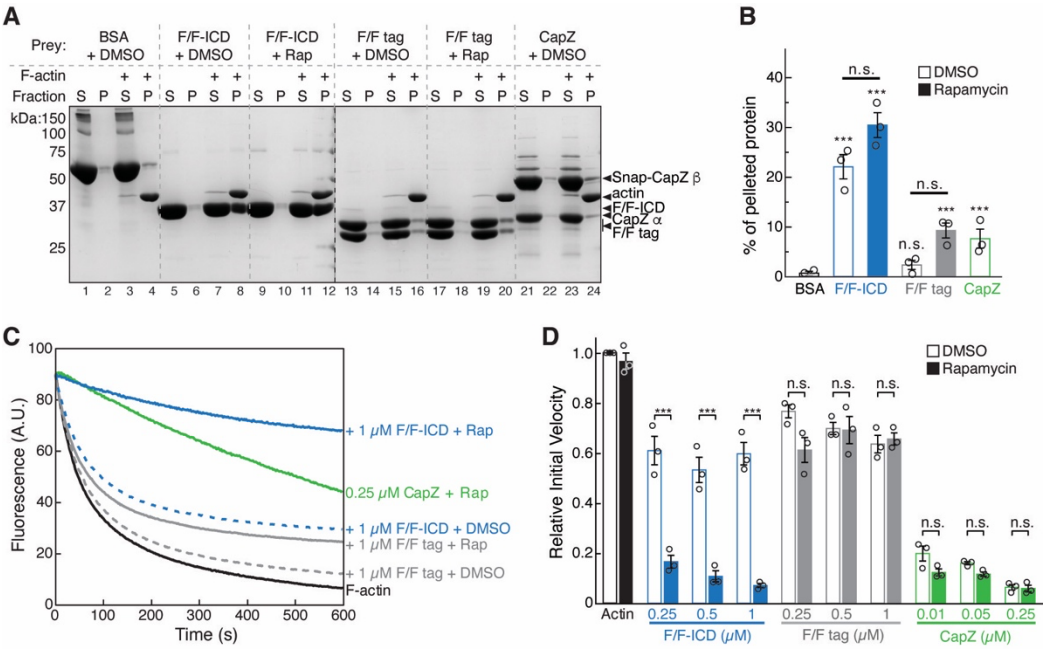

Figure 5. HPO-30 ICD binds to F-actin and inhibits actin depolymerization. (A) Representative Coomassie blue-stained SDS PAGE gels showing F-actin co-pelleting assays of indicated F/F-ICD and CapZ in the presence or absence of 5 μM rapamycin (or equal volume of DMSO). S: supernatant, P: pellet. **(B)** Quantification of (A) from three independent repeats, showing percentage of proteins in the pellet. Bars represent standard error, *** $p < 0.001$, ANOVA with Tukey test. **(C)** Representative F-actin depolymerization assay fluorescence curves of indicated conditions. Each reaction contained 5 μM pre-polymerized actin (70% pyrene labeled), diluted 20-fold into depolymerization buffer containing indicated proteins in the presence or absence of 5 μM rapamycin (or equal volume of DMSO). **(D)** Quantification of the initial velocity of fluorescence curves shown in (C). Initial velocity was normalized to F-actin alone in the presence of DMSO. Error bars represent standard error, n = 3 independent repeats, *** $p < 0.001$, ANOVA with Tukey test.

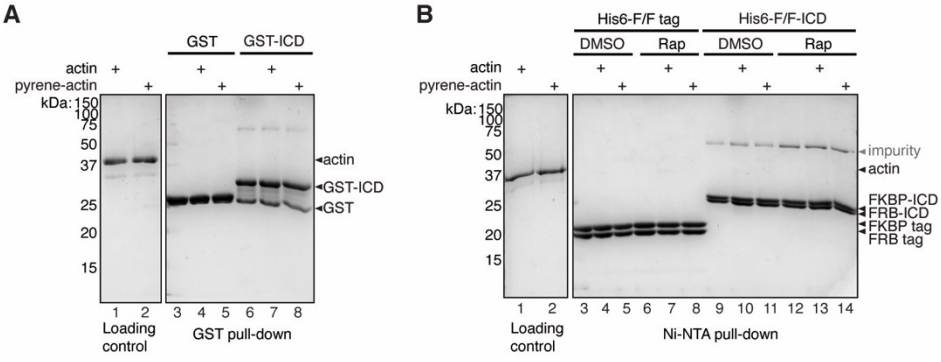

Figure 5—figure supplement 1. HPO-30 ICD does not bind to G-actin. (A-B) Coomassie blue-stained SDS PAGE gels showing GST-ICD (200 pmol) (A) or His6-F/F-ICD (B) (300 pmol) pulling down actin or pyrene labeled actin (500 pmol) in G buffer (2 mM Tris-HCl pH 8, 0.5 mM DTT, 0.2 mM ATP, 0.1 mM $CaCl_2$, 1 mM NaN_3), in the presence of 5 μM rapamycin (or equal volume of DMSO).

One group of proteins well-known to inhibit actin polymerization are called capping proteins (e.g., CapZ), which bind to the barbed ends of actin filaments to inhibit both actin polymerization and depolymerization from the barbed end (Caldwell et al., 1989; Weeds and Maciver, 1993). To test if the HPO-30 ICD may act as a capping protein, we used a depolymerization assay that has been commonly used to measure CapZ activity (Caldwell et al., 1989; Cooper and Pollard, 1985). We found that, similar to CapZ, HPO-30 ICD inhibited actin depolymerization (**Figure 5C,D**). Note that this activity was both concentration- and dimerization-dependent, similar to the ICD binding to WRC, suggesting dimerization is also involved in this capping-like activity. The ability to cap filaments also explains why dimeric HPO-30 ICD is capable of inhibiting actin polymerization more strongly than monomeric ICD.

HPO-30 ICD binds both the side and barbed end of actin filaments

In the above bulk solution assays, the dimerization-independent binding to F-actin (**Figure 5A,B**) versus the dimerization-dependent inhibition of actin polymerization and depolymerization (**Figure 4A,B, 5C,D**) suggest HPO-30 ICD may have two distinct activities on actin filaments, with only the dimerization-dependent activity resembling that of CapZ. This is also supported by the observation that F-actin pelleted a more significant amount of HPO-30 ICD than CapZ, as CapZ only binds to the barbed end of F-actin (albeit with high affinity) (**Figure 5A,B**) (Caldwell et al., 1989). Therefore, the ICD may bind to not only the barbed end (in a dimerization-dependent manner), but also other locations of the actin filament (in a dimerization-independent manner).

To directly validate these F-actin binding activities, we used single-molecule total internal reflection fluorescence (smTIRF) microscopy to visualize how HPO-30 ICD binds to actin filaments. For this assay, we prepared fluorophore-labeled proteins by fusing a SNAP tag to the N-terminus of the CapZ β-subunit, FKBP-ICD, FRB-ICD, FKBP tag, and FRB tag, which allowed us to label proteins using different SNAP-Surface® AlexaFluor® dyes (hereafter referred to as AF followed by the corresponding excitation wavelength) through the SNAP tag

and minimize the effect of fluorophore-labeling on protein activity. Actin was labeled with AF647 using previously established methods (Hansen et al., 2013). The SNAP-tagged F/F-ICDs were capable of binding the WRC in a rapamycin-dependent manner and to a level similar to the GB1-tagged F/F-ICD, suggesting that the SNAP-tag did not affect ICD binding to WRC (**Figure 6—figure supplement 1A**, lane 1-4). The labeled CapZ and F/F-ICD proteins exhibited capping activity similar to their counterparts used in bulk solution assays (except AF647-labeled F/F-ICD, which we decided to exclude from smTIRF assays) (**Figure 6—figure supplement 1B,C**).

The smTIRF experiments clearly showed $SNAP^{AF488}$-CapZ (at 5 nM) bound to the barbed end of filaments and stopped their growth (**Figure 6A** top; **6C** green; **Video 1,2**), consistent with the high affinity and very slow off-rate of CapZ at the barbed end shown in previous studies (Caldwell et al., 1989). Distinct from CapZ, $SNAP^{AF546}$-F/F-ICD (15 nM, with 8-fold molar excess of rapamycin) clearly revealed HPO-30 ICD mainly bound to the side of actin filaments, instead of the barbed end (**Figure 6A** bottom; **6B**; **Video 3-4**) (see below). **Figure 6A** bottom shows an example of binding of HPO-30 ICD near the barbed end of the filament (time 36.5 s), after which the filament continued to grow while the ICD molecule stayed bound to the same position. Note that this HPO-30 ICD molecule was bound to the filament, not the PEG-coated surface, because it moved together with the filament (Video 3,4). We applied stringent criteria to prevent misidentification of nonspecific background signals as binding events (see Materials and Methods) and found that 33% of filaments had at least one binding event over the course of the 15-minute duration of the experiment, which was significantly higher than the number of events for the F/F tag in identical conditions (**Figure 6B**).

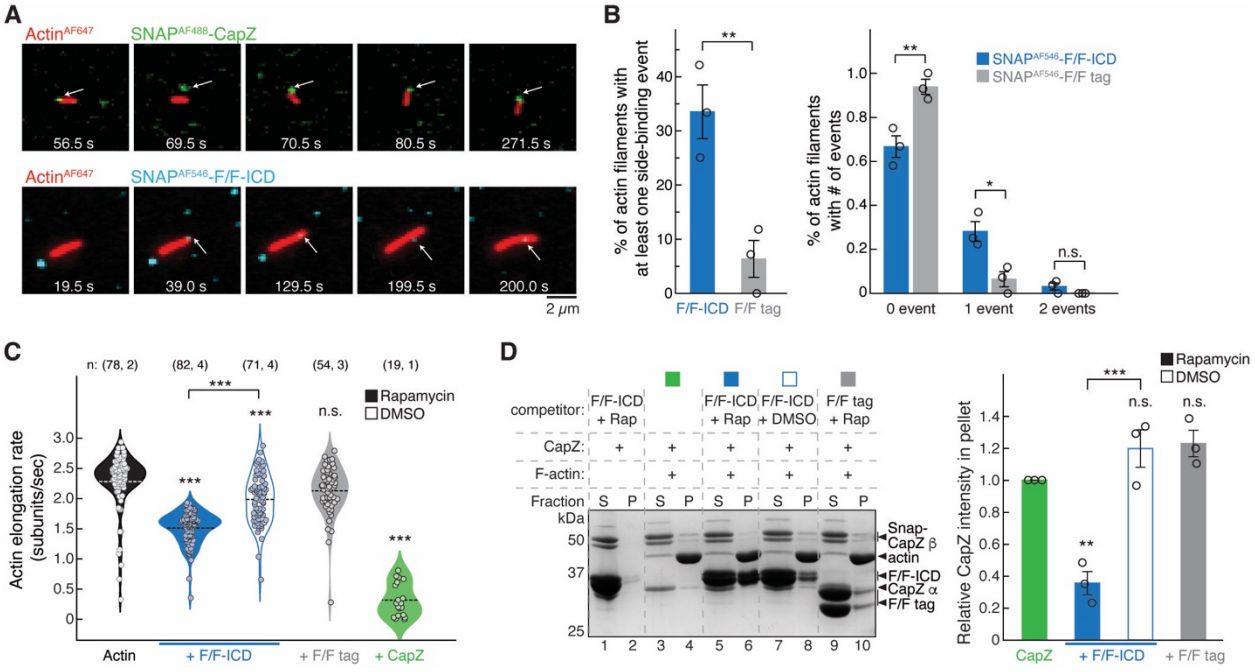

Figure 6. HPO-30 ICD binds both the side and barbed end of actin filaments. (A) Examples of time lapse images from smTIRF experiments. Top: a capping event of SNAP^{AF488}-CapZ (green, 5 nM) and actin^{AF647} (red). Bottom: a side-binding event of SNAP^{AF546}-F/F-ICD (cyan, 15 nM) and actin^{AF647} (red). Note that in smTIRF time-lapses, sometimes a lag was observed between signals at the two channels. For example, in the top row, the filament and SNAP^{AF488}-CapZ puncta were displaced at 69.5 s, but aligned again at 70.5 s. The lagging was due to image acquisition conditions, where, to prevent photobleaching of AF647, images in the 640 nm-channel for actin^{AF647} were taken every 20 acquisitions of the 488 nm-channel for SNAP^{AF488}-CapZ (see Materials and Methods) **(B)** Quantification of the frequency of side binding events from smTIRF imaging. Left: comparison of overall side binding events. Right: comparison of the percentage of filaments with 0, 1, and 2 events. Data were from three independent repeats, at least 15 filaments randomly selected per video. Bars represent standard error. * $p < 0.05$, ** $p < 0.01$, Student's paired t-test. **(C)** Violin plot showing quantification of elongation rate of actin filaments measured by smTIRF imaging. Total number of filaments pooled from the number of independent repeats for each sample are indicated in the paratheses on top of each column, respectively. *** $p < 0.001$, ANOVA with Tukey test. **(D)** Representative Coomassie blue-stained SDS PAGE gel (left) and quantification of pelleted CapZ from three independent repeats (right) showing F-actin (2 μM) co-pelleting assay of CapZ (0.6 μM) with the indicated F/F-ICD or F/F tag as a competitor (5 μM) in the presence or absence of 5 μM rapamycin (or equivalent volume DMSO). S: supernatant, P: pellet. Bars represent standard error, ** $p < 0.01$, *** $p < 0.001$, ANOVA with Tukey test.

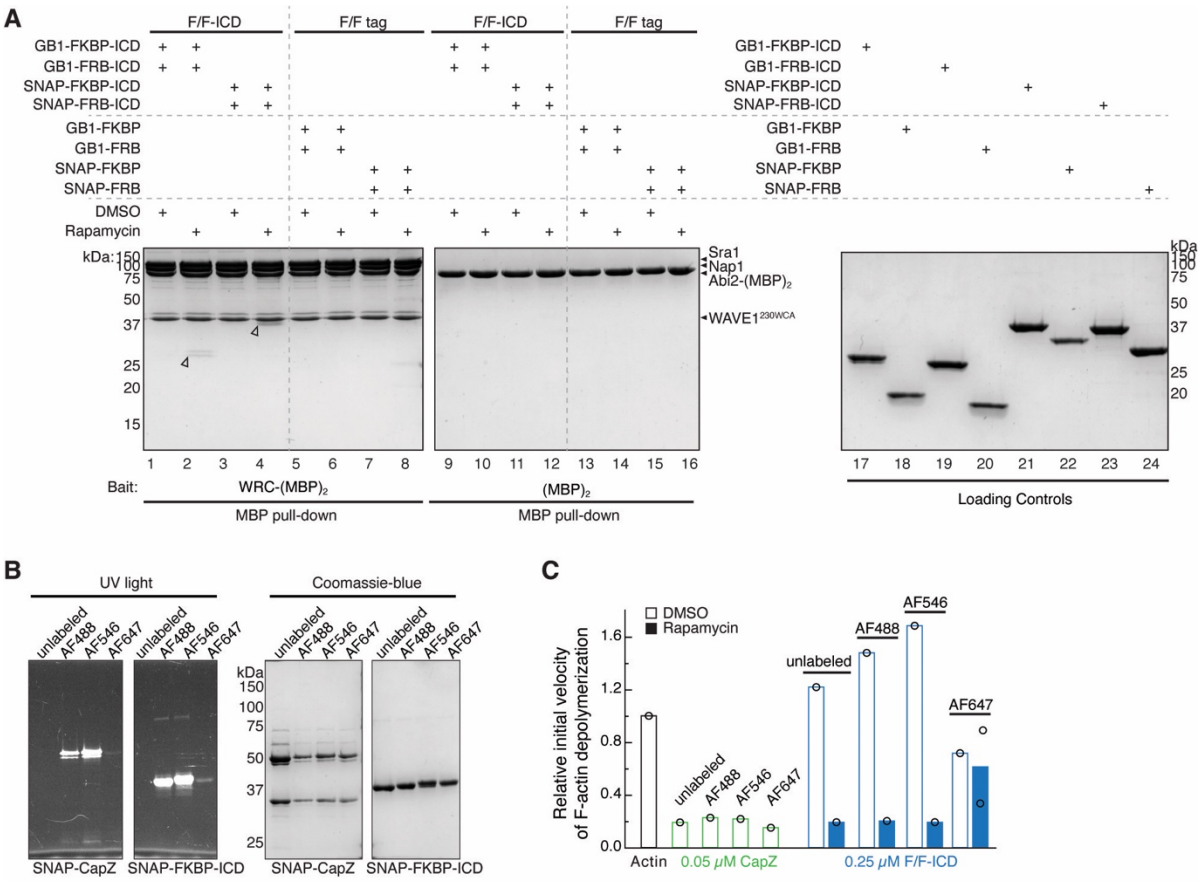

Figure 6—figure supplement 1. SNAP tag and fluorophore-labeling did not affect HPO-30 ICD function. **(A)** Coomassie blue-stained SDS PAGE gel showing WRC-$(MBP)_2$ (60 pmol) pulling down GB1-tagged vs. SNAP-tagged HPO-30 ICD (600 pmol) in the presence or absence of 5 μM rapamycin. **(B)** SDS PAGE gels of SNAP-tag labeling of CapZ, FKBP-ICD, and FKBP tag with indicated SNAP-Surface© AlexaFluor© dyes. Left: UV light with Alexa-488 filter. Right: Coomassie blue stain. **(C)** Actin depolymerization assays of SNAP-Alexa labeled proteins in conditions identical to Figure 5C,D.

Since we could not further increase the concentration of fluorophore-labeled ICD in smTIRF experiments to promote the chance of observing barbed end binding events without causing high background, we switched to using unlabeled ICD at a higher concentration to examine if the ICD inhibited actin filament growth as we observed in bulk solution assays in **Figure 5C,D (Figure 6C**; **Video 5)**. We found that at 1 μM concentration, dimerized F/F-ICD significantly reduced actin elongation rate from 2.3 ± 0.5 subunits/sec for actin alone to 1.5 ± 0.3 subunits/sec (Kuhn and Pollard, 2005) (**Figure 6C**, black vs. solid blue). The same concentration of monomeric F/F-ICD also significantly slowed down actin elongation, but to a lesser extent (2.0 ± 0.4 subunits/sec) (**Figure 6C**, open blue). This effect may result from the side-binding

activity of ICD slowing down actin polymerization or, more likely, a small population of dimeric ICD in equilibrium with the monomeric ICD, which could bind to the barbed end (see below). Importantly, dimerized F/F tag barely affected actin polymerization (2.1 ± 0.4 subunits/sec) (**Figure 6C**, grey). We were limited by sample addition to the microfluid chamber from high-concentration protein stocks and, as such, we could not further increase the unlabeled ICD concentration to higher than 1 μM in order to observe an even stronger inhibitory effect. By comparison, 5 nM CapZ strongly inhibited actin polymerization (0.3 ± 0.1 subunits/sec). Together, these data suggest that HPO-30 ICD and CapZ similarly inhibit actin filament elongation, although the activity of HPO-30 ICD is less potent.

In the above smTIRF experiments, we were unable to capture stable binding of the ICD to the barbed end as we were for CapZ, likely because of multiple technical challenges: 1) the low concentration of ICD that we had to use in single molecule assays (nM vs. μM that we used in bulk solution assays), 2) possibly low affinity and fast off-rate of the ICD at the barbed end (reflected by the higher concentration than CapZ that was required for inhibiting actin depolymerization in bulk solution assays), 3) the complications of the side-binding activity (which, due to light diffraction limit, made it difficult to distinguish real barbed end binding events from side binding near the barbed end), 4) the amount of dimeric HPO-30 is likely to be very low, as the affinity of the FKBP-rapamycin complex for FRB (which is responsible for dimerization of HPO-30 in this system) is ~12 nM (Banaszynski et al., 2005), and 5) the speed limitation of data acquisition (50 or 100 ms exposure time, which could miss fast binding/dissociation events). In order to determine if the ICD can indeed bind to the barbed end, we used a competition co-pelleting assay to examine if ICD binding can compete off CapZ binding to the barbed end of F-actin (**Figure 6D**). In this assay, due to the high affinity of CapZ to the barbed end, we used 10 times the concentration of F/F-ICD to compete against CapZ. We found that the dimerized F/F-ICD effectively reduced CapZ binding by over 60%, whereas the monomeric F/F-ICD or the dimerized F/F tag had no effect (**Figure 6D**). This result suggests dimeric, but not monomeric ICD binds to the barbed end, which can block CapZ binding, consistent with the result that dimeric ICD is more effective in inhibiting actin polymerization (**Figure 4A,B**) and depolymerization (**Figure 5C,D**). Alternatively, dimeric HPO-30 ICD could bind near, instead of directly to, the barbed end, which could allosterically destabilize CapZ

binding by altering the conformation of the actin filament. High-resolution structural information will be necessary to distinguish between these two scenarios.

Combining the above results, we conclude that HPO-30 ICD monomers preferentially bind to the side of actin filaments, while the dimers can bind to both the sides and the barbed end (or near the barbed end) of filaments. Only the (near-) barbed end binding by dimers can inhibit actin filament growth in a manner similar to the capping protein CapZ.

Discussion

HPO-30 is a claudin-like membrane protein required for higher order dendrite branching in *C. elegans* PVD neurons. Previous studies showed this function required the HPO-30 ICD to bind to the WRC, which in turn could activate Arp2/3 to generate branched actin networks to deform the membrane and promote new dendrite formation (Zou et al., 2018). Here, our biochemical, biophysical, structural, and single molecule analysis uncovers two distinct, novel mechanisms used by the HPO-30 ICD to regulate local actin dynamics. In the first mechanism, the unstructured ICD undergoes dimerization and induced folding to bind the WRC, which, in addition to recruiting the WRC to local dendrite branching sites, can also cooperate with Rac1 to promote WRC activation (**Figure 7**, step 3). In parallel, the co-receptor of HPO-30, DMA-1, was shown to bind the Rac-GEF, TIAM1, which would provide an additional layer of control to promote Rac1 activation and drive WRC-Arp2/3-mediated actin polymerization (Zou et al., 2018). In the second mechanism, the ICD can directly bind to actin filaments to modulate actin dynamics. Both monomeric and dimeric forms of the ICD can bind to the side of actin filaments, but only the dimeric ICD can bind to the barbed end to inhibit both actin polymerization and depolymerization, similar to the activity of the capping protein CapZ (**Figure 7**, step 1). These two seemingly contradictory actin regulatory mechanisms offered by the same membrane receptor could provide exquisite tuning of local actin dynamics to prepare for dendrite branching (**Figure 7**, and see discussion below).

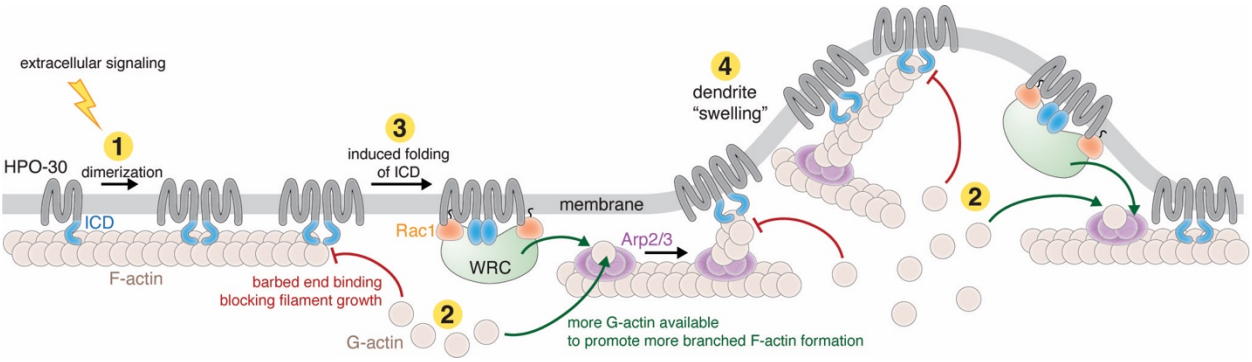

Figure 7. Model showing HPO-30 ICD integrates two distinct mechanisms to regulate actin dynamics and promote dendrite branching. In (1), HPO-30 on the dendrite membrane undergoes dimerization (or oligomerization). Both monomeric and dimeric forms of HPO-30 ICD can bind to the side of actin filaments, but only the dimeric ICD can bind to the fast-growing barbed end. In (2), dimeric ICD binding to the barbed end acts as a capping protein, which stops long filament growth and helps reserve G-actin for the Arp2/3 complex to nucleate actin for producing more short, branched actin filaments. In (3), the dimeric ICD undergoes induced folding to bind the WRC. This interaction recruits the WRC to the membrane and simultaneously promotes WRC activation by Rac1, which in turn stimulates Arp2/3 to produce branched actin filaments. In (4), the dual actions of HPO-30 ICD cooperatively promote the formation of branched actin networks, which can cause the "swelling" of dendrite observed in previous studies (Shi et al., 2021), an important prerequisite for the outgrowth of a new dendrite branch.

Many neuronal receptors, including SYG-1, Robo, Neogenin, TMEM132, neuroligins, and various protocadherins, contain a short WIRS peptide motif in their ICD, which allows them to recruit the WRC to their sites of action at membranes to regulate local actin polymerization in diverse cellular processes (Chaudhari et al., 2021; Chia et al., 2014; Fan et al., 2018; Lee et al., 2016; Wang et al., 2021; Xing et al., 2018). The HPO-30 ICD does not contain a WIRS motif. Instead, our structural-function analysis, structural predictions, and biophysical measurements reveal that HPO-30 ICD is unstructured, requires dimerization, and likely undergoes induced folding in order to bind to the WRC. This binding mechanism should be conserved throughout animals, as the HPO-30 ICD is conserved only in nematodes, but can bind to both *C. elegans* and human WRCs (Zou et al., 2018). Therefore, HPO-30 represents a new class of transmembrane proteins, which interact with the WRC using a noncanonical mechanism distinct from the previously identified WIRS peptide-containing receptors (Chen et al., 2014a). Exactly how HPO-30 ICD dimerizes and folds into a structure to bind the WRC is currently unknown, but the knowledge from our study has laid the ground for high-resolution structural determination of the HPO-30 ICD bound to the WRC, which will not only reveal the interaction mechanism and

identify the interaction surface on the WRC, but also facilitate the identification of human homologs of HPO-30 and revelation of new biological functions of this interaction in neural development (and/or other processes).

Our study suggests that HPO-30 binding to the WRC not only provides a membrane localization mechanism to recruit the WRC to the dendrite branching site, but also can simultaneously promote WRC activation by Rac1. The dual, synergistic actions of both binding and activating the WRC have been observed in several WIRS-containing receptors, such as PCDH10, in which WIRS peptide binding is responsible for membrane recruitment, while weak, secondary interactions from the flanking sequences in receptor ICD promotes WRC activation (Chen et al., 2014a). The HPO-30 ICD, however, is distinct from WIRS-containing receptors in that the ICD binding can directly promote WRC activation. Due to the strong inhibitory effect of HPO-30 ICD in pyrene-actin polymerization assays, it will be important to develop new assays to directly measure WRC activation (e.g. by tracking WCA release) to understand how HPO-30 ICD binding enhances WRC activation by Rac1. Rac1 activates the WRC by binding to two distinct sites located on the Sra1 subunit (Chen et al., 2017; Ding et al., 2022). It is possible HPO-30 ICD promotes WRC activation by Rac1 by directly stabilizing Rac1 binding to either site or by destabilizing the sequestration of WCA.

HPO-30 to our knowledge represents the first transmembrane protein that possesses actin capping, or capping-like, activity. The abilities of HPO-30 to promote WRC membrane recruitment and activation (which stimulates Arp2/3-mediated actin polymerization) and to simultaneously cap actin filaments and inhibit actin polymerization seem to be conflicting functions. However, such capping activity, which is usually provided by cytosolic capping proteins like CapZ, are known to be essential for Arp2/3-based actin dynamics in both bead motility assays *in vitro* and many processes *in vivo* (Akin and Mullins, 2008; Miyoshi et al., 2006). It is believed that capping proteins can reserve G-actin by blocking it from accessing barbed ends and simultaneously prevent the barbed end from sequestering the WH2 region of WCA, which collectively stimulates the formation of new branches through Arp2/3. Thus, capping proteins are critical for dynamically modulating the actin architecture to generate force against the surface where actin is localized (Akin and Mullins, 2008; Funk et al., 2021) (**Figure 7**, step 2). The capping activity of HPO-30 ICD in principle should similarly stimulate the formation of a highly branched actin network. Although HPO-30 ICD apparently has lower

capping activity compared to the canonical capping protein CapZ, it has the advantage of concentrating the capping activity next to membranes to provide a more focused control of actin dynamics.

The requirement of dimerization of HPO-30 ICD for both binding the WRC and providing the capping activity suggests an intriguing regulatory mechanism of membrane proteins. Clustering of membrane receptors is a common mechanism to increase local concentration of membrane signaling (Johannes et al., 2018). Enrichment of HPO-30 at developing PVD neuron dendrites is correlated with the high level of F-actin in these branches (Zou et al., 2018). In addition to increasing HPO-30 density, clustering of HPO-30 would facilitate dimerization of its ICD, which can act as a functional switch to allow the ICD to adopt two functions: binding to the WRC and capping actin filaments. This dimerization-mediated functional switch can help the cell to distinguish signal from noise and achieve switch-like spatiotemporal control of actin polymerization in response to upstream stimuli. Given the distinct surfaces of the actin barbed end and the WRC, it is possible the dimerized HPO-30 ICD uses distinct structural mechanisms to bind the two targets. Such structural plasticity has been observed for signaling molecules with versatile functions (Bürgi et al., 2016; Dishman and Volkman, 2018). Resolving the high-resolution structures and identifying the key residues responsible for each binding event would allow us to differentiate the two functions of HPO-30, both in *in vitro* and *in vivo*.

Together, our data establish HPO-30 as the first membrane receptor that, upon dimerization, can directly integrate the activities of Arp2/3-mediated actin polymerization (resembling WIRS-containing receptors, albeit through a distinct mechanism) and actin filament capping (resembling canonical barbed end cappers like CapZ, although the exact mechanism could be different). These two distinct functions by the same membrane receptor provide an exciting model to explain how HPO-30 regulates local actin dynamics to facilitate dendrite branching (**Figure 7**). Synergistic action of both functions of HPO-30 would promote the formation of highly branched actin networks, giving rise to dendritic “swellings” observed in PVD neurons prior to dendrite branch outgrowth (**Figure 7**, step 4) (Shi et al., 2021).

Materials and Methods

Protein expression and purification

HPO-30 ICD proteins (and their associated alanine-scan mutants), including GST-ICD, ICD-GST, DLC8-ICD-His6, GB1-ICD-His6, His9-sumo-ICD, MBP-ICD, GST-ICD-mEGFP, GB1-FKBP-ICD-His6, GB1-FRB-ICD-His6, GB1-FKBP-His6, GB1-FRB-His6, SNAP-FKBP-ICD-His6, SNAP-FRB-ICD-His6, SNAP-FKBP-His6, and SNAP-FRB-His6, as well as other related proteins, including MBP-WAVE1 (1-230), MBP-WAVE1 (1-230)-WCA, MBP-WAVE1 (1-178), MBP-Abi2 (1-158), MBP-HSPC300, $(MBP)_2$-Abi2 (1-158), $(MBP)_2$-HSPC300, and $Rac1^{Q61L/P29S}$ Δ4 (herein referred to as $Rac1^{QP}$), were individually expressed in Arctic Express (DE3) RIL (Agilent) or BL21 (DE3) $T1^{R}$ (Sigma) cells after induction with 0.75 mM IPTG at 10 °C or 18 °C for 16 hours. His10-SNAP-CapZ β and CapZ α were expressed together from the pCDF Duet vector in Arctic Express (DE3) RIL (Agilent) cells after induction with 0.75 mM IPTG at 10 °C for 16 hours. GST-ICD or ICD-GST (and alanine-scan mutants) and GST-mEGFP were purified through Glutathione Sepharose beads (GE Healthcare), followed by cation exchange chromatography using a Source 15S column (GE Healthcare) at pH 7.0. MBP-ICD was purified through amylose resin (New England Biolabs), followed by cation exchange chromatography using a Source 15S column (GE Healthcare) at pH 7.0. The GST tag from GST-ICD-mEGFP and the MBP tag from MBP-ICD were removed using TEV cleavage at 4 °C overnight, followed by cation exchange chromatography using a Source 15S column (GE Healthcare) at pH 7.0. DLC8-ICD-His6, GB1-ICD-His6, His9-sumo-ICD, GB1-FKBP-ICD-His6 (and associated alanine mutant), GB1-FRB-ICD-His6 (and associated alanine mutants), GB1-FKBP-His6, GB1-FRB-His6, SNAP-FKBP-ICD-His6, SNAP-FRB-ICD-His6, SNAP-FKBP-His6, and SNAP-FRB-His6 were purified through Ni-NTA Agarose resin (Qiagen), followed by cation exchange chromatography using a Source 15S column (GE Healthcare) at pH 7.0. GST-ICD, ICD-GST, DLC8-ICD-His6, GB1-ICD-His6, His6-sumo-ICD, ICD-mEGFP, untagged ICD, GB1-FKBP-ICD-His6 (and associated alanine mutants), GB1-FRB-ICD-His6 (and associated alanine mutants), GB1-FKBP-His6, GB1-FRB-His6, SNAP-FKBP-ICD-His6, SNAP-FRB-ICD-His6, SNAP-FKBP-His6, SNAP-FRB-His6 were further purified through a Superdex 75 column (GE Healthcare). His10-SNAP-CapZ β and CapZ α were purified through Ni-NTA Agarose resin (Qiagen), followed by anion exchange chromatography using a Source 15Q column (GE Healthcare) at pH 8.0 and size exclusion chromatography on a Superdex 200

column (GE Healthcare). Rac1^{QP}Δ4 was purified by an SP-Sepharose Fast Flow column (GE Healthcare) at pH 7.0 followed by size exclusion chromatography through a Superdex 75 column.

MBP-WAVE1, MBP-Abi2, MBP-HSPC300, $(MBP)_2$-Abi2, and $(MBP)_2$-HSPC300 proteins were purified through amylose beads (New England Biolabs). His6-Sra1 and Nap1 dimer were co-expressed in Tni insect cells (Expression systems), and the dimer was purified through Ni-NTA agarose resin (Qiagen) followed by anion exchange chromatography using a Source 15Q column at pH 8.0. Pentameric WRC was assembled and purified following previously described protocols (Chen et al., 2014b, 2010). Briefly, individually purified WAVE1, Abi2, and HSPC300 subunits were mixed at equimolar ratio in the presence of 1% (w/v) NP40 and incubated on ice for 48 hours. The assembled trimer was then purified by anion exchange chromatography through a Source 15Q column at pH 8.0 and cation exchange chromatography by a Source 15S column at pH 6.0. Dimer and trimer were mixer at equimolar ratio and incubated on ice for 30 min. The assembled pentamer was purified on amylose beads (NEB), after which the MBP and His6 tags were cleaved using TEV protease incubation overnight. The pentamer was further purified using anion exchange chromatography through a Source 15Q column at pH 8.0 and size exclusion chromatography using a Superdex 200 column.

Actin was purified as previously described from rabbit muscle acetone powder from Pel-Freeze (Spudich and Watt, 1971). Actin was labeled by pyrene or Alexa Fluor® 647 after polymerization at 4 °C, using a 10-fold or 2-fold excess dye, respectively. Actin and pyrene actin for actin polymerization and depolymerization assays were kept in continuous dialysis at 4 °C, with biweekly buffer changes. Actin and Alexa Fluor® 647-labeled actin for smTIRF experiments were kept in closed tubes for two weeks.

Generation of WRC-$(MBP)_2$

To create WRC-$(MBP)_2$, MBP-Abi2 (1-158) had the sortase ligation sequence, LPGTG, genetically fused to the C-terminus. Meanwhile, a TEV site was added to the N-terminus of an $(MBP)_2$ tag, which exposes a Gly after Tev cleavage. MBP-Abi2 (1-158)-LPGTG was expressed, purified, and incorporated into the WRC as described above to create WRC-LPGTG. GG-2MBP was expressed in Arctic Express (DE3) RIL (Agilent) cells after induction with 0.75 mM IPTG at 10 °C for 16 hours, purified on amylose resin, and subjected to TEV cleavage

overnight, followed by anion exchange chromatography using a Source 15Q column (GE Healthcare). Sortase5M (sortase A pentamutant) was a gift from David Liu (Addgene plasmid # 75144), expressed in Arctic Express (DE3) RIL (Agilent) cells, purified over Ni-NTA agarose resin, followed by cation exchange using a Source 15S column (GE Healthcare) and size exclusion chromatography using a Superdex 75 column (GE Healthcare) (Chen et al., 2011). 1 µM WRC-LPGTG was mixed with 25 µM GG-MBP and 10 µM sortase in 50 mM Tris pH 7.5, 150 mM NaCl, and 10 mM $CaCl_2$ and left at room temperature for two hours. The reaction was quenched by adding 25 mM EGTA, and the WRC-$(MBP)_2$ was purified over a Superdex 200 column to separate the WRC-$(MBP)_2$ from unligated products.

Regular pull-down assay

GST pull-down assays were performed as previously described (Shi et al., 2021). Briefly, 20 µL of GSH-Sepharose beads were mixed with bait protein and prey protein in 1 mL of pull-down buffer (50 mM NaCl, 10 mM HEPES pH 7.0, 5% (w/v) glycerol, 5 mM 2-mercaptoethanol, and 0.05% Triton X-100). The samples were mixed at 4 °C for 30 minutes, washed three times with 1 mL of pull-down buffer, and eluted with 40 µL of elution buffer containing 30 mM reduced glutathione and 100 mM Tris pH 8.5. MBP pull-down assays were performed like GST pull-down assays, but used 20 µL of amylose resin and elution buffer that was pull-down buffer supplemented with 2% [w/v] maltose. His-tagged pull-down assays were performed as above, used 20 µL of Ni-NTA agarose resin, G-Buffer (2 mM Tris HCl pH 8.0, 200 µM ATP, 0.5 mM DTT, 0.1 mM $CalCl_2$, and 1mM NaN_3) as the wash buffer, and elution buffer containing 500 mM imidazole pH 7.0. In all pull-down assays, the eluant was examined by SDS-PAGE and Coomassie blue staining. In all pull-down assays using FKBP and FRB, rapamycin was added to 5 µM final concentration. As controls, the same volume of DMSO was added in place of rapamycin. For the alanine scan pull-down quantification, the intensity of the Sra1 and Nap1 bands were quantified using ImageJ. The intensity from the GST control lane was subtracted from the alanine protein lane, and the corrected intensity was divided by the intensity of the wild type HPO-30 lane. A Student's paired t-test was used to compare the wild type and each mutant separately.

Equilibrium pull-down (EPD) assay

Equilibrium pull-down assays were performed as previously described (Chen et al., 2017). Briefly, 60 µL of GSH-Sepharose beads (50% slurry equilibrated in pull-down buffer) were mixed with 0.1 µM WRC and various amounts of GST-tagged protein (from 0.01 µM to 30 µM) and brought to 100 µL with pull-down buffer (composition the same as in GST pull-down assays, above). The reactions were allowed to mix for 30 min at 4 °C, and four reactions at a time were spun at 15 krpm for 15 seconds. The supernatant was removed and examined by SDS-PAGE and Coomassie blue staining. Each assay was repeated 3 times. The Sra1/Nap1 intensity was quantified using ImageJ to calculate the fractional occupancy. The data was fitted in DynaFit using a single binding site model (Kuzmic, 1996).

Size exclusion chromatography analysis

GB1-FKBP-ICD and GB1-FRB-ICD were mixed at equimolar ratio and loaded onto a 24-mL Superdex 200 column (GE healthcare) equilibrated in 100 mM NaCl, 10 mM HEPES pH 7.0, 5% (w/v) glycerol, and 1 mM DTT, with or without 5 µM rapamycin.

Pyrene-actin polymerization assay

Pyrene-actin polymerization assays were performed as previously described (Doolittle et al., 2013a). Actin was purified and pyrene-labeled as described above and kept in continuous dialysis in G-Buffer (2 mM Tris-HCl pH 8, 0.5 mM DTT, 0.2 mM ATP, 0.1 mM $CaCl_2$, 1 mM NaN_3) that is changed twice a week. Arp2/3 was purified following existing protocols and kept aliquoted at -80°C (Doolittle et al., 2013b). All proteins except for the WRC and Arp2/3 were purified into 50KMEH5Gd (50 mM KCl, 1 mM $MgCl_2$, 1 mM EGTA, 10 mM HEPES pH 7.0, 5% [w/v] glycerol, 1 mM DTT) and stored at -80°C. WRC230VCA was purified into 100KMEI20Gd (100 mM KCl, 10 mM Imidazole pH 7.0, 20% [w/v] glycerol) and kept at -80°C. Unless otherwise noted, a typical reaction contained 2 µM actin with 10% pyrene labeled, 10 nM Arp2/3, 100 nM WRC^{230WCA} or free WCA, and /or 0.4 µM $Rac1^{QP}\Delta4$, and/or additional ICD ligands to be analyzed, with or without 5 µM rapamycin or an equivalent volume of DMSO. The excitation and emission wavelengths were set to 365 nm and 407 nm, respectively. Data were collected on a TECAN SPARK plate reader.

Actin depolymerization assay

Actin depolymerization assays were performed as previously described, with some modifications (Heiss and Cooper, 1991). Actin at ~20 µM and 70% pyrene-labeling was pre-polymerized at room temperature overnight by addition of 1 mM $MgCl_2$ and 50 mM KCl. For each depolymerization reaction, actin was diluted to 5 µM in one pooled mixture, either alone or with proteins to be tested, and left for 3 minutes at room temperature to allow for protein binding. Protein at the same concentration was prepared in a second, separate mixture. After 3 minutes, the actin was further diluted 20-fold by the addition of the second mixture. All proteins were diluted into depolymerization buffer, which is 3 parts G-Buffer and 1 part 50KMEH5Gd (see above for buffer composition). The excitation and emission wavelengths were set to 365 nm and 407 nm, respectively. Data were collected on a TECAN SPARK plate reader. To calculate the relative initial velocity, the slope for the first 30 seconds of the reaction was calculated and divided by the slope of the actin control. ANOVA on Ranks and Dunn-Tukey tests were performed to determine significance.

Circular dichroism (CD) measurement

Untagged HPO-30 ICD was purified into 100 mM NaCl, 10 mM HEPES pH 7.0, 5% (w/v) glycerol, and 1 mM DTT. The same buffer was used to dissolve BSA powder (Fisher Cat # BP1600-100) and as a blank for the CD spectrometer. The blank buffer was degassed by sonication for 3 minutes at 30% power. Data were collected on a MOS-500 fluorimeter using an ALX250 lamp. Data were collected for wavelengths between 190 nm and 260 nm, with a 1 nm step, 0.5 s acquisition period, and averaged over three repeats. Mean residue ellipticity was calculated as described previously (Greenfield, 2006). Data for BSA and HPO-30 were collected at the same concentration of protein. TMAO was dissolved to 3 M in the same buffer as HPO-30 purification and was added to the appropriate concentration before measurement. Separate buffer blanks containing the same concentration of TMAO were measured to ensure TMAO alone did not contritube to the spectrum.

Nuclear magnetic resonance (NMR) spectroscopy

Isotopically labeled proteins were expressed and purified as described for non-labeled proteins, using minimal media containing N^{15} NH_4Cl instead of traditional media. Proteins were purified into 100 mM NaCl, 10 mM HEPES pH 7.0, 5% (w/v) glycerol, 1 mM DTT and were

supplemented with 10% D_2O. Protein concentration ranged from 70 µM (GB1 tag) to 850 µM (GB1-ICD). GB1 tag was produced by thrombin cleavage of GB1-ICD and removal of ICD using nickel-NTA resin (Qiagen). NMR spectra were collected on a Bruker 700 MHz spectrometer at Iowa State University equipped with z-shielded gradient triple resonance 5 mm TCI cryoprobe. 2D ^{1}H-^{15}N TROSY-HSQC and ^{1}H-^{15}N HSQC experiments were recorded with a time domain matrix consisting of 100* (t_1, ^{15}N) × 1024* (t_2, ^{1}H) complex points with acquisition time of 50 ms (t_1) and 91.8 ms (t_2) using 16 scans per FID and 1.5 s interscan delay. Spectral widths for ^{1}H and ^{15}N dimensions were set to 15.9 and 28.2 ppm, respectively, with carriers set at 4.821 ppm (^{1}H) and 119.138 ppm (^{15}N).

Fluorophore labeling of proteins

SNAP-tagged proteins were labeled with SNAP-Surface® Alexa Fluor® 488, SNAP-Surface® Alexa Fluor® 546, and SNAP-Surface® Alexa Fluor® 647 (New England Biolabs). 5 µM protein and 10 µM dye were mixed and allowed to react in 50KMEH5Gd at room temperature for two hours, followed by desalting into 50KMEH5Gd buffer and concentration. Dye extinction coefficients were calculated from a standard curve and are as follows: Alexa 488 at 495 nm, 95000 $M^{-1}*cm^{-1}$; Alexa 546 at 556 nm, 120000 $M^{-1}*cm^{-1}$; Alexa 647 at 650 nm, 255000 $M^{-1}*cm^{-1}$. Protein labeling efficiency was calculated by dividing protein concentration by dye concentration—for Alexa Fluor® 488 the labeling efficiency was estimated at ~100%, for Alexa Fluor® 546 the labeling efficiency was estimated at ~60%.

smTIRF data collection

All time lapses were collected on a Nikon TE2000-E inverted microscope equipped with a 100x 1.49 NA TIRF objective and a TIRF Quad filter cube (Chroma C141789), using an Andor iXon3 EM-CCD (DU-897-CS0) camera, with a GATACA iLas system to prevent uneven illumination. Coverslips were prepared as described previously with slight modifications (Narvaez-Ortiz and Nolen, 2022). Briefly, glass coverslips (VWR Cat # 48393-241) were cleaned with 2% (w/v) Hellmanex, acetone, and 1 M KOH solutions with sonication, and rinsed extensively with DI water before each step and after the KOH treatment. Coverslips were rinsed with methanol and dried using a N_2 gas stream. GOPTES (Fisher Cat # G0210100G) was added to the coverslips, which were then baked at 75°C for 30 minutes. Coverslips were rinsed with

893 microscope grade acetone and dried with N_2 gas stream. A 2% (w/w) Biotin-PEG3000/NH2-
894 PEG3000 mixture of powder (Rapp Polymere GmbH) was prepared, placed on top of the
895 coverslips, and the coverslips baked overnight at 75°C. After overnight baking, the coverslips
896 were washed with water and dried with N_2 gas. Individual wells were made by placing
897 functionalized coverslips on Ibidi® sticky-Slide IV 0.4 slides (Ibidi Cat # 80608). Individual
898 lanes were prepared for microscopy by incubating with 5% (w/v) Pluronic F-127 for 10 min at
899 RT, followed by either 100 nM (for elongation rate analysis) or 35 nM (for side binding analysis)
900 neutravidin incubation (in 50 mM Tris pH 7.5, 200 mM NaCl, referred to as LS TBS for short)
901 for 10 min at RT, and either 10 nM (for elongation rate analysis) or 3.5 nM (for side binding
902 analysis) biotinylated inactivated heavy meromyosin (in LS TBS) incubation for 10 min at RT.
903 The chambers were washed with 20 mg/mL BSA in 50 mM Tris pH 7.5, 600 mM NaCl, and
904 incubated with 20 mg/mL BSA in LS TBS for 10 min at RT. Actin was diluted to a final
905 concentration of 2.1 µM with 20% Alexa-647 labeling in 1X TIRF buffer (final concentrations:
906 50 mM KCl, 2 mM $MgCl_2$, 2 mM EGTA pH 8.0, 10 mM Imidazole pH 7.0, 25 mM glucose, 1
907 mM Trolox, 0.5% methylcellulose (400 cP), 20 mM 2-mercaptoethanol, 0.4 mM ATP, 20
908 mg/mL BSA, 0.02 mg/mL catalase, 0.1 mg/mL glucose oxidase, 1 mM 4-nitrobenzyl alcohol,
909 and 0.5 mM propyl gallate) and allowed to polymerize on the slide for 5 minutes at room
910 temperature. Excess actin was removed by two washes, each time using 40 µL of 1X TIRF
911 buffer. A separate mixture of 1 µM actin with 20% Alexa-647 labeling containing desired
912 proteins in 1X TIRF buffer was then added to the wells to start data acquisition. Time lapse
913 images were acquired using the following setups. Experiments involving unlabeled HPO-30 ICD
914 and CapZ for elongation rate analysis of actin^{AF647}: 640-nm laser, 5% power, 50 ms exposure
915 time, and a 5-s interval between exposures; experiments involving CapZ^{AF488}: 488-nm laser
916 (15% power, 50 ms exposure time) and 640-nm laser (5% power, 50 ms exposure time),
917 alternating between 20 consecutive exposures in the 488-nm channel for CapZ^{AF488} and one
918 exposure in the 640-nm channel for actin^{AF647}, with a 500-ms interval between exposures;
919 experiments involving HPO-30 ICD^{AF546}: 561-nm laser (10% power, 50 or 100 ms exposure
920 time) and 640-nm laser (5% power, 50 ms exposure time), alternating between 20 consecutive
921 exposures in the 561-nm channel for ICD^{AF546} and one exposure in the 640-nm channel for
922 actin^{AF647}, with a 500-ms interval between exposures.
923

smTIRF data processing - actin elongation rate measurement

Time lapses were opened in ImageJ and the background removed using a rolling ball radius of 10 pixels. The length of actin filaments was calculated using the Filament Length ImageJ plugin, kindly provided by Jeff Kuhn, using a Gaussian-Radius of 1.5-2, determined for each individual movie (Kuhn and Pollard, 2005). The length (in microns) was converted to subunits using the established value of 370 actin subunits / μm (Huxley and Brown, 1967). Time points were taken from NIS Elements software. Filaments were only selected if they were present within the first 10 frames of the movie and did not leave the frame during the course of the video. 10 time points were selected and the length at each point was calculated, and the average slope was used for the actin elongation rate. ANOVA with Dunn-Tukey tests were used to determine significance.

smTIRF data processing - side-binding/capping analysis

Time lapses were opened in ImageJ and the background removed using a rolling ball radius of 10 pixels. Only filaments present at the beginning of the videos and those that did not leave the frame during the duration of the video were selected. Analysis was performed in a single-blinded manner. Side binding events were determined if they met the following criteria: 1) the ICD/empty tag puncta must be present for more than one frame; 2) the ICD/empty tag puncta must move with the filament at least once; 3) the filament must not move away from the ICD/empty tag puncta; 4) the HPO-30/vector puncta must be smaller than a circle with a radius of 4 pixels. Capping events were confirmed by the absence of growth with puncta present and, if available, growth from the end capped after the puncta leaves the filament. A Student's t-test was used to determine significance between ICD and tag reactions.

Actin pelleting assay

Actin pelleting assays were performed based on (Heier et al., 2017) with modifications. Actin was pre-polymerized at room temperature overnight by addition of 1X 50KMEH5Gd. Reactions (60 μL) were assembled by mixing 2 μM actin and 5 μM protein (in the same 50KMEH5Gd buffer), which were then allowed to bind at room temperature for 30 minutes. Reactions were centrifuged at 100,000 g at 4 °C for 30 min in a Type 42.2 Ti rotor in a Beckman ultracentrifuge. 40 μL of the supernatant was removed and mixed with SDS, and the remaining ~15 μL was removed and discarded. The pellet was dissolved by the addition of 40 μL of G-

buffer, followed by brief pipetting and vortexing, and allowed to sit at room temperature for 5 min before the liquid was removed and mixed with SDS PAGE loading buffer. The intensity of the supernatant and pellet bands on SDS PAGE gels were measured using ImageJ. The total intensity of the supernatant and pellet bands, and the percentage of intensity from the pellet and the supernatant were calculated. The percentage pelleted protein was calculated by subtracting the percentage of intensity from the pelleted protein in the absence of actin from the percentage of intensity from the pelleted protein in the presence of actin. For example, in Figure 5A, the intensity of BSA from lanes 1 and 2 was summed and the percentage of intensity from 1 and from 2 were calculated. This was repeated for lanes 3 and 4, then the percentage intensity of lane 2 was subtracted from lane 4. ANOVA with Dunn-Tukey tests were used to determine significance.

Actin pelleting competition assays

Actin pelleting competition assays were performed nearly identically to the actin pelleting assay described above, except that after 30 minutes of incubation of 5 µM HPO-30 ICD proteins with 2 µM actin, 600 nM CapZ was added and incubated for 5 minutes before ultracentrifugation. The intensity of the top bands for CapZ in the pellet were calculated for all reactions and corrected for the intensity of CapZ pelleted without actin. The relative intensity was calculated by dividing the intensity of the lane by CapZ with actin alone. For example, in Figure 6D, the intensity of lane 2 was subtracted from lanes 4, 6, 8, and 10. Then, the corrected intensity of lane 4 was divided by that of lane 2. ANOVA with Dunn-Tukey tests were used to determine significance.

S2 cell culture and transfection

Drosophila S2 cells were grown in Schneider's media (Thermo Fisher) supplemented with 10% heat-inactivated FBS (Life Technologies) and 50 U/mL penicillin-streptomycin (Thermo Fisher). Cells were transfected with Effectene (Qiagen) and 1ug of total plasmid (either Pactin>HPO-30:6xMyc (pXD384) or both Pactin>HPO-30:6xMyc (pXD384) and Pactin>HPO-30:HA (pXD226)).

Co-immunoprecipitation

S2 cells were harvested 72 hours after transfection. Cells were lysed in RIPA buffer (Thermo Fisher) with 1x Halt Protease Inhibitor Cocktail (Thermofisher) for 30 minutes on ice. Cell lysates were incubated with anti-HA affinity gel beads (Sigma E6779-1ML) for 1 hour at 4℃ with rotation. Proteins were eluted at 80℃ in NuPAGE LDS Sample Buffer (Life Technologies) supplemented with DTT (GoldBio) and detected using Western blot with mouse antibody to HA (1:1000, Sigma H3663), rabbit antibody to Myc (1:1000, Santa Cruz Biotechnology sc-789), and HRP-conjugated goat antibodies to mouse (1:20,000, Jackson Immuno Research).

Acknowledgements

We thank ResearchIT at Iowa State University for installing AlphaFold 2 and AlphaFold Multimer; Daniel Boesch for help with submitting AlphaFold prediction tasks; Scott Nelson at Iowa State for guidance with CD spectroscopy; Xuefeng Wang at Iowa State for the initial setup of smTIRF experiments; Aubrey Sijo-Gonzales, Finlan Rhodes, Leyuan Loh, Ganesh Prasad, Simanta Mitra, and the ResearchIT at Iowa State University for establishing a web-based application (*https://biochempy.bb.iastate.edu*) for data visualization; and Michael Rosen at UT Southwestern for sharing FKBP/FRB constructs. This work was supported by funding from the National Institutes of Health (R35-GM128786) and start-up funds from the Iowa State University and the Roy J. Carver Charitable Trust to B.C., National Institutes of Health (R35-GM136319) to B.J.N., National Institutes of Health (R01-GM132561) to J.R., Howard Hughes Medical Institute and the National Institute of Neurological Disorders and Stroke (1R01NS082208) to K.S., and the National Science Foundation Graduate Research Fellowship and a training grant from the National Institutes of Health to R.S.

Author contributions

B.C. conceived and oversaw the project. B.N. oversaw single molecule experiments. J.R. oversaw NMR experiments. D.A.K. purified proteins and performed biochemical experiments. D.A.K. performed AlphaFold predictions. D.A.K. and J.R. performed NMR measurements. D.A.K. and H.Y.N-O. performed single molecule TIRF experiments. R.S. performed co-immunoprecipitation experiments under the supervision of K.S. D.A.K. and B.C. drafted the manuscript and prepared the figures with assistance from all the authors.

Competing interests

The authors declare no competing interests.

Additional Information

Correspondence and request for materials should be addressed to stone@iastate.edu

Supplemental materials

Video 1. CapZ capping event example 1. Related to Figure 6A, top. Time lapse of $SNAP^{AF488}$-CapZ (green) bound to the end of actin filaments (red) obtained by smTIRF microscopy. Video length of 1200 frames at 120 frames per second. The filament in the top left corner is the one showcased in Figure 6A, top.

Video 2. CapZ capping event example 2. Related to Figure 6A, top. Time lapse of $SNAP^{AF488}$-CapZ (green) bound to the end of an actin filament (red) obtained by smTIRF microscopy. Video length of 1800 frames at 120 frames per second.

Video 3. HPO-30 ICD side binding event example 1. Related to Figure 6A, bottom. $SNAP^{AF546}$-F/F-ICD (cyan) bound to the side of an actin filament (red) obtained by smTIRF microscopy. Video length of 1000 frames at 100 frames per second.

Video 4. HPO-30 ICD side binding event example 2. Related to Figure 6A, bottom. $SNAP^{AF546}$-F/F-ICD (cyan) bound to the side of an actin filament (red) obtained by smTIRF microscopy. Video length of 350 frames at 35 frames per second.

Video 5. Actin elongation rate comparison. Related to Figure 6C. Representative smTIRF time lapses used to quantify the elongation rate of actin filaments. Video shows a random selection of actin filaments from each condition tested. Video length of 15 minutes and 181 frames was compressed to 9 seconds.

1048 **Supplemental Table 1: Sequences of recombinant proteins used in this study.**

Construct name	Description	Plasmid Identity	Sequence	Source or reference
GST-ICD	GST-thrombin-TEV-ceHPO-30 ICD (a.a. 229-279)	pDK079	MSPILGYWKIKGLVQPTRLLLEYLEEKYEEHLYERDEGDKWRNKKFELGLEFPNLPY YIDGDVKLTQSMAIIRYIADKHNMLGGCPKERAEISMLEGAVLDIRYGVSRIAYSKD FETLKVDFLSKLPEMLKMFEDRLCHKTYLNGDHVTHPDFMLYDALDVVLYMDPMCLD AFPKLVCFKKRIEAIPQIDKYLKSSKYIAWPLQGWQATFGGGDHPPKSDLVPRGSEN LYFQGHMTSKHAHDVCCTSRKEYREQTKWKNNGLILKTGRVNHQSHRPFVVIDDDSS M	Zou, 2018
GST-ICD Δ1	GST-thrombin-TEV-ceHPO-30 ICD Ala 229-233	pDK325	MSPILGYWKIKGLVQPTRLLLEYLEEKYEEHLYERDEGDKWRNKKFELGLEFPNLPY YIDGDVKLTQSMAIIRYIADKHNMLGGCPKERAEISMLEGAVLDIRYGVSRIAYSKD FETLKVDFLSKLPEMLKMFEDRLCHKTYLNGDHVTHPDFMLYDALDVVLYMDPMCLD AFPKLVCFKKRIEAIPQIDKYLKSSKYIAWPLQGWQATFGGGDHPPKSDLVPRGSEN LYFQGHMAAAAAHDVCCTSRKEYREQTKWKNNGLILKTGRVNHQSHRPFVVIDDDSS M	Zou, 2018
GST-ICD Δ2	GST-thrombin-TEV-ceHPO-30 ICD Ala 234-238	pDK326	MSPILGYWKIKGLVQPTRLLLEYLEEKYEEHLYERDEGDKWRNKKFELGLEFPNLPY YIDGDVKLTQSMAIIRYIADKHNMLGGCPKERAEISMLEGAVLDIRYGVSRIAYSKD FETLKVDFLSKLPEMLKMFEDRLCHKTYLNGDHVTHPDFMLYDALDVVLYMDPMCLD AFPKLVCFKKRIEAIPQIDKYLKSSKYIAWPLQGWQATFGGGDHPPKSDLVPRGSEN LYFQGHMTSKHAAAAAAATSRKEYREQTKWKNNGLILKTGRVNHQSHRPFVVIDDDSS M	Zou, 2018
GST-ICD Δ3	GST-thrombin-TEV-ceHPO-30 ICD Ala 239-243	pDK327	MSPILGYWKIKGLVQPTRLLLEYLEEKYEEHLYERDEGDKWRNKKFELGLEFPNLPY YIDGDVKLTQSMAIIRYIADKHNMLGGCPKERAEISMLEGAVLDIRYGVSRIAYSKD FETLKVDFLSKLPEMLKMFEDRLCHKTYLNGDHVTHPDFMLYDALDVVLYMDPMCLD AFPKLVCFKKRIEAIPQIDKYLKSSKYIAWPLQGWQATFGGGDHPPKSDLVPRGSEN LYFQGHMTSKHAHDVCCAAAAAAYREQTKWKNNGLILKTGRVNHQSHRPFVVIDDDSS M	Zou, 2018
GST-ICD Δ4	GST-thrombin-TEV-ceHPO-30 ICD Ala 244-248	pDK328	MSPILGYWKIKGLVQPTRLLLEYLEEKYEEHLYERDEGDKWRNKKFELGLEFPNLPY YIDGDVKLTQSMAIIRYIADKHNMLGGCPKERAEISMLEGAVLDIRYGVSRIAYSKD FETLKVDFLSKLPEMLKMFEDRLCHKTYLNGDHVTHPDFMLYDALDVVLYMDPMCLD AFPKLVCFKKRIEAIPQIDKYLKSSKYIAWPLQGWQATFGGGDHPPKSDLVPRGSEN LYFQGHMTSKHAHDVCCTSRKEAAAAAAKWKNNGLILKTGRVNHQSHRPFVVIDDDSS M	Zou, 2018
GST-ICD Δ5	GST-thrombin-TEV-ceHPO-30 ICD Ala 249-253	pDK329	MSPILGYWKIKGLVQPTRLLLEYLEEKYEEHLYERDEGDKWRNKKFELGLEFPNLPY YIDGDVKLTQSMAIIRYIADKHNMLGGCPKERAEISMLEGAVLDIRYGVSRIAYSKD FETLKVDFLSKLPEMLKMFEDRLCHKTYLNGDHVTHPDFMLYDALDVVLYMDPMCLD AFPKLVCFKKRIEAIPQIDKYLKSSKYIAWPLQGWQATFGGGDHPPKSDLVPRGSEN LYFQGHMTSKHAHDVCCTSRKEYREQTAAAAAGLILKTGRVNHQSHRPFVVIDDDSS M	Zou, 2018
GST-ICD Δ6	GST-thrombin-TEV-ceHPO-30 ICD Ala 254-258	pDK330	MSPILGYWKIKGLVQPTRLLLEYLEEKYEEHLYERDEGDKWRNKKFELGLEFPNLPY YIDGDVKLTQSMAIIRYIADKHNMLGGCPKERAEISMLEGAVLDIRYGVSRIAYSKD FETLKVDFLSKLPEMLKMFEDRLCHKTYLNGDHVTHPDFMLYDALDVVLYMDPMCLD AFPKLVCFKKRIEAIPQIDKYLKSSKYIAWPLQGWQATFGGGDHPPKSDLVPRGSEN LYFQGHMTSKHAHDVCCTSRKEYREQTKWKNNAAAAATGRVNHQSHRPFVVIDDDSS M	Zou, 2018
GST-ICD Δ7	GST-thrombin-TEV-ceHPO-30 ICD Ala 259-263	pDK331	MSPILGYWKIKGLVQPTRLLLEYLEEKYEEHLYERDEGDKWRNKKFELGLEFPNLPY YIDGDVKLTQSMAIIRYIADKHNMLGGCPKERAEISMLEGAVLDIRYGVSRIAYSKD FETLKVDFLSKLPEMLKMFEDRLCHKTYLNGDHVTHPDFMLYDALDVVLYMDPMCLD AFPKLVCFKKRIEAIPQIDKYLKSSKYIAWPLQGWQATFGGGDHPPKSDLVPRGSEN LYFQGHMTSKHAHDVCCTSRKEYREQTKWKNNGLILKAAAAAAHQSHRPFVVIDDDSS M	Zou, 2018
ICD-GST	ceHPO-30 ICD (a.a. 229-279)-GG-3C-GST	pDK238	MTSKHAHDVCCTSRKEYREQTKWKNNGLILKTGRVNHQSHRPFVVIDDDSSMGGLEV LFQGPMSPILGYWKIKGLVQPTRLLLEYLEEKYEEHLYERDEGDKWRNKKFELGLEF PNLPYYIDGDVKLTQSMAIIRYIADKHNMLGGCPKERAEISMLEGAVLDIRYGVSRI AYSKDFETLKVDFLSKLPEMLKMFEDRLCHKTYLNGDHVTHPDFMLYDALDVVLYMD PMCLDAFPKLVCFKKRIEAIPQIDKYLKSSKYIAWPLQGWQATFGGGDHPPK	This paper
ICD Δ8 - GST	ceHPO-30 ICD Ala 264-268	pDK257	MTSKHAHDVCCTSRKEYREQTKWKNNGLILKTGRVNAAAAAPFVVIDDDSSMGGLEV LFQGPMSPILGYWKIKGLVQPTRLLLEYLEEKYEEHLYERDEGDKWRNKKFELGLEF PNLPYYIDGDVKLTQSMAIIRYIADKHNMLGGCPKERAEISMLEGAVLDIRYGVSRI AYSKDFETLKVDFLSKLPEMLKMFEDRLCHKTYLNGDHVTHPDFMLYDALDVVLYMD PMCLDAFPKLVCFKKRIEAIPQIDKYLKSSKYIAWPLQGWQATFGGGDHPPK	This paper
ICD Δ9 - GST	ceHPO-30 ICD Ala 269-273	pDK258	MTSKHAHDVCCTSRKEYREQTKWKNNGLILKTGRVNHQSHRAAAAADDDSSMGGLEV LFQGPMSPILGYWKIKGLVQPTRLLLEYLEEKYEEHLYERDEGDKWRNKKFELGLEF PNLPYYIDGDVKLTQSMAIIRYIADKHNMLGGCPKERAEISMLEGAVLDIRYGVSRI AYSKDFETLKVDFLSKLPEMLKMFEDRLCHKTYLNGDHVTHPDFMLYDALDVVLYMD PMCLDAFPKLVCFKKRIEAIPQIDKYLKSSKYIAWPLQGWQATFGGGDHPPK	This paper

ICD Δ10 - GST	ceHPO-30 ICD Ala 274-279	pDK259	MTSKHAHDVCCTSRKEYREQTKWKNNGLILKTGRVNHQSHRPFVVIAAAAAAGGLEV LFQGPMSPILGYWKIKGLVQPTRLLLEYLEEKYEEHLYERDEGDKWRNKKFELGLEF PNLPYYIDGDVKLTQSMAIIRYIADKHNMLGGCPKERAEISMLEGAVLDIRYGVSRI AYSKDFETLKVDFLSKLPEMLKMFEDRLCHKTYLNGDHVTHPDFMLYDALDVVLYMD PMCLDAFPKLVCFKKRIEAIPQIDKYLKSSKYIAWPLQGWQATFGGGDHPPK	This paper
GST-ICD Δ11	GST-thrombin-TEV-ceHPO-30 ICD GGS 249-258	pDK332	MSPILGYWKIKGLVQPTRLLLEYLEEKYEEHLYERDEGDKWRNKKFELGLEFPNLPY YIDGDVKLTQSMAIIRYIADKHNMLGGCPKERAEISMLEGAVLDIRYGVSRIAYSKD FETLKVDFLSKLPEMLKMFEDRLCHKTYLNGDHVTHPDFMLYDALDVVLYMDPMCLD AFPKLVCFKKRIEAIPQIDKYLKSSKYIAWPLQGWQATFGGGDHPPKSDLVPRGSEN LYFQGHMTSKHAHDVCCTSRKEYREQTGGSGGSGGSGTGRVNHQSHRPFVVIDDDSS M	This paper
GST-ICD Δ12	GST-thrombin-TEV-ceHPO-30 ICD GGS 264-273	pDK333	MSPILGYWKIKGLVQPTRLLLEYLEEKYEEHLYERDEGDKWRNKKFELGLEFPNLPY YIDGDVKLTQSMAIIRYIADKHNMLGGCPKERAEISMLEGAVLDIRYGVSRIAYSKD FETLKVDFLSKLPEMLKMFEDRLCHKTYLNGDHVTHPDFMLYDALDVVLYMDPMCLD AFPKLVCFKKRIEAIPQIDKYLKSSKYIAWPLQGWQATFGGGDHPPKSDLVPRGSEN LYFQGHMTSKHAHDVCCTSRKEYREQTKWKNNAAAAATGRVNGGSGGSGGSGDDDSS M	This paper
GST-ICD Δ13	GST-thrombin-TEV-ceHPO-30 ICD GGS 264-275	pDK334	MSPILGYWKIKGLVQPTRLLLEYLEEKYEEHLYERDEGDKWRNKKFELGLEFPNLPY YIDGDVKLTQSMAIIRYIADKHNMLGGCPKERAEISMLEGAVLDIRYGVSRIAYSKD FETLKVDFLSKLPEMLKMFEDRLCHKTYLNGDHVTHPDFMLYDALDVVLYMDPMCLD AFPKLVCFKKRIEAIPQIDKYLKSSKYIAWPLQGWQATFGGGDHPPKSDLVPRGSEN LYFQGHMTSKHAHDVCCTSRKEYREQTGGSGGSGGSGGSGGSGGSGGSGGSGDSS M	This paper
GST-ICD Δ14	GST-thrombin-TEV-ceHPO-30 ICD GGS 229-248	pDK335	MSPILGYWKIKGLVQPTRLLLEYLEEKYEEHLYERDEGDKWRNKKFELGLEFPNLPY YIDGDVKLTQSMAIIRYIADKHNMLGGCPKERAEISMLEGAVLDIRYGVSRIAYSKD FETLKVDFLSKLPEMLKMFEDRLCHKTYLNGDHVTHPDFMLYDALDVVLYMDPMCLD AFPKLVCFKKRIEAIPQIDKYLKSSKYIAWPLQGWQATFGGGDHPPKSDLVPRGSEN LYFQGHMGGSGGSGGSGGSGGSGGSGGKWKNNGLILKTGRVNHQSHRPFVVIDDDSS M	This paper
ICD-mEGFP	GST-TEV-ceHPO-30 ICD 229-279 – GGS2-mEGFP, GST tag removed by TEV cleavage	pDK184	MSPILGYWKIKGLVQPTRLLLEYLEEKYEEHLYERDEGDKWRNKKFELGLEFPNLPY YIDGDVKLTQSMAIIRYIADKHNMLGGCPKERAEISMLEGAVLDIRYGVSRIAYSKD FETLKVDFLSKLPEMLKMFEDRLCHKTYLNGDHVTHPDFMLYDALDVVLYMDPMCLD AFPKLVCFKKRIEAIPQIDKYLKSSKYIAWPLQGWQATFGGGDHPPKSDLVPRGSEN LYFQGHMTSKHAHDVCCTSRKEYREQTKWKNNGLILKTGRVNHQSHRPFVVIDDDSS MGGSGGSMVSKGEELFTGVVPILVELDGDVNGHKFSVSGEGEGDATYGKLTLKFICT TGKLPVPWPTLVTTLTYGVQCFSRYPDHMKQHDFFKSAMPEGYVQERTIFFKDDGNY KTRAEVKFEGDTLVNRIELKGIDFKEDGNILGHKLEYNYNSHNVYIMADKQKNGIKV NFKIRHNIEDGSVQLADHYQQNTPIGDGPVLLPDNHYLSTQSKLSKDPNEKRDHMVL KEKVTAAGITLGMDELYK	This paper
ICD	MBP-TEV-ceHPO-30 ICD 229-279, MBP tag removed by TEV cleavage	pDK092	MKIEEGKLVIWINGDKGYNGLAEVGKKFEKDTGIKVTVEHPDKLEEKFPQVAATGDG PDIIFWAHDRFGGYAQSGLLAEITPDKAFQDKLYPFTWDAVRYNGKLIAYPIAVEAL SLIYNKDLLPNPPKTWEEIPALDKELKAKGKSALMFNLQEPYFTWPLIAADGGYAFK YENGKYDIKDVGVDNAGAKAGLTFLVDLIKNKHMNADTDYSIAEAAFNKGETAMTIN GPWAWSNIDTSKVNYGVTVLPTFKGQPSKPFVGVLSAGINAASPNKELAKEFLENYL LTDEGLEAVNKDKPLGAVALKSYEEELAKDPRIAATMENAQKGEIMPNIPQMSAFWY AVRTAVINAASGRQTVDEALKDAQTNSSSNNNNNNNNNNLGIEGRISEFENLYFQGH TSKHAHDVCCTSRKEYREQTKWKNNGLILKTGRVNHQSHRPFVVIDDDSSM	This paper
DLC8-ICD	DLC8-TEV-ceHPO-30 ICD 229-279-His6	pDK268	MSDRKAVIKNADMSEEMQQDAVDCATQALEKYNIEKDIAAYIKKEFDKKYNPTWHCI VGRNFGSYVTHETRHFIYFYLGQVAILLFKSGGSENLYFQGHMTSKHAHDVCCTSRK EYREQTKWKNNGLILKTGRVNHQSHRPFVVIDDDSSMHHHHHH	This paper
GB1-ICD	GB1-thrombin-ceHPO-30 ICD 229-279-His6	pDK239	MQYKLALNGKTLKGETTTEAVDAATAEKVFKQYANDNGVDGEWTYDDATKTFTVTEL VPRGSTSKHAHDVCCTSRKEYREQTKWKNNGLILKTGRVNHQSHRPFVVIDDDSSMH HHHHH	This paper
sumo-ICD	His10-Sumo-GGS-ceHPO-30 ICD 229-279	pDK219	MGHHHHHHHHHHSSGHIEGRHMASMSDSEVNQEAKPEVKPEVKPETHINLKVSDGSS EIFFKIKKTTPLRRLMEAFAKRQGKEMDSLRFLYDGIRIQADQTPEDLDMEDNDIIE AHREQIGGSTSKHAHDVCCTSRKEYREQTKWKNNGLILKTGRVNHQSHRPFVVIDDD SSM	This paper
GB1-FKBP-ICD	GB1-thrombin-FKBP-GGS3-ceHPO-30 ICD 229-279 – His6	pDK264	MQYKLALNGKTLKGETTTEAVDAATAEKVFKQYANDNGVDGEWTYDDATKTFTVTEL VPRGSHMVQVETISPGDGRTFPKRGQTCVVHYTGMLEDGKKFDSSRDRNKPFKFMLG KQEVIRGWEEGVAQMSVGQRAKLTISPDYAYGATGHPGIIPPHATLVFDVELLKLEG GSGGSGGSMTSKHAHDVCCTSRKEYREQTKWKNNGLILKTGRVNHQSHRPFVVIDDD SSMHHHHHH	This paper
GB1-FRB-ICD	GB1-thrombin-FRB-GGS3-ceHPO-30	pDK265	MQYKLALNGKTLKGETTTEAVDAATAEKVFKQYANDNGVDGEWTYDDATKTFTVTEL VPRGSHMELIRVAILWHEMWHEGLEEASRLYFGERNVKGMFEVLEPLHAMMERGPQT LKETSFNQAYGRDLMEAQEWCRKYMKSGNVKDLTQAWDLYYHVFRRISKQGGSGGSG	This paper

	ICD 229-279 – His6		GSMTSKHAHDVCCTSRKEYREQTKWKNNGLILKTGRVNHQSHRPFVVIDDDSSMHHHHHH	
GB1-FKBP	GB1-thrombin-FKBP-GGS3-His6	pDK270	MQYKLALNGKTLKGETTTEAVDAATAEKVFKQYANDNGVDGEWTYDDATKTFTVTELVPRGSHMVQVETISPGDGRTFPKRGQTCVVHYTGMLEDGKKFDSSRDRNKPFKFMLGKQEVIRGWEEGVAQMSVGQRAKLTISPDYAYGATGHPGIIPPHATLVFDVELLKLEGGSGGSGGSHHHHHH	This paper
GB1-FRB	GB1-thrombin-FRB-GGS3-His6	pDK271	MQYKLALNGKTLKGETTTEAVDAATAEKVFKQYANDNGVDGEWTYDDATKTFTVTELVPRGSHMELIRVAILWHEMWHEGLEEASRLYFGERNVKGMFEVLEPLHAMMERGPQTLKETSFNQAYGRDLMEAQEWCRKYMKSGNVKDLTQAWDLYYHVFRRISKQGGSGGSGGSGSHHHHHH	This paper
GB1-FKBP-ICD Δ5	GB1-thrombin-FKBP-GGS3-ceHPO-30 ICD Ala 249-253– His6	pDK274	MQYKLALNGKTLKGETTTEAVDAATAEKVFKQYANDNGVDGEWTYDDATKTFTVTELVPRGSHMVQVETISPGDGRTFPKRGQTCVVHYTGMLEDGKKFDSSRDRNKPFKFMLGKQEVIRGWEEGVAQMSVGQRAKLTISPDYAYGATGHPGIIPPHATLVFDVELLKLEGGSGGSGGSGSMTSKHAHDVCCTSRKEYREQTAAAAAGLILKTGRVNHQSHRPFVVIDDDSSMHHHHHH	This paper
GB1-FRB-ICD Δ5	GB1-FRB-thrombin-GGS3-ceHPO-30 ICD Ala 249-253– His6	pDK275	QYKLALNGKTLKGETTTEAVDAATAEKVFKQYANDNGVDGEWTYDDATKTFTVTELVPRGSHMELIRVAILWHEMWHEGLEEASRLYFGERNVKGMFEVLEPLHAMMERGPQTLKETSFNQAYGRDLMEAQEWCRKYMKSGNVKDLTQAWDLYYHVFRRISKQGGSGGSGGSMTSKHAHDVCCTSRKEYREQTAAAAAGLILKTGRVNHQSHRPFVVIDDDSSMHHHHHH	This paper
SNAP-FKBP-ICD	SNAP-FKBP-GGS3-ceHPO-30 ICD 229-279-His6	pDK283	MDKDCEMKRTTLDSPLGKLELSGCEQGLHEIKLLGKGTSAADAVEVPAPAAVLGGPEPLMQATAWLNAYFHQPEAIEEFPVPALHHPVFQQESFTRQVLWKLLKVVKFGEVISYQQLAALAGNPAATAAVKTALSGNPVPILIPCHRVVSSSGAAGGYEGGLAVKEWLLAHEGHRLGKPGLGPAGIGAPGSMVQVETISPGDGRTFPKRGQTCVVHYTGMLEDGKKFDSSRDRNKPFKFMLGKQEVIRGWEEGVAQMSVGQRAKLTISPDYAYGATGHPGIIPPHATLVFDVELLKLEGGSGGSGGSMTSKHAHDVCCTSRKEYREQTKWKNNGLILKTGRVNHQSHRPFVVIDDDSSMHHHHHH	https://www.addgene.org/101137/ and this paper
SNAP-FRB-ICD	SNAP-FRB-GGS3-ceHPO-30 ICD 229-279-His6	pDK281	MDKDCEMKRTTLDSPLGKLELSGCEQGLHEIKLLGKGTSAADAVEVPAPAAVLGGPEPLMQATAWLNAYFHQPEAIEEFPVPALHHPVFQQESFTRQVLWKLLKVVKFGEVISYQQLAALAGNPAATAAVKTALSGNPVPILIPCHRVVSSSGAVGGYEGGLAVKEWLLAHEGHRLGKPGLGPAGIGAPGSMELIRVAILWHEMWHEGLEEASRLYFGERNVKGMFEVLEPLHAMMERGPQTLKETSFNQAYGRDLMEAQEWCRKYMKSGNVKDLTQAWDLYYHVFRRISKQGGSGGSGGSMTSKHAHDVCCTSRKEYREQTKWKNNGLILKTGRVNHQSHRPFVVIDDDSSMHHHHHH	https://www.addgene.org/101137/ and this paper
SNAP-FKBP	SNAP-FKBP-GGS3-His6	pDK282	MDKDCEMKRTTLDSPLGKLELSGCEQGLHEIKLLGKGTSAADAVEVPAPAAVLGGPEPLMQATAWLNAYFHQPEAIEEFPVPALHHPVFQQESFTRQVLWKLLKVVKFGEVISYQQLAALAGNPAATAAVKTALSGNPVPILIPCHRVVSSSGAVGGYEGGLAVKEWLLAHEGHRLGKPGLGPAGIGAPGSMVQVETISPGDGRTFPKRGQTCVVHYTGMLEDGKKFDSSRDRNKPFKFMLGKQEVIRGWEEGVAQMSVGQRAKLTISPDYAYGATGHPGIIPPHATLVFDVELLKLEGGSGGSGGSHHHHHH	https://www.addgene.org/101137/ and this paper
SNAP-FRB	SNAP-FRB-GGS3-His6	pDK280	MDKDCEMKRTTLDSPLGKLELSGCEQGLHEIKLLGKGTSAADAVEVPAPAAVLGGPEPLMQATAWLNAYFHQPEAIEEFPVPALHHPVFQQESFTRQVLWKLLKVVKFGEVISYQQLAALAGNPAATAAVKTALSGNPVPILIPCHRVVSSSGAVGGYEGGLAVKEWLLAHEGHRLGKPGLGPAGIGAPGSMELIRVAILWHEMWHEGLEEASRLYFGERNVKGMFEVLEPLHAMMERGPQTLKETSFNQAYGRDLMEAQEWCRKYMKSGNVKDLTQAWDLYYHVFRRISKQGGSGGSGGSHHHHHH	https://www.addgene.org/101137/ and this paper
SNAP-CapZ	His9-SNAP-CapZ β / CapZ α, from *Gallus gallus*	pDK288	>His9-SNAP-CapZ β MGHHHHHHHHHHENLYFQGSEFMDKDCEMKRTTLDSPLGKLELSGCEQGLHEIKLLGKGTSAADAVEVPAPAAVLGGPEPLMQATAWLNAYFHQPEAIEEFPVPALHHPVFQQESFTRQVLWKLLKVVKFGEVISYQQLAALAGNPAATAAVKTALSGNPVPILIPCHRVVSSSGAVGGYEGGLAVKEWLLAHEGHRLGKPGLGPAGIGAPGSMSDQQLDCALDLMRRLPPQQIEKNLSDLIDLVPSLCEDLLSSVDQPLKIARDKVVGKDYLLCDYNRDGDSYRSPWSNKYDPPLEDGAMPSARLRKLEVEANNAFDQYRDLYFEGGVSSVYLWDLDHGFAGVILIKKAGDGSKKIKGCWDSIHVVEVQEKSSGRTAHYKLTSTVMLWLQTNKTGSGTMNLGGSLTRQMEKDETVSDSSPHIANIGRLVEDMENKIRSTLNEIYFGKTKDIVNGLRSIDAIPDNQKYKQLQRELSQVLTQRQIYIQPDN >CapZ α MADFEDRVSDEEKVRIAAKFITHAPPGEFNEVFNDVRLLLNNDNLLREGAAHAFAQYNMDQFTPVKIEGYDDQVLITEHGDLGNGRFLDPRNKISFKFDHLRKEASDPQPEDTESALKQWRDACDSALRAYVKDHYPNGFCTVYGKSIDGQQTIIACIESHQFQPKNFWNGRWRSEWKFTITPPTAQVAAVLKIQVHYYEDGNVQLVSHKDIQDSVQVSSDVQTAKEFIKIIENAENEYQTAISENYQTMSDTTFKALRRQLPVTRTKIDWNKILSYKIGKEMQNA	https://www.addgene.org/101137/ and this paper
Sra1	His6-TEV-hSra1 (1-1253, FL).	pDK116	MSYYHHHHHHDYDIPTTENLYFQGAMAAQVTLEDALSNVDLLEELPLPDQQPCIEPPPSSLLYQPNFNTNFEDRNAFVTGIARYIEQATVHSSMNEMLEEGQEYAVMLYTWRSCSRAIPQVKCNEQPNRVEIYEKTVEVLEPEVTKLMNFMYFQRNAIERFCGEVRRLCHA	(Ismail et al., 2009)

	His6 tag removed by TEV cleavage		ERRKDFVSEAYLITLGKFINMFAVLDELKNMKCSVKNDHSAYKRAAQFLRKMADPQS IQESQNLSMFLANHNKITQSLQQQLEVISGYEELLADIVNLCVDYYENRMYLTPSEK HMLLKVMGFGLYLMDGSVSNIYKLDAKKRINLSKIDKYFKQLQVVPLFGDMQIELAR YIKTSAHYEENKSRWTCTSSGSSPQYNICEQMIQIREDHMRFISELARYSNSEVVTG SGRQEAQKTDAEYRKLFDLALQGLQLLSQWSAHVMEVYSWKLVHPTDKYSNKDCPDS AEEYERATRYNYTSEEKFALVEVIAMIKGLQVLMGRMESVFNHAIRHTVYAALQDFS QVTLREPLRQAIKKKKNVIQSVLQAIRKTVCDWETGHEPFNDPALRGEKDPKSGFDI KVPRRAVGPSSTQLYMVRTMLESLIADKSGSKKTLRSSLEGPTILDIEKFHRESFFY THLINFSETLQQCCDLSQLWFREFFLELTMGRRIQFPIEMSMPWILTDHILETKEAS MMEYVLYSLDLYNDSAHYALTRFNKQFLYDEIEAEVNLCFDQFVYKLADQIFAYYKV MAGSLLLDKRLRSECKNQGATIHLPPSNRYETLLKQRHVQLLGRSIDLNRLITQRVS AAMYKSLELAIGRFESEDLTSIVELDGLLEINRMTHKLLSRYLTLDGFDAMFREANH NVSAPYGRITLHVFWELNYDFLPNYCYNGSTNRFVRTVLPFSQEFQRDKQPNAQPQY LHGSKALNLAYSSIYGSYRNFVGPPHFQVICRLLGYQGIAVVMEELLKVVKSLLQGT ILQYVKTLMEVMPKICRLPRHEYGSPGILEFFHHQLKDIVEYAELKTVCFQNLREVG NAILFCLLIEQSLSLEEVCDLLHAAPFQNILPRVHVKEGERLDAKMKRLESKYAPLH LVPLIERLGTPQQIAIAREGDLLTKERLCCGLSMFEVILTRIRSFLDDPIWRGPLPS NGVMHVDECVEFHRLWSAMQFVYCIPVGTHEFTVEQCFGDGLHWAGCMIIVLLGQQR RFAVLDFCYHLLKVQKHDGKDEIIKNVPLKKMVERIRKFQILNDEIITILDKYLKSG DGEGTPVEHVRCFQPPIHQSLASS	
Nap1	hNap1 (1-1128, FL)	pDK149	MSRSVLQPSQQKLAEKLTILNDRGVGMLTRLYNIKKACGDPKAKPSYLIDKNLESAV KFIVRKFPAVETRNNNQQLAQLQKEKSEILKNLALYYFTFVDVMEFKDHVCELLNTI DVCQVFFDITVNFDLTKNYLDLIITYTTLMILLSRIEERKAIIGLYNYAHEMTHGAS DREYPRLGQMIVDYENPLKKMMEEFVPHSKSLSDALISLQMVYPRRNLSADQWRNAQ LLSLISAPSTMLNPAQSDTMPCEYLSLDAMEKWIIFGFILCHGILNTDATALNLWKL ALQSSSCLSLFRDEVFHIHKAAEDLFVNIRGYNKRINDIRECKEAAVSHAGSMHRER RKFLRSALKELATVLSDQPGLLGPKALFVFMALSFARDEIIWLLRHADNMPKKSADD FIDKHIAELIFYMEELRAHVRKYGPVMQRYYVQYLSGFDAVVLNELVQNLSVCPEDE SIIMSSFVNTMTSLSVKQVEDGEVFDFRGMRLDWFRLQAYTSVSKASLGLADHRELG KMMNTIIFHTKMVDSLVEMLVETSDLSIFCFYSRAFEKMFQQCLELPSQSRYSIAFP LLCTHFMSCTHELCPEERHHIGDRSLSLCNMFLDEMAKQARNLITDICTEQCTLSDQ LLPKHCAKTISQAVNKKSKKQTGKKGEPEREKPGVESMRKNRLVVTNLDKLHTALSE LCFSINYVPNMVVWEHTFTPREYLTSHLEIRFTKSIVGMTMYNQATQEIAKPSELLT SVRAYMTVLQSIENYVQIDITRVFNNVLLQQTQHLDSHGEPTITSLYTNWYLETLLR QVSNGHIAYFPAMKAFVNLPTENELTFNAEEYSDISEMRSLSELLGPYGMKFLSESL MWHISSQVAELKKLVVENVDVLTQMRTSFDKPDQMAALFKRLSSVDSVLKRMTIIGV ILSFRSLAQEALRDVLSYHIPFLVSSIEDFKDHIPRETDMKVAMNVYELSSAAGLPC EIDPALVVALSSQKSENISPEEEYKIACLLMVFVAVSLPTLASNVMSQYSPAIEGHC NNIHCLAKAINQIAAALFTIHKGSIEDRLKEFLALASSSLLKIGQETDKTTTRNRES VYLLLDMIVQESPFLTMDLLESCFPYVLLRNAYHAVYKQSVTSSA	(Ismail et al., 2009)
WAVE1$^{230\Delta}_{WCA}$	MBP-TEV-hWAVE(1) 1-230, MBP tag removed by TEV cleavage	pDK071	MKIEEGKLVIWINGDKGYNGLAEVGKKFEKDTGIKVTVEHPDKLEEKFPQVAATGDG PDIIFWAHDRFGGYAQSGLLAEITPDKAFQDKLYPFTWDAVRYNGKLIAYPIAVEAL SLIYNKDLLPNPPKTWEEIPALDKELKAKGKSALMFNLQEPYFTWPLIAADGGYAFK YENGKYDIKDVGVDNAGAKAGLTFLVDLIKNKHMNADTDYSIAEAAFNKGETAMTIN GPWAWSNIDTSKVNYGVTVLPTFKGQPSKPFVGVLSAGINAASPNKELAKEFLENYL LTDEGLEAVNKDKPLGAVALKSYEEELAKDPRIAATMENAQKGEIMPNIPQMSAFWY AVRTAVINAASGRQTVDEALKDAQTNSSSNNNNNNNNNNLGIEGRISEFENLYFQGH MPLVKRNIDPRHLCHTALPRGIKNELECVTNISLANIIRQLSSLSKYAEDIFGELFN EAHSFSFRVNSLQERVDRLSVSVTQLDPKEEELSLQDITMRKAFRSSTIQDQQLFDR KTLPIPLQETYDVCEQPPPLNILTPYRDDGKEGLKFYTNPSYFFDLWKEKMLQDTED KRKEKRKQKQKNLDRPHEPEKVPRAPHDRRREWQKLAQGPELAEDDANLLHKHIEVA NG	(Chen et al., 2017)
WAVE1$^{230W}_{CA}$	MBP-TEV-hWAVE(1) 1-230 – GGS6 – VCA, MBP tag removed by TEV cleavage	pDK081	MKIEEGKLVIWINGDKGYNGLAEVGKKFEKDTGIKVTVEHPDKLEEKFPQVAATGDG PDIIFWAHDRFGGYAQSGLLAEITPDKAFQDKLYPFTWDAVRYNGKLIAYPIAVEAL SLIYNKDLLPNPPKTWEEIPALDKELKAKGKSALMFNLQEPYFTWPLIAADGGYAFK YENGKYDIKDVGVDNAGAKAGLTFLVDLIKNKHMNADTDYSIAEAAFNKGETAMTIN GPWAWSNIDTSKVNYGVTVLPTFKGQPSKPFVGVLSAGINAASPNKELAKEFLENYL LTDEGLEAVNKDKPLGAVALKSYEEELAKDPRIAATMENAQKGEIMPNIPQMSAFWY AVRTAVINAASGRQTVDEALKDAQTNSSSNNNNNNNNNNLGIEGRISEFENLYFQGH MPLVKRNIDPRHLCHTALPRGIKNELECVTNISLANIIRQLSSLSKYAEDIFGELFN EAHSFSFRVNSLQERVDRLSVSVTQLDPKEEELSLQDITMRKAFRSSTIQDQQLFDR KTLPIPLQETYDVCEQPPPLNILTPYRDDGKEGLKFYTNPSYFFDLWKEKMLQDTED KRKEKRKQKQKNLDRPHEPEKVPRAPHDRRREWQKLAQGPELAEDDANLLHKHIEVA NGGGSGGSGGSGGSGGSGGSKRHPSTLPVISDARSVLLEAIRKGIQLRKVEEQREQE AKHERIENDVATILSRRIAVEYSDSEDDSEFDEVDWLE	(Chen et al., 2017)
Abi2 (1-158)	MBP-TEV-hAbi(2) 1-158, MBP tag removed by TEV cleavage	pDK075	MKIEEGKLVIWINGDKGYNGLAEVGKKFEKDTGIKVTVEHPDKLEEKFPQVAATGDG PDIIFWAHDRFGGYAQSGLLAEITPDKAFQDKLYPFTWDAVRYNGKLIAYPIAVEAL SLIYNKDLLPNPPKTWEEIPALDKELKAKGKSALMFNLQEPYFTWPLIAADGGYAFK YENGKYDIKDVGVDNAGAKAGLTFLVDLIKNKHMNADTDYSIAEAAFNKGETAMTIN GPWAWSNIDTSKVNYGVTVLPTFKGQPSKPFVGVLSAGINAASPNKELAKEFLENYL LTDEGLEAVNKDKPLGAVALKSYEEELAKDPRIAATMENAQKGEIMPNIPQMSAFWY	(Ismail et al., 2009)

			AVRTAVINAASGRQTVDEALKDAQTNSSSNNNNNNNNNNLGIEGRISEFENLYFQGH MAELQMLLEEEIPGGRRALFDSYTNLERVADYCENNYIQSADKQRALEETKAYTTQS LASVAYLINTLANNVLQMLDIQASQLRRMESSINHISQTVDIHKEKVARREIGILTT NKNTSRTHKIIAPANLERPVRYIRKPIDYTILDDIGHGVKVSTQ	
Abi2 (1-158)-sortase	MBP-TEV-hAbi(2) 1-158-LPGTG, MBP tag removed by TEV cleavage	pDK255	MKIEEGKLVIWINGDKGYNGLAEVGKKFEKDTGIKVTVEHPDKLEEKFPQVAATGDG PDIIFWAHDRFGGYAQSGLLAEITPDKAFQDKLYPFTWDAVRYNGKLIAYPIAVEAL SLIYNKDLLPNPPKTWEEIPALDKELKAKGKSALMFNLQEPYFTWPLIAADGGYAFK YENGKYDIKDVGVDNAGAKAGLTFLVDLIKNKHMNADTDYSIAEAAFNKGETAMTIN GPWAWSNIDTSKVNYGVTVLPTFKGQPSKPFVGVLSAGINAASPNKELAKEFLENYL LTDEGLEAVNKDKPLGAVALKSYEEELAKDPRIAATMENAQKGEIMPNIPQMSAFWY AVRTAVINAASGRQTVDEALKDAQTNSSSNNNNNNNNNNLGIEGRISEFENLYFQGH MAELQMLLEEEIPGGRRALFDSYTNLERVADYCENNYIQSADKQRALEETKAYTTQS LASVAYLINTLANNVLQMLDIQASQLRRMESSINHISQTVDIHKEKVARREIGILTT NKNTSRTHKIIAPANLERPVRYIRKPIDYTILDDIGHGVKVSTQGGLPGTGG	This paper
$(MBP)_2$-Abi2	2MBP-Thrombin-StrepII-hAbi(2) 1-158	pDK119	MKIEEGKLVIWINGDKGYNGLAEVGKKFEKDTGIKVTVEHPDKLEEKFPQVAATGDG PDIIFWAHDRFGGYAQSGLLAEITPDKAFQDKLYPFTWDAVRYNGKLIAYPIAVEAL SLIYNKDLLPNPPKTWEEIPALDKELKAKGKSALMFNLQEPYFTWPLIAADGGYAFK YENGKYDIKDVGVDNAGAKAGLTFLVDLIKNKHMNADTDYSIAEAAFNKGETAMTIN GPWAWSNIDTSKVNYGVTVLPTFKGQPSKPFVGVLSAGINAASPNKELAKEFLENYL LTDEGLEAVNKDKPLGAVALKSYEEELAKDPRIAATMENAQKGEIMPNIPQMSAFWY AVRTAVINAASGRQTVDEALKDAQTNSSSLEWSHPQFEKAGGMKIEEGKLVIWINGD KGYNGLAEVGKKFEKDTGIKVTVEHPDKLEEKFPQVAATGDGPDIIFWAHDRFGGYA QSGLLAEITPDKAFQDKLYPFTWDAVRYNGKLIAYPIAVEALSLIYNKDLLPNPPKT WEEIPALDKELKAKGKSALMFNLQEPYFTWPLIAADGGYAFKYENGKYDIKDVGVDN AGAKAGLTFLVDLIKNKHMNADTDYSIAEAAFNKGETAMTINGPWAWSNIDTSKVNY GVTVLPTFKGQPSKPFVGVLSAGINAASPNKELAKEFLENYLLTDEGLEAVNKDKPL GAVALKSYEEELAKDPRIAATMENAQKGEIMPNIPQMSAFWYAVRTAVINAASGRQT VDEALKDAQTNSSSNNNNNNNNNNLGEFLVPRGSWSHPQFEKAGGHMAELQMLLEEE IPGGRRALFDSYTNLERVADYCENNYIQSADKQRALEETKAYTTQSLASVAYLINTL ANNVLQMLDIQASQLRRMESSINHISQTVDIHKEKVARREIGILTTNKNTSRTHKII APANLERPVRYIRKPIDYTILDDIGHGVKVSTQ	This paper
HSPC300	MBP-TEV-hHSPC300, MBP tag removed by TEV cleavage	pDK069	MKIEEGKLVIWINGDKGYNGLAEVGKKFEKDTGIKVTVEHPDKLEEKFPQVAATGDG PDIIFWAHDRFGGYAQSGLLAEITPDKAFQDKLYPFTWDAVRYNGKLIAYPIAVEAL SLIYNKDLLPNPPKTWEEIPALDKELKAKGKSALMFNLQEPYFTWPLIAADGGYAFK YENGKYDIKDVGVDNAGAKAGLTFLVDLIKNKHMNADTDYSIAEAAFNKGETAMTIN GPWAWSNIDTSKVNYGVTVLPTFKGQPSKPFVGVLSAGINAASPNKELAKEFLENYL LTDEGLEAVNKDKPLGAVALKSYEEELAKDPRIAATMENAQKGEIMPNIPQMSAFWY AVRTAVINAASGRQTVDEALKDAQTNSSSNNNNNNNNNNLGIEGRISEFENLYFQGH MGAAMAGQEDPVQREIHQDWANREYIEIITSSIKKIADFLNSFDMSCRSRLATLNEK LTALERRIEYIEARVTKGETLT	(Ismail et al., 2009)
$(MBP)_2$-HSPC300	2MBP-Thrombin-StrepII-hHSPC300	pDK118	MKIEEGKLVIWINGDKGYNGLAEVGKKFEKDTGIKVTVEHPDKLEEKFPQVAATGDG PDIIFWAHDRFGGYAQSGLLAEITPDKAFQDKLYPFTWDAVRYNGKLIAYPIAVEAL SLIYNKDLLPNPPKTWEEIPALDKELKAKGKSALMFNLQEPYFTWPLIAADGGYAFK YENGKYDIKDVGVDNAGAKAGLTFLVDLIKNKHMNADTDYSIAEAAFNKGETAMTIN GPWAWSNIDTSKVNYGVTVLPTFKGQPSKPFVGVLSAGINAASPNKELAKEFLENYL LTDEGLEAVNKDKPLGAVALKSYEEELAKDPRIAATMENAQKGEIMPNIPQMSAFWY AVRTAVINAASGRQTVDEALKDAQTNSSSLEWSHPQFEKAGGMKIEEGKLVIWINGD KGYNGLAEVGKKFEKDTGIKVTVEHPDKLEEKFPQVAATGDGPDIIFWAHDRFGGYA QSGLLAEITPDKAFQDKLYPFTWDAVRYNGKLIAYPIAVEALSLIYNKDLLPNPPKT WEEIPALDKELKAKGKSALMFNLQEPYFTWPLIAADGGYAFKYENGKYDIKDVGVDN AGAKAGLTFLVDLIKNKHMNADTDYSIAEAAFNKGETAMTINGPWAWSNIDTSKVNY GVTVLPTFKGQPSKPFVGVLSAGINAASPNKELAKEFLENYLLTDEGLEAVNKDKPL GAVALKSYEEELAKDPRIAATMENAQKGEIMPNIPQMSAFWYAVRTAVINAASGRQT VDEALKDAQTNSSSNNNNNNNNNNLGEFLVPRGSWSHPQFEKAGGHMGAAMAGQEDP VQREIHQDWANREYIEIITSSIKKIADFLNSFDMSCRSRLATLNEKLTALERRIEYI EARVTKGETLT	(Chen et al., 2014)
GG-$(MBP)_2$	MKI-GGS-TEV-GG-2MBP-TEV, N-terminal and C-terminal regions removed after TEV cleavage	pDK256	MKIGGSENLYFQGGKTEEGKLVIWINGDKGYNGLAEVGKKFEKDTGIKVTVEHPDK LEEKFPQVAATGDGPDIIFWAHDRFGGYAQSGLLAEITPDKAFQDKLYPFTWDAVRY NGKLIAYPIAVEALSLIYNKDLLPNPPKTWEEIPALDKELKAKGKSALMFNLQEPYF TWPLIAADGGYAFKYENGKYDIKDVGVDNAGAKAGLTFLVDLIKNKHMNADTDYSIA EAAFNKGETAMTINGPWAWSNIDTSKVNYGVTVLPTFKGQPSKPFVGVLSAGINAAS PNKELAKEFLENYLLTDEGLEAVNKDKPLGAVALKSYEEELAKDPRIAATMENAQKG EIMPNIPQMSAFWYAVRTAVINAASGRQTVDEALKDAQTNSSSNNGGSGGSGGSKTE EGKLVIWINGDKGYNGLAEVGKKFEKDTGIKVTVEHPDKLEEKFPQVAATGDGPDII FWAHDRFGGYAQSGLLAEITPDKAFQDKLYPFTWDAVRYNGKLIAYPIAVEALSLIY NKDLLPNPPKTWEEIPALDKELKAKGKSALMFNLQEPYFTWPLIAADGGYAFKYENG KYDIKDVGVDNAGAKAGLTFLVDLIKNKHMNADTDYSIAEAAFNKGETAMTINGPWA WSNIDTSKVNYGVTVLPTFKGQPSKPFVGVLSAGINAASPNKELAKEFLENYLLTDE GLEAVNKDKPLGAVALKSYEEELAKDPRIAATMENAQKGEIMPNIPQMSAFWYAVRT AVINAASGRQTVDEALKDAQTNSSSNNNNNNNNNLGIEGRISEFENLYFQGHMLEE	This paper

			FGSSRVDLQASLALAVVLQRRDWENPGVTQLNRLAAHPPFASWRNSEEARTDRPSQQ LRSLNGEWQLGCFGG	
Sortase 5M	Sortase 5M-His6	pDK085	MQAKPQIPKDKSKVAGYIEIPDADIKEPVYPGPATREQLNRGVSFAEENESLDDQNI SIAGHTFIDRPNYQFTNLKAAKKGSMVYFKVGNETRKYKMTSIRNVKPTAVEVLDEQ KGKDKQLTLITCDDYNEETGVWETRKIFVATEVKLEHHHHHH	https://www.addgene.org/75144/
Rac1^{QP}	hRac1$^{Q61L/P29S}$ Δ4	pDK077	MQAIKCVVVGDGAVGKTCLLISYTTNAFSGEYIPTVFDNYSANVMVDGKPVNLGLWD TAGLEDYDRLRPLSYPQTDVFLICFSLVSPASFENVRAKWYPEVRHHCPNTPIILVG TKLDLRDDKDTIEKLKEKKLTPITYPQGLAMAKEIGAVKYLECSALTQRGLKTVFDE AIRAVLCPPPVKKRKRK	This paper

1049

References

Adamczak, R., Porollo, A., Meller, J., 2004. Accurate prediction of solvent accessibility using neural networks-based regression. Proteins Struct. Funct. Genet. 56, 753–767. https://doi.org/10.1002/prot.20176

Akin, O., Mullins, R.D., 2008. Capping Protein Increases the Rate of Actin-Based Motility by Promoting Filament Nucleation by the Arp2/3 Complex. Cell 133, 841–851. https://doi.org/10.1016/j.cell.2008.04.011

Alekhina, O., Burstein, E., Billadeau, D.D., 2017. Cellular functions of WASP family proteins at a glance. J. Cell Sci. 130, 2235–2241. https://doi.org/10.1242/jcs.199570

Askelöf, P., Guthenberg, C., Jakobson, I., Mannervik, B., 1975. Purification and characterization of two glutathione S-aryltransferase activities from rat liver. Biochem. J. 147, 513–522. https://doi.org/10.1042/bj1470513

Banaszynski, L.A., Liu, C.W., Wandless, T.J., 2005. Characterization of the FKBP·Rapamycin·FRB Ternary Complex. J. Am. Chem. Soc. 127, 4715–4721. https://doi.org/10.1021/ja043277y

Baskakov, I. V, Kumar, R., Srinivasan, G., Ji, Y., Bolen, D.W., Thompson, E.B., 1999. Trimethylamine N-Oxide-induced Cooperative Folding of an Intrinsically Unfolded Transcription-activating Fragment of Human Glucocorticoid Receptor*. J. Biol. Chem. 274, 10693–10696. https://doi.org/https://doi.org/10.1074/jbc.274.16.10693

Begemann, A., Sticht, H., Begtrup, A., Vitobello, A., Faivre, L., Banka, S., Alhaddad, B., Asadollahi, R., Becker, J., Bierhals, T., Brown, K.E., Bruel, A.L., Brunet, T., Carneiro, M., Cremer, K., Day, R., Denommé-Pichon, A.S., Dyment, D.A., Engels, H., Fisher, R., Goh, E.S., Hajianpour, M.J., Haertel, L.R.M., Hauer, N., Hempel, M., Herget, T., Johannsen, J., Kraus, C., Le Guyader, G., Lesca, G., Mau-Them, F.T., McDermott, J.H., McWalter, K., Meyer, P., Õunap, K., Popp, B., Reimand, T., Riedhammer, K.M., Russo, M., Sadleir, L.G., Saenz, M., Schiff, M., Schuler, E., Syrbe, S., Van der Ven, A.T., Verloes, A., Willems, M., Zweier, C., Steindl, K., Zweier, M., Rauch, A., 2021. New insights into the clinical and molecular spectrum of the novel CYFIP2-related neurodevelopmental disorder and impairment of the WRC-mediated actin dynamics. Genet. Med. 23, 543–554. https://doi.org/10.1038/s41436-020-01011-x

Bernhofer, M., Dallago, C., Karl, T., Satagopam, V., Heinzinger, M., Littmann, M., Olenyi, T.,

Qiu, J., Schütze, K., Yachdav, G., Ashkenazy, H., Ben-Tal, N., Bromberg, Y., Goldberg, T., Kajan, L., O'Donoghue, S., Sander, C., Schafferhans, A., Schlessinger, A., Vriend, G., Mirdita, M., Gawron, P., Gu, W., Jarosz, Y., Trefois, C., Steinegger, M., Schneider, R., Rost, B., 2021. PredictProtein - Predicting protein structure and function for 29 years. Nucleic Acids Res. 49, W535–W540. https://doi.org/10.1093/nar/gkab354

Bonneau, R., Tsai, J., Ruczinski, I., Chivian, D., Rohl, C., Strauss, C.E., Baker, D., 2001. Rosetta in CASP4: progress in ab initio protein structure prediction. Proteins Suppl 5, 119–126. https://doi.org/10.1002/prot.1170

Bürgi, J., Xue, B., Uversky, V.N., van der Goot, F.G., 2016. Intrinsic Disorder in Transmembrane Proteins: Roles in Signaling and Topology Prediction. PLoS One 11, e0158594–e0158594. https://doi.org/10.1371/journal.pone.0158594

Burianek, L.E., Soderling, S.H., 2013. Under lock and key: Spatiotemporal regulation of WASP family proteins coordinates separate dynamic cellular processes. Semin. Cell Dev. Biol. 24, 258–266. https://doi.org/10.1016/j.semcdb.2012.12.005

Caldwell, J.E., Heiss, S.G., Mermall, V., Cooper, J.A., 1989. Effects of CapZ, an Actin Capping Protein of Muscle, on the Polymerization of Actin. Biochemistry 28, 8506–8514. https://doi.org/10.1021/bi00447a036

Chaudhari, K., Gorla, M., Chang, C., Kania, A., Bashaw, G.J., 2021. Robo recruitment of the wave regulatory complex plays an essential and conserved role in midline repulsion. Elife 10, 1–35. https://doi.org/10.7554/ELIFE.64474

Chen, B., Brinkmann, K., Chen, Z., Pak, C.W., Liao, Y., Shi, S., Henry, L., Grishin, N. V., Bogdan, S., Rosen, M.K., 2014a. The WAVE regulatory complex links diverse receptors to the actin cytoskeleton. Cell 156, 195–207. https://doi.org/10.1016/j.cell.2013.11.048

Chen, B., Chou, H.-T., Brautigam, C.A., Xing, W., Yang, S., Henry, L., Doolittle, L.K., Walz, T., Rosen, M.K., 2017. Rac1 GTPase activates the WAVE regulatory complex through two distinct binding sites. Elife 6, 1–22. https://doi.org/10.7554/elife.29795

Chen, B., Padrick, S.B., Henry, L., Rosen, M.K., 2014b. Biochemical reconstitution of the WAVE regulatory complex. Methods Enzymol. 540, 55–72. https://doi.org/10.1016/B978-0-12-397924-7.00004-2

Chen, I., Dorr, B.M., Liu, D.R., 2011. A general strategy for the evolution of bond-forming enzymes using yeast display. Proc. Natl. Acad. Sci. U. S. A. 108, 11399–11404.

https://doi.org/10.1073/pnas.1101046108

Chen, Z., Borek, D., Padrick, S.B., Gomez, T.S., Metlagel, Z., Ismail, A.M., Umetani, J., Billadeau, D.D., Otwinowski, Z., Rosen, M.K., 2010. Structure and control of the actin regulatory WAVE complex. Nature 468, 533–538. https://doi.org/10.1038/nature09623

Cheng, P., Poo, M., 2012. Early events in axon/dendrite polarization. Annu. Rev. Neurosci. 35, 181–201. https://doi.org/10.1146/annurev-neuro-061010-113618

Chia, P.H., Chen, B., Li, P., Rosen, M.K., Shen, K., 2014. Local F-actin network links synapse formation and axon branching. Cell 156, 208–220. https://doi.org/10.1016/j.cell.2013.12.009

Chou, F.-S., Wang, P.-S., 2016. The Arp2/3 complex is essential at multiple stages of neural development. Neurogenesis 3, e1261653. https://doi.org/10.1080/23262133.2016.1261653

Conway, O.J., Carrasquillo, M.M., Wang, X., Bredenberg, J.M., Reddy, J.S., Strickland, S.L., Younkin, C.S., Burgess, J.D., Allen, M., Lincoln, S.J., Nguyen, T., Malphrus, K.G., Soto, A.I., Walton, R.L., Boeve, B.F., Petersen, R.C., Lucas, J.A., Ferman, T.J., Cheshire, W.P., van Gerpen, J.A., Uitti, R.J., Wszolek, Z.K., Ross, O.A., Dickson, D.W., Graff-Radford, N.R., Ertekin-Taner, N., 2018. ABI3 and PLCG2 missense variants as risk factors for neurodegenerative diseases in Caucasians and African Americans. Mol. Neurodegener. 13, 1–12. https://doi.org/10.1186/s13024-018-0289-x

Cooper, J.A., Pollard, T.D., 1985. Effects of Capping Protein on the Kinetics of Actin Polymerization. Biochemistry 793–799.

Cooper, J.A., Walker, S.B., Pollard, T.D., 1983. Pyrene actin: documentation of the validity of a sensitive assay for actin polymerization. J. Muscle Res. Cell Motil. 4, 253–262. https://doi.org/10.1007/BF00712034

Dahl, J.P., Wang-Dunlop, J., Gonzales, C., Goad, M.E.P., Mark, R.J., Kwak, S.P., 2003. Characterization of the WAVE1 knock-out mouse: Implications for CNS development. J. Neurosci. 23, 3343–3352. https://doi.org/10.1523/jneurosci.23-08-03343.2003

Ding, B., Yang, S., Schaks, M., Liu, Y., Brown, A., Rottner, K., Chowdhury, S., Chen, B., 2022. Structures reveal a key mechanism of WAVE Regulatory Complex activation by Rac1 GTPase. BioRxiv [Preprint], May 10. doi: 10.1101/2022.05.10.491380.

Dishman, A.F., Volkman, B.F., 2018. Unfolding the Mysteries of Protein Metamorphosis. ACS Chem. Biol. 13, 1438–1446. https://doi.org/10.1021/acschembio.8b00276

1143 Dong, X., Liu, O.W., Howell, A.S., Shen, K., 2013. An extracellular adhesion molecule complex
1144 patterns dendritic branching and morphogenesis. Cell 155, 296.
1145 https://doi.org/10.1016/j.cell.2013.08.059
1146 Doolittle, L.K., Rosen, M.K., Padrick, S.B., 2013a. Measurement and analysis of in vitro actin
1147 polymerization. Methods Mol. Biol. 1046, 273–293. https://doi.org/10.1007/978-1-62703-
1148 538-5_16
1149 Doolittle, L.K., Rosen, M.K., Padrick, S.B., 2013b. Purification of native Arp2/3 complex from
1150 bovine thymus. Methods Mol. Biol. 1046, 231–250. https://doi.org/10.1007/978-1-62703-
1151 538-5_14
1152 Drozdetskiy, A., Cole, C., Procter, J., Barton, G.J., 2015. JPred4: a protein secondary structure
1153 prediction server. Nucleic Acids Res. 43, W389–W394. https://doi.org/10.1093/nar/gkv332
1154 Dyson, H.J., Wright, P.E., 2002. Coupling of folding and binding for unstructured proteins. Curr.
1155 Opin. Struct. Biol. 12, 54–60. https://doi.org/10.1016/S0959-440X(02)00289-0
1156 Eden, S., Rohatgi, R., Podtelejnikov, A. V., Mann, M., Kirschner, M.W., 2002. Mechanism of
1157 regulation of WAVE1-induced actin nucleation by Rac1 and Nck. Nature 418, 790–793.
1158 https://doi.org/10.1038/nature00859
1159 Evans, R., O'Neill, M., Pritzel, A., Antropova, N., Senior, A., Green, T., Žídek, A., Bates, R.,
1160 Blackwell, S., Yim, J., Ronneberger, O., Bodenstein, S., Zielinski, M., Bridgland, A.,
1161 Potapenko, A., Cowie, A., Tunyasuvunakool, K., Jain, R., Clancy, E., Kohli, P., Jumper, J.,
1162 Hassabis, D., 2022. Protein complex prediction with AlphaFold-Multimer. bioRxiv
1163 2021.10.04.463034. https://doi.org/10.1101/2021.10.04.463034
1164 Fan, L., Lu, Y., Shen, X., Shao, H., Suo, L., Wu, Q., 2018. Alpha protocadherins and Pyk2
1165 kinase regulate cortical neuron migration and cytoskeletal dynamics via rac1 GTPase and
1166 WAVE complex in mice. Elife 7, 1–26. https://doi.org/10.7554/eLife.35242
1167 Funk, J., Merino, F., Schaks, M., Rottner, K., Raunser, S., Bieling, P., 2021. A barbed end
1168 interference mechanism reveals how capping protein promotes nucleation in branched actin
1169 networks. Nat. Commun. 12. https://doi.org/10.1038/s41467-021-25682-5
1170 Gautreau, A., Ho, H. -y. H., Li, J., Steen, H., Gygi, S.P., Kirschner, M.W., 2004. Purification and
1171 architecture of the ubiquitous Wave complex. Proc. Natl. Acad. Sci. 101, 4379–4383.
1172 https://doi.org/10.1073/pnas.0400628101
1173 Goley, E.D., Welch, M.D., 2006. The ARP2/3 complex: An actin nucleator comes of age. Nat.

1174 Rev. Mol. Cell Biol. 7, 713–726. https://doi.org/10.1038/nrm2026
1175 Greenfield, N.J., 2006. Using circular dichroism spectra to estimate protein secondary structure.
1176 Nat. Protoc. 1, 2876–2890. https://doi.org/10.1038/nprot.2006.202
1177 Hansen, S.D., Zuchero, J.B., Mullins, R.D., 2013. Cytoplasmic Actin: Purification and Single
1178 Molecule Assembly Assays BT - Adhesion Protein Protocols, in: Coutts, A.S. (Ed.), .
1179 Humana Press, Totowa, NJ, pp. 145–170. https://doi.org/10.1007/978-1-62703-538-5_9
1180 Heier, J.A., Dickinson, D.J., Kwiatkowski, A. V, 2017. Measuring Protein Binding to F-actin by
1181 Co-sedimentation. J. Vis. Exp. 55613. https://doi.org/10.3791/55613
1182 Heiss, S.G., Cooper, J.A., 1991. Regulation of CapZ, an Actin Capping Protein of Chicken
1183 Muscle, by Anionic Phospholipids. Biochemistry 30, 8753–8758.
1184 https://doi.org/10.1021/bi00100a006
1185 Hotulainen, P., Hoogenraad, C.C., 2010. Actin in dendritic spines: Connecting dynamics to
1186 function. J. Cell Biol. 189, 619–629. https://doi.org/10.1083/jcb.201003008
1187 Huber, A.H., Stewart, D.B., Laurents, D. V, Nelson, W.J., Weis, W.I., 2001. The cadherin
1188 cytoplasmic domain is unstructured in the absence of beta-catenin. A possible mechanism
1189 for regulating cadherin turnover. J. Biol. Chem. 276, 12301–12309.
1190 https://doi.org/10.1074/jbc.M010377200
1191 Huber, A.H., Weis, W.I., 2001. The structure of the beta-catenin/E-cadherin complex and the
1192 molecular basis of diverse ligand recognition by beta-catenin. Cell 105, 391–402.
1193 https://doi.org/10.1016/s0092-8674(01)00330-0
1194 Huxley, H.E., Brown, W., 1967. The low-angle X-ray diagram of vertebrate striated muscle and
1195 its behaviour during contraction and rigor. J. Mol. Biol. 30, 383–434.
1196 https://doi.org/10.1016/S0022-2836(67)80046-9
1197 Ito, Y., Carss, K.J., Duarte, S.T., Hartley, T., Keren, B., Kurian, M.A., Marey, I., Charles, P.,
1198 Mendonça, C., Nava, C., Pfundt, R., Sanchis-Juan, A., van Bokhoven, H., van Essen, A.,
1199 van Ravenswaaij-Arts, C., Aitman, T., Bennett, D., Caulfield, M., Chinnery, P., Gale, D.,
1200 Koziell, A., Kuijpers, T.W., Laffan, M.A., Maher, E., Markus, H.S., Morrell, N.W.,
1201 Ouwehand, W.H., Perry, D.J., Raymond, F.L., Roberts, I., Smith, K.G.C., Thrasher, A.,
1202 Watkins, H., Williamson, C., Woods, G., Ashford, S., Bradley, J.R., Fletcher, D.,
1203 Hammerton, T., James, R., Kingston, N., Penkett, C.J., Stirrups, K., Veltman, M., Young,
1204 T., Brown, M., Clements-Brod, N., Davis, J., Dewhurst, E., Dolling, H., Erwood, M., Frary,

A., Linger, R., Martin, J.M., Papadia, S., Rehnstrom, K., Stark, H., Allsup, D., Austin, S., Bakchoul, T., Bariana, T.K., Bolton-Maggs, P., Chalmers, E., Collins, J., Collins, P., Erber, W.N., Everington, T., Favier, R., Freson, K., Furie, B., Gattens, M., Gebhart, J., Gomez, K., Greene, D., Greinacher, A., Gresele, P., Hart, D., Heemskerk, J.W.M., Henskens, Y., Kazmi, R., Keeling, D., Kelly, A.M., Lambert, M.P., Lentaigne, C., Liesner, R., Makris, M., Mangles, S., Mathias, M., Millar, C.M., Mumford, A., Nurden, P., Payne, J., Pasi, J., Peerlinck, K., Revel-Vilk, S., Richards, M., Rondina, M., Roughley, C., Schulman, S., Schulze, H., Scully, M., Sivapalaratnam, S., Stubbs, M., Tait, R.C., Talks, K., Thachil, J., Toh, C.H., Turro, E., Van Geet, C., De Vries, M., Warner, T.Q., Watson, H., Westbury, S., Furnell, A., Mapeta, R., Rayner-Matthews, P., Simeoni, I., Staines, S., Stephens, J., Watt, C., Whitehorn, D., Attwood, A., Daugherty, L., Deevi, S.V.V., Halmagyi, C., Hu, F., Matser, V., Meacham, S., Megy, K., Shamardina, O., Titterton, C., Tuna, S., Yu, P., von Ziegenweldt, J., Astle, W., Bleda, M., Carss, K.J., Gräf, S., Haimel, M., Lango-Allen, H., Richardson, S., Calleja, P., Rankin, S., Turek, W., Anderson, J., Bryson, C., Carmichael, J., McJannet, C., Stock, S., Allen, L., Ambegaonkar, G., Armstrong, R., Arno, G., Bitner-Glindzicz, M., Brady, A., Canham, N., Chitre, M., Clement, E., Clowes, V., Deegan, P., Deshpande, C., Doffinger, R., Firth, H., Flinter, F., French, C., Gardham, A., Ghali, N., Gissen, P., Grozeva, D., Henderson, R., Hensiek, A., Holden, S., Holder, M., Holder, S., Hurst, J., Josifova, D., Krishnakumar, D., Kurian, M.A., Lees, M., MacLaren, R., Maw, A., Mehta, S., Michaelides, M., Moore, A., Murphy, E., Park, S.M., Parker, A., Patch, C., Paterson, J., Rankin, J., Reid, E., Rosser, E., Sanchis-Juan, A., Sandford, R., Santra, S., Scott, R., Sohal, A., Stein, P., Thomas, E., Thompson, D., Tischkowitz, M., Vogt, J., Wakeling, E., Wassmer, E., Webster, A., Ali, Sonia, Ali, Souad, Boggard, H.J., Church, C., Coghlan, G., Cookson, V., Corris, P.A., Creaser-Myers, A., DaCosta, R., Dormand, N., Eyries, M., Gall, H., Ghataorhe, P.K., Ghio, S., Ghofrani, A., Gibbs, J.S.R., Girerd, B., Greenhalgh, A., Hadinnapola, C., Houweling, A.C., Humbert, M., in't Veld, A.H., Kennedy, F., Kiely, D.G., Kovacs, G., Lawrie, A., Ross, R.V.M., Machado, R., Masati, L., Meehan, S., Moledina, S., Montani, D., Othman, S., Peacock, A.J., Pepke-Zaba, J., Pollock, V., Polwarth, G., Ranganathan, L., Rhodes, C.J., Rue-Albrecht, K., Schotte, G., Shipley, D., Soubrier, F., Southgate, L., Scelsi, L., Suntharalingam, J., Tan, Y., Toshner, M., Treacy, C.M., Trembath, R., Noordegraaf, A.V., Walker, Sara, Wanjiku, I., Wharton, J., Wilkins,

M., Wort, S.J., Yates, K., Alachkar, H., Antrobus, R., Arumugakani, G., Bacchelli, C., Baxendale, H., Bethune, C., Bibi, S., Booth, C., Browning, M., Burns, S., Chandra, A., Cooper, N., Davies, S., Devlin, L., Drewe, E., Edgar, D., Egner, W., Ghurye, R., Gilmour, K., Goddard, S., Gordins, P., Grigoriadou, S., Hackett, S., Hague, R., Harper, L., Hayman, G., Herwadkar, A., Huissoon, A., Jolles, S., Kelleher, P., Kumararatne, D., Lear, S., Longhurst, H., Lorenzo, L., Maimaris, J., Manson, A., McDermott, E., Murng, S., Nejentsev, S., Noorani, S., Oksenhendler, E., Ponsford, M., Qasim, W., Quinti, I., Richter, A., Samarghitean, C., Sargur, R., Savic, S., Seneviratne, S., Sewell, C., Staples, E., Stauss, H., Thaventhiran, J., Thomas, M., Welch, S., Willcocks, L., Yeatman, N., Yong, P., Ancliff, P., Babbs, C., Layton, M., Louka, E., McGowan, S., Mead, A., Roy, N., Chambers, J., Dixon, P., Estiu, C., Hague, B., Marschall, H.U., Simpson, M., Chong, S., Emmerson, I., Ginsberg, L., Gosal, D., Hadden, R., Horvath, R., Mahdi-Rogers, M., Manzur, A., Marshall, A., Matthews, E., McCarthy, M., Reilly, M., Renton, T., Rice, A., Themistocleous, A., Vale, T., Van Zuydam, N., Walker, Suellen, Ormondroyd, L., Hudson, G., Wei, W., Yu Wai Man, P., Whitworth, J., Afzal, M., Colby, E., Saleem, M., Alavijeh, O.S., Cook, H.T., Johnson, S., Levine, A.P., Wong, E.K.S., Tan, R., Boycott, K.M., MacKenzie, A., Majewski, J., Brudno, M., Bulman, D., Dyment, D., Boycott, K.M., Kernohan, K.D., Dyack, S., Raymond, F.L., 2018. De Novo Truncating Mutations in WASF1 Cause Intellectual Disability with Seizures. Am. J. Hum. Genet. 103, 144–153. https://doi.org/10.1016/j.ajhg.2018.06.001

Jan, Y.-N., Jan, L.Y., 2003. The Control of Dendrite Development. Neuron 40, 229–242. https://doi.org/https://doi.org/10.1016/S0896-6273(03)00631-7

Johannes, L., Pezeshkian, W., Ipsen, J.H., Shillcock, J.C., 2018. Clustering on Membranes: Fluctuations and More. Trends Cell Biol. 28, 405–415. https://doi.org/10.1016/j.tcb.2018.01.009

Jumper, J., Evans, R., Pritzel, A., Green, T., Figurnov, M., Ronneberger, O., Tunyasuvunakool, K., Bates, R., Žídek, A., Potapenko, A., Bridgland, A., Meyer, C., Kohl, S.A.A., Ballard, A.J., Cowie, A., Romera-Paredes, B., Nikolov, S., Jain, R., Adler, J., Back, T., Petersen, S., Reiman, D., Clancy, E., Zielinski, M., Steinegger, M., Pacholska, M., Berghammer, T., Bodenstein, S., Silver, D., Vinyals, O., Senior, A.W., Kavukcuoglu, K., Kohli, P., Hassabis, D., 2021. Highly accurate protein structure prediction with AlphaFold. Nature 596, 583–

589. https://doi.org/10.1038/s41586-021-03819-2

Källberg, M., Wang, H., Wang, S., Peng, J., Wang, Z., Lu, H., Xu, J., 2012. Template-based protein structure modeling using the RaptorX web server. Nat. Protoc. 7, 1511–1522. https://doi.org/10.1038/nprot.2012.085

Kirkpatrick, S.L., Goldberg, L.R., Yazdani, N., Babbs, R.K., Wu, J., Reed, E.R., Jenkins, D.F., Bolgioni, A.F., Landaverde, K.I., Luttik, K.P., Mitchell, K.S., Kumar, V., Johnson, W.E., Mulligan, M.K., Cottone, P., Bryant, C.D., 2017. Cytoplasmic FMR1-Interacting Protein 2 Is a Major Genetic Factor Underlying Binge Eating. Biol. Psychiatry 81, 757–769. https://doi.org/10.1016/j.biopsych.2016.10.021

Kobayashi, K., Kuroda, S., Fukata, M., Nakamura, T., Nagase, T., Nomura, N., Matsuura, Y., Yoshida-Kubomura, N., Iwamatsu, A., Kaibuchi, K., 1998. p140Sra-1 (specifically Rac1-associated protein) is a novel specific target for Rac1 small GTPase. J. Biol. Chem. 273, 291–295. https://doi.org/10.1074/jbc.273.1.291

Koronakis, V., Hume, P.J., Humphreys, D., Liu, T., Horning, O., Jensen, O.N., McGhie, E.J., 2011. WAVE regulatory complex activation by cooperating GTPases Arf and Rac1. Proc. Natl. Acad. Sci. 108, 14449–14454. https://doi.org/10.1073/pnas.1107666108

Kouyama, T., Mihashi, K., 1981. Fluorimetry study of N-(1-pyrenyl)iodoacetamide-labelled F-actin. Local structural change of actin protomer both on polymerization and on binding of heavy meromyosin. Eur. J. Biochem. 114, 33–38.

Kramer, D.A., Piper, H.K., Chen, B., 2022. WASP family proteins : Molecular mechanisms and implications in human disease. Eur. J. Cell Biol. 101. https://doi.org/10.1016/j.ejcb.2022.151244

Kuhn, J.R., Pollard, T.D., 2005. Real-time measurements of actin filament polymerization by total internal reflection fluorescence microscopy. Biophys. J. 88, 1387–1402. https://doi.org/10.1529/biophysj.104.047399

Kumar, V., Kim, K., Joseph, C., Kourrich, S., Yoo, S.-H., Huang, H.C., Vitaterna, M.H., de Villena, F.P.-M., Churchill, G., Bonci, A., Takahashi, J.S., 2013. C57BL/6N Mutation in Cytoplasmic FMRP interacting protein 2 Regulates Cocaine Response. Science (80-.). 342, 1508–1512.

Kuzmic, P., 1996. Program DYNAFIT for the analysis of enzyme kinetic data: application to HIV proteinase. Anal. Biochem. 237, 260–273. https://doi.org/10.1006/abio.1996.0238

1298 Lebensohn, A.M., Kirschner, M.W., 2009. Activation of the WAVE Complex by Coincident
1299 Signals Controls Actin Assembly. Mol. Cell 36, 512–524.
1300 https://doi.org/10.1016/j.molcel.2009.10.024
1301 Lee, N.K., Fok, K.W., White, A., Wilson, N.H., O'Leary, C.J., Cox, H.L., Michael, M., Yap,
1302 A.S., Cooper, H.M., 2016. Neogenin recruitment of the WAVE regulatory complex
1303 maintains adherens junction stability and tension. Nat. Commun. 7.
1304 https://doi.org/10.1038/ncomms11082
1305 Lefebvre, J.L., Sanes, J.R., Kay, J.N., 2015. Development of Dendritic Form and Function.
1306 Annu. Rev. Cell Dev. Biol. 31, 741–777. https://doi.org/10.1146/annurev-cellbio-100913-
1307 013020
1308 Machesky, L.M., Atkinson, S.J., Ampe, C., Vandekerckhove, J., Pollard, T.D., Vandekercldaove,
1309 J., 1994. Purification of a cortical complex containing two unconventional actins from
1310 Acanthamoeba by affinity chromatography on profilin-agarose. J. Cell Biol. 127, 107–115.
1311 https://doi.org/10.1083/jcb.127.1.107
1312 Machesky, L.M., Insall, R.H., 1998. Scar1 and the related Wiskott-Aldrich syndrome protein,
1313 WASP, regulate the actin cytoskeleton through the Arp2/3 complex. Curr. Biol. 8, 1347–
1314 1356. https://doi.org/10.1016/S0960-9822(98)00015-3
1315 McGuffin, L.J., Bryson, K., Jones, D.T., 2000. The PSIPRED protein structure prediction server
1316 . Bioinformatics 16, 404–405. https://doi.org/10.1093/bioinformatics/16.4.404
1317 Minkyung, B., Frank, D., Ivan, A., Justas, D., Sergey, O., Rie, L.G., Jue, W., Qian, C., N., K.L.,
1318 Dustin, S.R., Claudia, M., Hahnbeom, P., Carson, A., R., G.C., Andy, D., H., P.J., V., R.A.,
1319 A., van D.A., C., E.A., J., O.D., Theo, S., Christoph, B., Tea, P.-K., K., R.M., Udit, D., K.,
1320 Y.C., E., B.J., Christopher, G.K., V., G.N., D., A.P., J., R.R., David, B., 2021. Accurate
1321 prediction of protein structures and interactions using a three-track neural network. Science
1322 (80-.). 373, 871–876. https://doi.org/10.1126/science.abj8754
1323 Miyoshi, T., Tsuji, T., Higashida, C., Hertzog, M., Fujita, A., Narumiya, S., Scita, G., Watanabe,
1324 N., 2006. Actin turnover-dependent fast dissociation of capping protein in the dendritic
1325 nucleation actin network: Evidence of frequent filament severing. J. Cell Biol. 175, 947–
1326 955. https://doi.org/10.1083/jcb.200604176
1327 Narvaez-Ortiz, H.Y., Nolen, B.J., 2022. Unconcerted conformational changes in Arp2/3 complex
1328 integrate multiple activating signals to assemble functional actin networks. Curr. Biol. 32,

975-987.e6. https://doi.org/10.1016/j.cub.2022.01.004

Olive, C., Ibanez, L., Farias, F.H.G., Wang, F., John, P., Norton, J.B., Gentsch, J., Morris, J.C., Li, Z., Del-aguila, J., Bergmann, K., Bradley, J., Benitez, B.A., Harari, O., Fagan, A., Ances, B., Cruchaga, C., Victoria, M., 2020. Examination of the Effect of Rare Variants in TREM2, ABI3, and PLCG2 in LOAD Through Multiple Phenotypes. J. Alzheimers Dis. 77, 1469–1482. https://doi.org/10.3233/JAD-200019.Examination

Pilpel, Y., Segal, M., 2005. Rapid WAVE dynamics in dendritic spines of cultured hippocampal neurons is mediated by actin polymerization. J. Neurochem. 95, 1401–1410. https://doi.org/10.1111/j.1471-4159.2005.03467.x

Polesskaya, A., Boutillon, A., Yang, S., Wang, Y., Romero, S., Liu, Y., Lavielle, M., Vacher, S., Schnitzler, A., Molinie, N., Rocques, N., Fokin, A., Guérois, R., Bièche, I., Chen, B., David, N.B., Gautreau, A.M., 2021. CYFIP2-containing WAVE complexes inhibit cell migration by a competition mechanism. bioRxiv 2020.07.02.184655.

Pollard, T.D., 2010. A Guide to Simple and Informative Binding Assays. Mol. Biol. Cell 21, 4061–4067. https://doi.org/10.1091/mbc.e10-08-0683

Pollard, T.D., 2007. Regulation of Actin Filament Assembly by Arp2/3 Complex and Formins. Annu. Rev. Biophys. Biomol. Struct. 36, 451–477. https://doi.org/10.1146/annurev.biophys.35.040405.101936

Pollitt, A.Y., Insall, R.H., 2009. WASP and SCAR/WAVE proteins: the drivers of actin assembly. J. Cell Sci. 122, 2575–2578. https://doi.org/10.1242/jcs.023879

Racz, B., Weinberg, R.J., 2008. Organization of the Arp2/3 Complex in Hippocampal Spines. J. Neurosci. 28, 5654–5659. https://doi.org/10.1523/jneurosci.0756-08.2008

Rottner, K., Stradal, T.E.B., Chen, B., 2021. WAVE regulatory complex. Curr. Biol. 31, R512–R517. https://doi.org/10.1016/j.cub.2021.01.086

Scott, E.K., Luo, L., 2001. How do dendrites take their shape? Nat. Neurosci. 4, 359–365. https://doi.org/10.1038/86006

Shi, R., Kramer, D.A., Chen, B., Shen, K., 2021. A two-step actin polymerization mechanism drives dendrite branching. Neural Dev. 16, 1–16. https://doi.org/10.1186/s13064-021-00154-0

Shimojima Yamamoto, K., Yanagishita, T., Yamamoto, H., Miyamoto, Y., Nagata, M., Ishihara, Y., Miyashita, Y., Asano, Y., Sakata, Y., Yamamoto, T., 2021. Recurrent de novo

pathogenic variant of WASF1 in a Japanese patient with neurodevelopmental disorder with absent language and variable seizures. Hum. Genome Var. 8, 7–9. https://doi.org/10.1038/s41439-021-00176-4

Sims, R., Van Der Lee, S.J., Naj, A.C., Bellenguez, C., Badarinarayan, N., Jakobsdottir, J., Kunkle, B.W., Boland, A., Raybould, R., Bis, J.C., Martin, E.R., Grenier-Boley, B., Heilmann-Heimbach, S., Chouraki, V., Kuzma, A.B., Sleegers, K., Vronskaya, M., Ruiz, A., Graham, R.R., Olaso, R., Hoffmann, P., Grove, M.L., Vardarajan, B.N., Hiltunen, M., Nöthen, M.M., White, C.C., Hamilton-Nelson, K.L., Epelbaum, J., Maier, W., Choi, S.H., Beecham, G.W., Dulary, C., Herms, S., Smith, A.G.A. V., Funk, C.C., Derbois, C., Forstner, A.J., Ahmad, S., Li, H., Bacq, D., Harold, D., Satizabal, C.L., Valladares, O., Squassina, A., Thomas, R., Brody, J.A., Qu, L., Sánchez-Juan, P., Morgan, T., Wolters, F.J., Zhao, Y., Garcia, F.S., Denning, N., Fornage, M., Malamon, J., Naranjo, M.C.D., Majounie, E., Mosley, T.H., Dombroski, B., Wallon, D., Lupton, M.K., Dupuis, J., Whitehead, P., Fratiglioni, L., Medway, C., Jian, X., Mukherjee, S., Keller, L., Brown, K., Lin, H., Cantwell, L.B., Panza, F., McGuinness, B., Moreno-Grau, S., Burgess, J.D., Solfrizzi, V., Proitsi, P., Adams, H.H., Allen, M., Seripa, D., Pastor, P., Cupples, L.A., Price, N.D., Hannequin, D., Frank-García, A., Levy, D., Chakrabarty, P., Caffarra, P., Giegling, I., Beiser, A.S., Giedraitis, V., Hampel, H., Garcia, M.E., Wang, X., Lannfelt, L., Mecocci, P., Eiriksdottir, G., Crane, P.K., Pasquier, F., Boccardi, V., Henández, I., Barber, R.C., Scherer, M., Tarraga, L., Adams, P.M., Leber, M., Chen, Y., Albert, M.S., Riedel-Heller, S., Emilsson, V., Beekly, D., Braae, A., Schmidt, R., Blacker, D., Masullo, C., Schmidt, H., Doody, R.S., Spalletta, G., Jr, W.T.L., Fairchild, T.J., Bossù, P., Lopez, O.L., Frosch, M.P., Sacchinelli, E., Ghetti, B., Yang, Q., Huebinger, R.M., Jessen, F., Li, S., Kamboh, M.I., Morris, J.C., Sotolongo-Grau, O., Katz, M.J., Corcoran, C., Dunstan, M., Braddel, A., Thomas, C., Meggy, A., Marshall, R., Gerrish, A., Chapman, J., Aguilar, M., Taylor, S., Hill, M., Fairén, M.D., Hodges, A., Vellas, B., Soininen, H., Kloszewska, I., Daniilidou, M., Uphill, J., Patel, Y., Hughes, J.T., Lord, J., Turton, J., Hartmann, A.M., Cecchetti, R., Fenoglio, C., Serpente, M., Arcaro, M., Caltagirone, C., Orfei, M.D., Ciaramella, A., Pichler, S., Mayhaus, M., Gu, W., Lleó, A., Fortea, J., Blesa, R., Barber, I.S., Brookes, K., Cupidi, C., Maletta, R.G., Carrell, D., Sorbi, S., Moebus, S., Urbano, M., Pilotto, A., Kornhuber, J., Bosco, P., Todd, S., Craig, D., Johnston, J., Gill, M., Lawlor, B., Lynch, A.,

Fox, N.C., Hardy, J., Albin, R.L., Apostolova, L.G., Arnold, S.E., Asthana, S., Atwood, C.S., Baldwin, C.T., Barnes, L.L., Barral, S., Beach, T.G., Becker, J.T., Bigio, E.H., Bird, T.D., Boeve, B.F., Bowen, J.D., Boxer, A., Burke, J.R., Burns, J.M., Buxbaum, J.D., Cairns, N.J., Cao, C., Carlson, C.S., Carlsson, C.M., Carney, R.M., Carrasquillo, M.M., Carroll, S.L., Diaz, C.C., Chui, H.C., Clark, D.G., Cribbs, D.H., Crocco, E.A., Decarli, C., Dick, M., Duara, R., Evans, D.A., Faber, K.M., Fallon, K.B., Fardo, D.W., Farlow, M.R., Ferris, S., Foroud, T.M., Galasko, D.R., Gearing, M., Geschwind, D.H., Gilbert, J.R., Graff-Radford, N.R., Green, R.C., Growdon, J.H., Hamilton, R.L., Harrell, L.E., Honig, L.S., Huentelman, M.J., Hulette, C.M., Hyman, B.T., Jarvik, G.P., Abner, E., Jin, L.W., Jun, G., Karydas, A., Kaye, J.A., Kim, R., Kowall, N.W., Kramer, J.H., Laferla, F.M., Lah, J.J., Leverenz, J.B., Levey, A.I., Li, G., Lieberman, A.P., Lunetta, K.L., Lyketsos, C.G., Marson, D.C., Martiniuk, F., Mash, D.C., Masliah, E., McCormick, W.C., McCurry, S.M., McDavid, A.N., McKee, A.C., Mesulam, M., Miller, B.L., Miller, C.A., Miller, J.W., Murrell, J.R., Myers, A.J., O'Bryant, S., Olichney, J.M., Pankratz, V.S., Parisi, J.E., Paulson, H.L., Perry, W., Peskind, E., Pierce, A., Poon, W.W., Potter, H., Quinn, J.F., Raj, A., Raskind, M., Reisberg, B., Reitz, C., Ringman, J.M., Roberson, E.D., Rogaeva, E., Rosen, H.J., Rosenberg, R.N., Sager, M.A., Saykin, A.J., Schneider, J.A., Schneider, L.S., Seeley, W.W., Smith, A.G.A. V., Sonnen, J.A., Spina, S., Stern, R.A., Swerdlow, R.H., Tanzi, R.E., Thornton-Wells, T.A., Trojanowski, J.Q., Troncoso, J.C., Van Deerlin, V.M., Van Eldik, L.J., Vinters, H. V., Vonsattel, J.P., Weintraub, S., Welsh-Bohmer, K.A., Wilhelmsen, K.C., Williamson, J., Wingo, T.S., Woltjer, R.L., Wright, C.B., Yu, C.E., Yu, L., Garzia, F., Golamaully, F., Septier, G., Engelborghs, S., Vandenberghe, R., De Deyn, P.P., Fernadez, C.M., Benito, Y.A., Thonberg, H., Forsell, C., Lilius, L., Kinhult-Stählbom, A., Kilander, L., Brundin, R., Concari, L., Helisalmi, S., Koivisto, A.M., Haapasalo, A., Dermecourt, V., Fievet, N., Hanon, O., Dufouil, C., Brice, A., Ritchie, K., Dubois, B., Himali, J.J., Keene, C.D., Tschanz, J., Fitzpatrick, A.L., Kukull, W.A., Norton, M., Aspelund, T., Larson, E.B., Munger, R., Rotter, J.I., Lipton, R.B., Bullido, M.J., Hofman, A., Montine, T.J., Coto, E., Boerwinkle, E., Petersen, R.C., Alvarez, V., Rivadeneira, F., Reiman, E.M., Gallo, M., O'Donnell, C.J., Reisch, J.S., Bruni, A.C., Royall, D.R., Dichgans, M., Sano, M., Galimberti, D., St George-Hyslop, P., Scarpini, E., Tsuang, D.W., Mancuso, M., Bonuccelli, U., Winslow, A.R., Daniele, A., Wu, C.K., Peters, O., Nacmias, B.,

1422 Riemenschneider, M., Heun, R., Brayne, C., Rubinsztein, D.C., Bras, J., Guerreiro, R., Al-
1423 Chalabi, A., Shaw, C.E., Collinge, J., Tsolaki, M., Clarimón, J., Sussams, R., Lovestone, S.,
1424 O'Donovan, M.C., Owen, M.J., Behrens, T.W., Mead, S., Uitterlinden, A.G., Holmes, C.,
1425 Cruchaga, C., Ingelsson, M., Bennett, D.A., Powell, J., Golde, T.E., Graff, C., De Jager,
1426 P.L., Morgan, K., Ertekin-Taner, N., Combarros, O., Psaty, B.M., Passmore, P., Younkin,
1427 S.G., Berr, C., Gudnason, V., Rujescu, D., Dickson, D.W., Dartigues, J.F., Destefano, A.L.,
1428 Ortega-Cubero, S., Hakonarson, H., Campion, D., Boada, M., Kauwe, J.K., Farrer, L.A.,
1429 Van Broeckhoven, C., Ikram, M.A., Jones, L., Haines, J.L., Tzourio, C., Tzourio, C.,
1430 Escott-Price, V., Mayeux, R., Deleuze, J.F., Amin, N., Goate, A.M., Pericak-Vance, M.A.,
1431 Amouyel, P., Van Duijn, C.M., Ramirez, A., Wang, L.S., Lambert, J.C., Seshadri, S.,
1432 Williams, J., Schellenberg, G.D., 2017. Rare coding variants in PLCG2, ABI3, and TREM2
1433 implicate microglial-mediated innate immunity in Alzheimer's disease. Nat. Genet. 49,
1434 1373–1384. https://doi.org/10.1038/ng.3916
1435 Soderling, S.H., Guire, E.S., Kaech, S., White, J., Zhang, F., Schutz, K., Langeberg, L.K.,
1436 Banker, G., Raber, J., Scott, J.D., 2007. A WAVE-1 and WRP Signaling Complex
1437 Regulates Spine Density, Synaptic Plasticity, and Memory. J. Neurosci. 27, 355–365.
1438 https://doi.org/10.1523/jneurosci.3209-06.2006
1439 Soderling, S.H., Langeberg, L.K., Soderling, J.A., Davee, S.M., Simerly, R., Raber, J., Scott,
1440 J.D., H., S.S., K., L.L., A., S.J., M., D.S., Richard, S., Jacob, R., D., S.J., 2003. Loss of
1441 WAVE-1 causes sensorimotor retardation and reduced learning and memory in mice. Proc.
1442 Natl. Acad. Sci. 100, 1723–1728. https://doi.org/10.1073/pnas.0438033100
1443 Spudich, J.A., Watt, S., 1971. The Regulation of Rabbit Skeletal Muscle Contraction. J. Biol.
1444 Chem. 246, 4866–4871. https://doi.org/10.1016/s0021-9258(18)62016-2
1445 Srivastava, S., Macke, E.L., Swanson, L.C., Coulter, D., Klee, E.W., Mullegama, S. V., Xie, Y.,
1446 Lanpher, B.C., Bedoukian, E.C., Skraban, C.M., Villard, L., Milh, M., Leppert, M.L.O.,
1447 Cohen, J.S., 2021. Expansion of the genotypic and phenotypic spectrum of wasf1-related
1448 neurodevelopmental disorder. Brain Sci. 11, 1–10.
1449 https://doi.org/10.3390/brainsci11070931
1450 Stephan, R., Gohl, C., Fleige, A., Klämbt, C., Bogdan, S., 2011. Membrane-targeted WAVE
1451 mediates photoreceptor axon targeting in the absence of the WAVE complex in Drosophila.
1452 Mol. Biol. Cell 22, 4079–4092. https://doi.org/10.1091/mbc.E11-02-0121

1453 Tahirovic, S., Hellal, F., Neukirchen, D., Hindges, R., Garvalov, B.K., Flynn, K.C., Stradal, T.E.,
1454 Chrostek-Grashoff, A., Brakebusch, C., Bradke, F., 2010. Rac1 regulates neuronal
1455 polarization through the WAVE complex. J. Neurosci. 30, 6930–6943.
1456 https://doi.org/10.1523/JNEUROSCI.5395-09.2010
1457 Takenawa, T., Suetsugu, S., 2007. The WASP-WAVE protein network: Connecting the
1458 membrane to the cytoskeleton. Nat. Rev. Mol. Cell Biol. 8, 37–48.
1459 https://doi.org/10.1038/nrm2069
1460 Tang, L.T., Diaz-Balzac, C.A., Rahman, M., Ramirez-Suarez, N.J., Salzberg, Y., Lázaro-Peña,
1461 M.I., Bülow, H.E., 2019. TIAM-1/GEF can shape somatosensory dendrites independently
1462 of its GEF activity by regulating F-actin localization. Elife 8, 1–27.
1463 https://doi.org/10.7554/elife.38949
1464 Tavosanis, G., 2012. Dendritic structural plasticity. Dev. Neurobiol. 72, 73–86.
1465 https://doi.org/10.1002/dneu.20951
1466 Turjanski, A.G., Gutkind, J.S., Best, R.B., Hummer, G., 2008. Binding-Induced Folding of a
1467 Natively Unstructured Transcription Factor. PLOS Comput. Biol. 4, e1000060.
1468 Wang, W., Lo, K.W.-H., Kan, H.-M., Fan, J.-S., Zhang, M., 2003. Structure of the monomeric 8-
1469 kDa dynein light chain and mechanism of the domain-swapped dimer assembly. J. Biol.
1470 Chem. 278, 41491–41499. https://doi.org/10.1074/jbc.M307118200
1471 Wang, X., Jiang, W., Luo, S., Yang, X., Wang, C., Wang, B., Dang, Y., Shen, Y., Ma, D.K.,
1472 2021. The C. elegans homolog of human panic-disorder risk gene TMEM132D orchestrates
1473 neuronal morphogenesis through the WAVE-regulatory complex. Mol. Brain 14, 54.
1474 https://doi.org/10.1186/s13041-021-00767-w
1475 Weeds, A., Maciver, S., 1993. F-actin capping proteins. Curr. Opin. Cell Biol. 5, 63–69.
1476 https://doi.org/10.1016/S0955-0674(05)80009-2
1477 Wu, S., Zhang, Y., 2007. LOMETS: a local meta-threading-server for protein structure
1478 prediction. Nucleic Acids Res. 35, 3375–3382. https://doi.org/10.1093/nar/gkm251
1479 Xing, G., Li, M., Sun, Y., Rui, M., Zhuang, Y., Lv, H., Han, J., Jia, Z., Xie, W., 2018. Neurexin–
1480 neuroligin 1 regulates synaptic morphology and functions via the WAVE regulatory
1481 complex in Drosophila neuromuscular junction. Elife 7, 1–23.
1482 https://doi.org/10.7554/eLife.30457
1483 Yamazaki, D., Fujiwara, T., Suetsugu, S., Takenawa, T., 2005. A novel function of WAVE in

lamellipodia: WAVE1 is required for stabilization of lamellipodial protrusions during cell spreading. Genes Cells 10, 381–392. https://doi.org/10.1111/j.1365-2443.2005.00845.x

Yan, Z., Kim, E., Datta, D., Lewis, D.A., Soderling, S.H., 2016. Synaptic Actin Dysregulation, a Convergent Mechanism of Mental Disorders? J. Neurosci. 36, 11411–11417. https://doi.org/10.1523/jneurosci.2360-16.2016

Yokoyama, K., Tezuka, T., Kotani, M., Nakazawa, T., Hoshina, N., Shimoda, Y., Kakuta, S., Sudo, K., Watanabe, K., Iwakura, Y., Yamamoto, T., 2011. NYAP: A phosphoprotein family that links PI3K to WAVE1 signalling in neurons. EMBO J. 30, 4739–4754. https://doi.org/10.1038/emboj.2011.348

Zhao, A., Zhou, R., Gu, Q., Liu, M., Zhang, B., Huang, J., Yang, B., Yao, R., Wang, J., Lv, H., Wang, J., Shen, Y., Wang, H., Chen, X., 2021. Trio exome sequencing identified a novel de novo WASF1 missense variant leading to recurrent site substitution in a Chinese patient with developmental delay, microcephaly, and early-onset seizures: a mutational hotspot p.Trp161 and literature review. Clin. Chim. Acta. https://doi.org/10.1016/j.cca.2021.08.030

Zhao, B., Meka, D.P., Scharrenberg, R., König, T., Schwanke, B., Kobler, O., Windhorst, S., Kreutz, M.R., Mikhaylova, M., Calderon de Anda, F., 2017. Microtubules Modulate F-actin Dynamics during Neuronal Polarization. Sci. Rep. 7, 9583. https://doi.org/10.1038/s41598-017-09832-8

Zhou, P., Wagner, G., 2010. Overcoming the solubility limit with solubility-enhancement tags: successful applications in biomolecular NMR studies. J. Biomol. NMR 46, 23–31. https://doi.org/10.1007/s10858-009-9371-6

Zou, W., Dong, X., Broederdorf, T.R., Shen, A., Kramer, D.A., Shi, R., Liang, X., Miller, D.M., Xiang, Y.K., Yasuda, R., Chen, B., Shen, K., 2018. A Dendritic Guidance Receptor Complex Brings Together Distinct Actin Regulators to Drive Efficient F-Actin Assembly and Branching. Dev. Cell 45, 362-375.e3. https://doi.org/10.1016/j.devcel.2018.04.008

Zou, W., Shen, A., Dong, X., Tugizova, M., Xiang, Y.K., Shen, K., 2016. A multi-protein receptor-ligand complex underlies combinatorial dendrite guidance choices in C. elegans. Elife 5, 1–25. https://doi.org/10.7554/elife.18345

Zweier, M., Begemann, A., McWalter, K., Cho, M.T., Abela, L., Banka, S., Behring, B., Berger, A., Brown, C.W., Carneiro, M., Chen, J., Cooper, G.M., Finnila, C.R., Guillen Sacoto, M.J., Henderson, A., Hüffmeier, U., Joset, P., Kerr, B., Lesca, G., Leszinski, G.S., McDermott,

J.H., Meltzer, M.R., Monaghan, K.G., Mostafavi, R., Õunap, K., Plecko, B., Powis, Z., Purcarin, G., Reimand, T., Riedhammer, K.M., Schreiber, J.M., Sirsi, D., Wierenga, K.J., Wojcik, M.H., Papuc, S.M., Steindl, K., Sticht, H., Rauch, A., 2019. Spatially clustering de novo variants in CYFIP2, encoding the cytoplasmic FMRP interacting protein 2, cause intellectual disability and seizures. Eur. J. Hum. Genet. 27, 747–759. https://doi.org/10.1038/s41431-018-0331-z

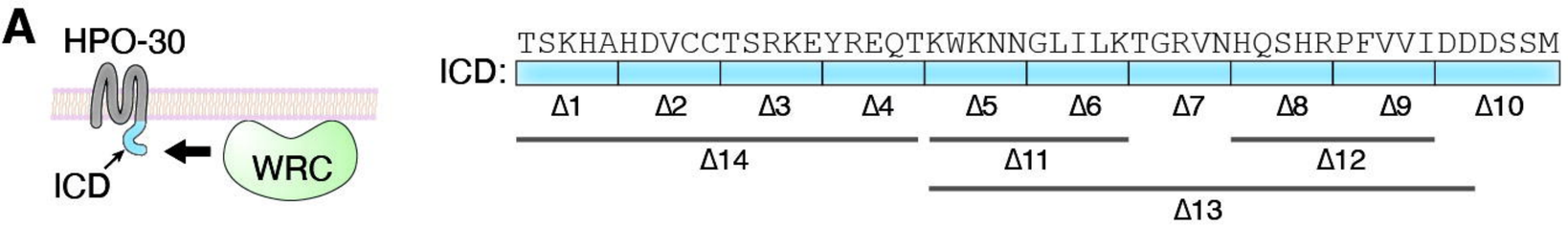

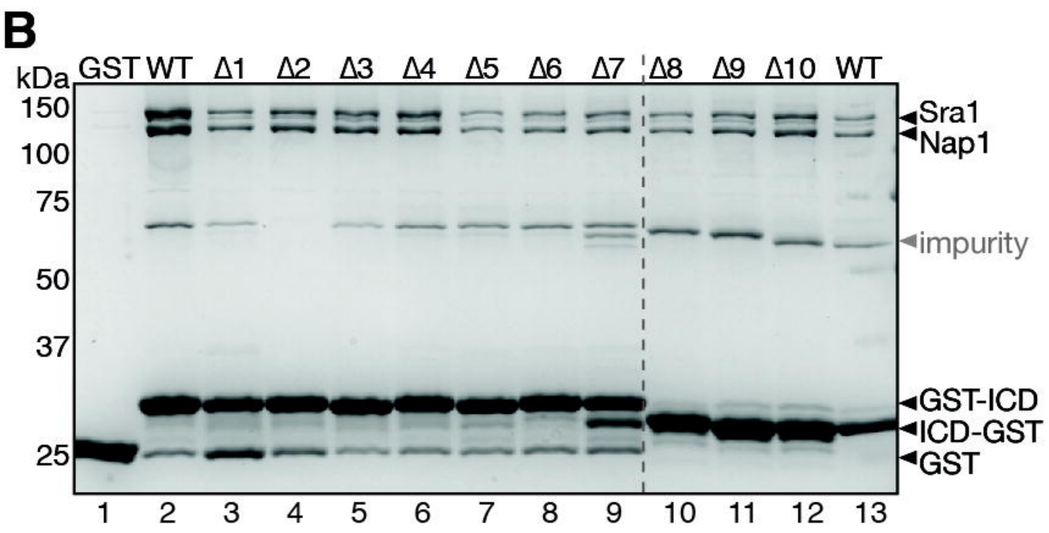

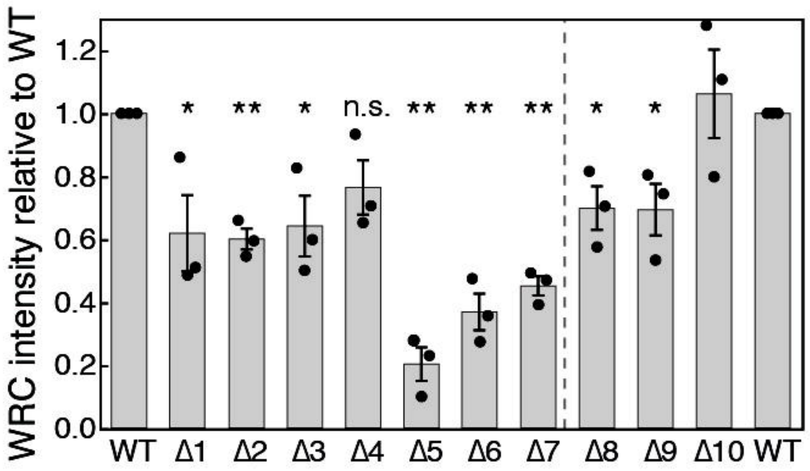

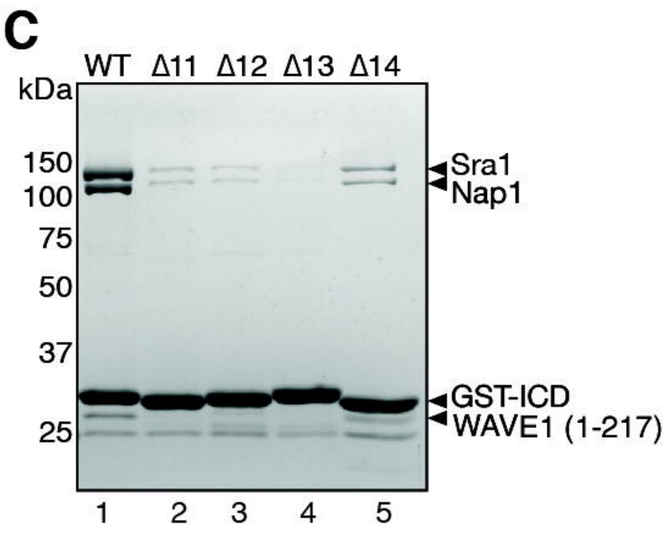

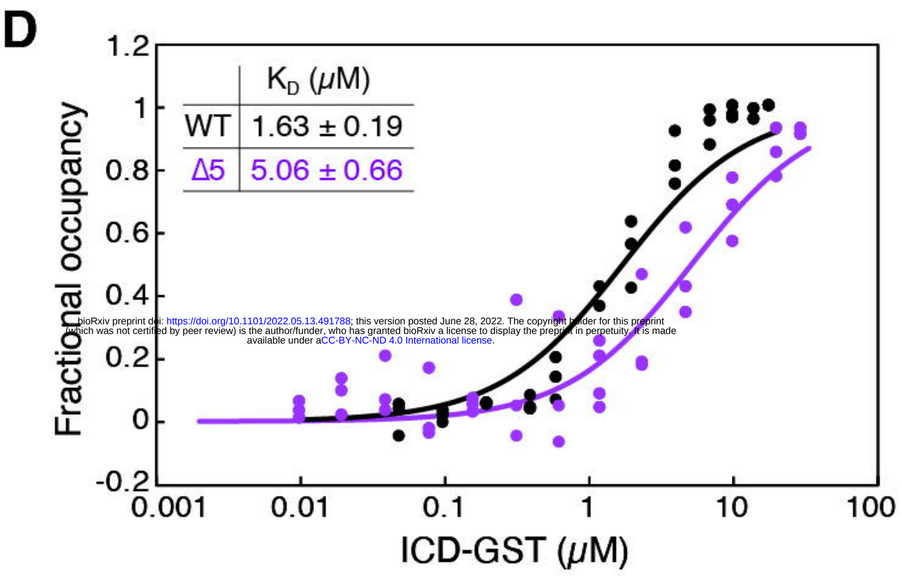

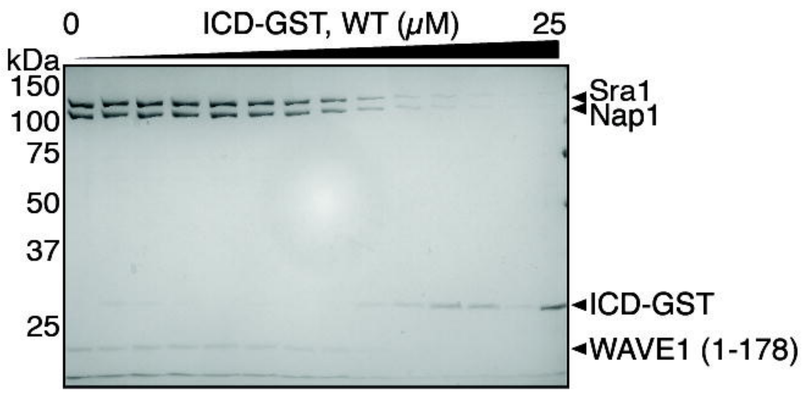

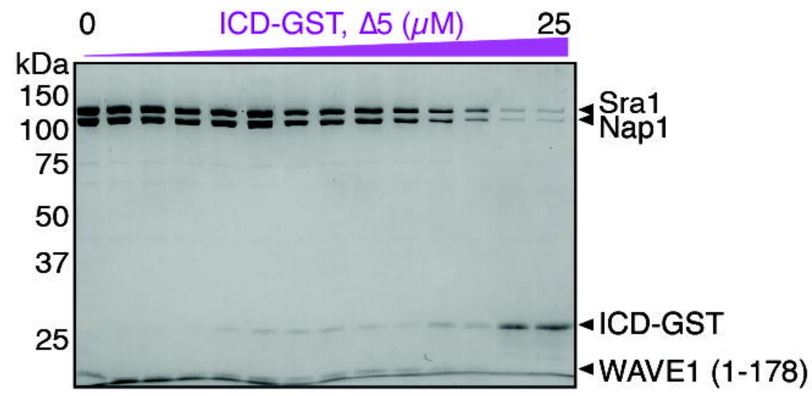

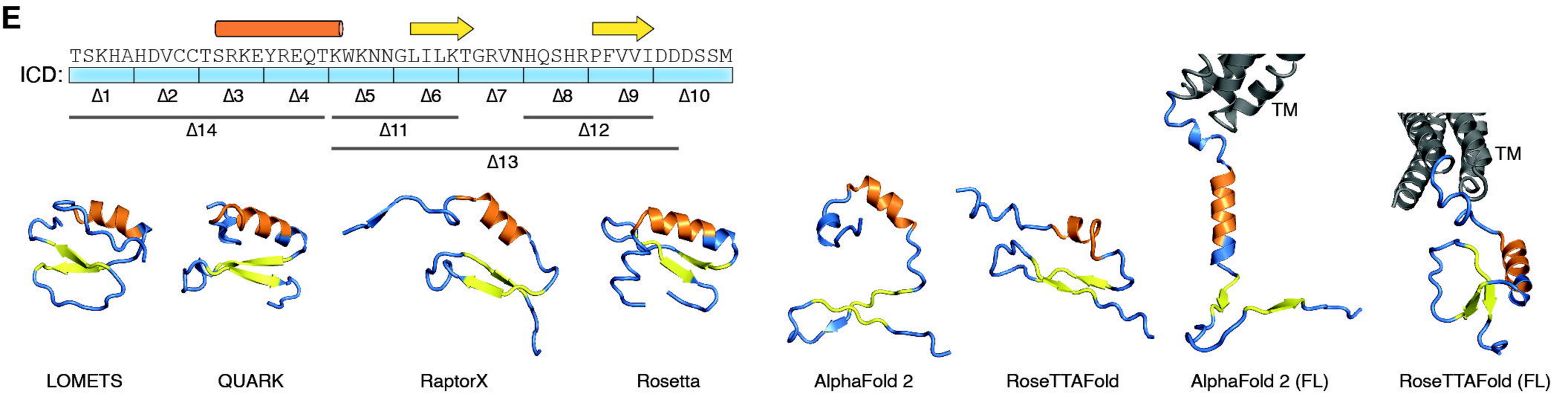

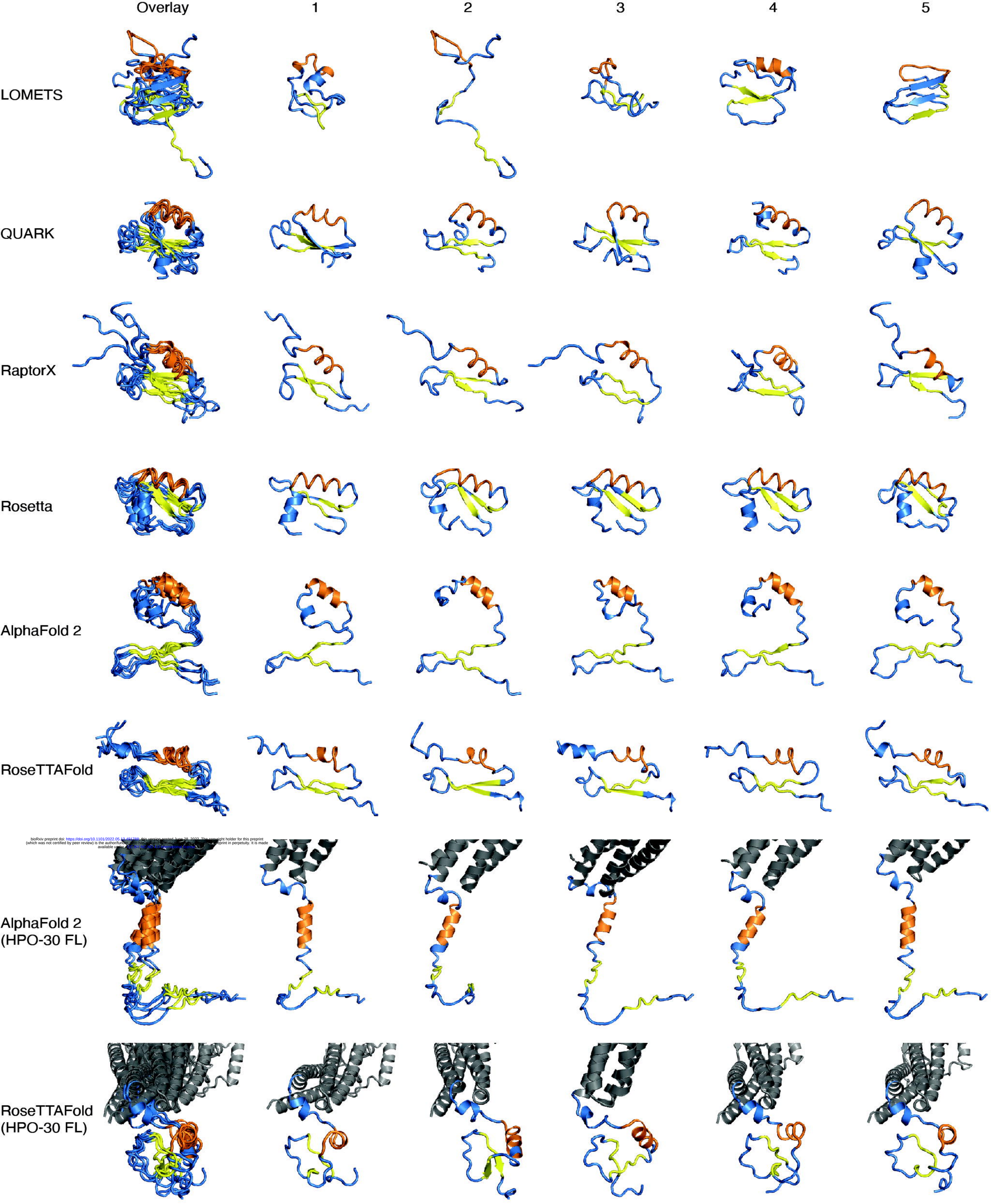

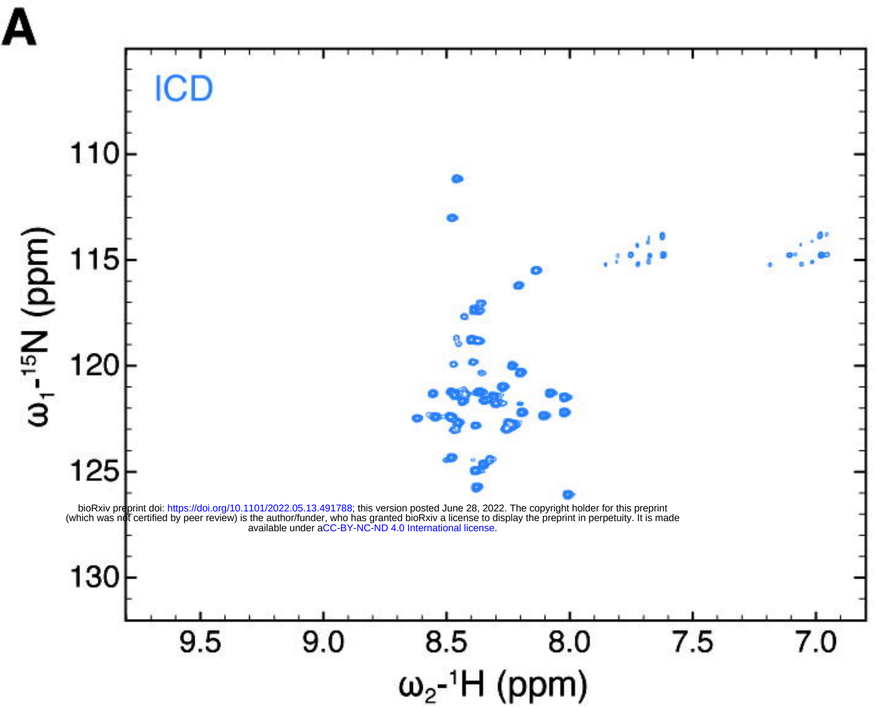

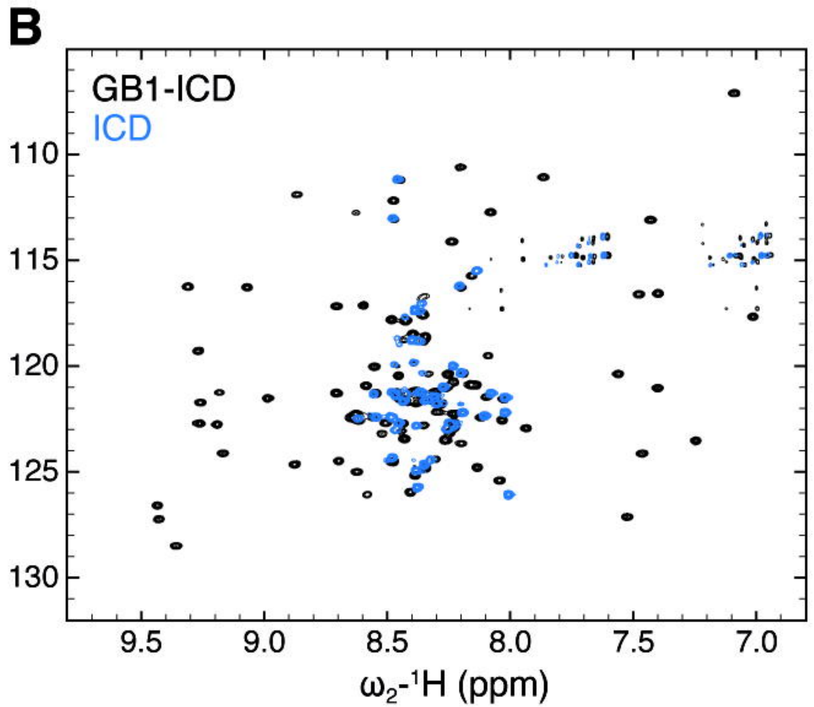

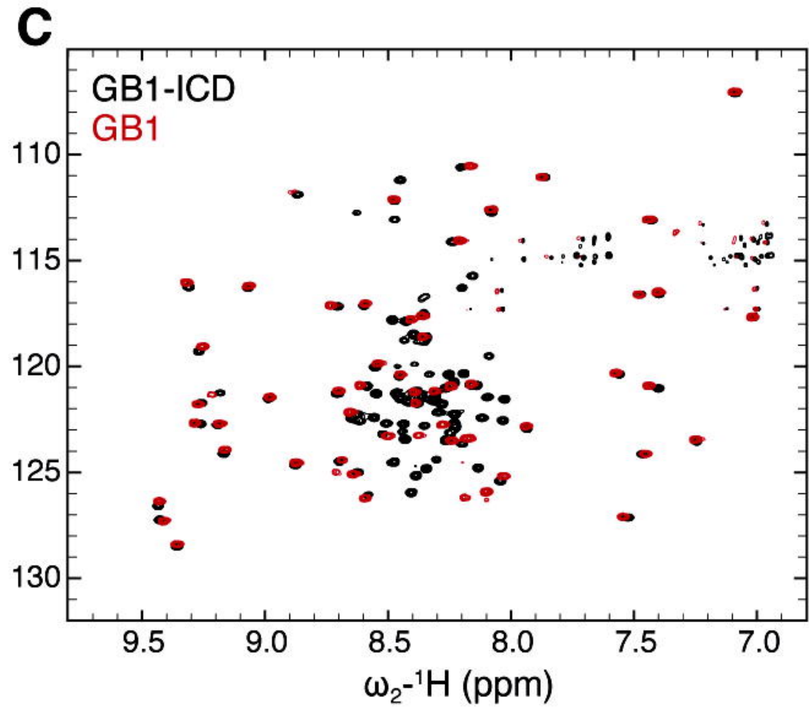

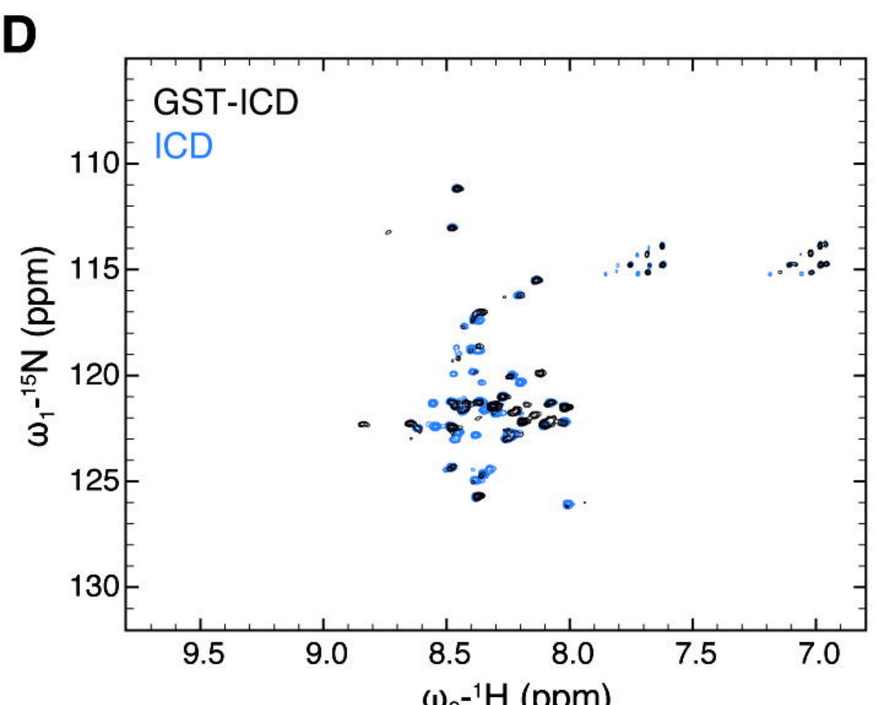

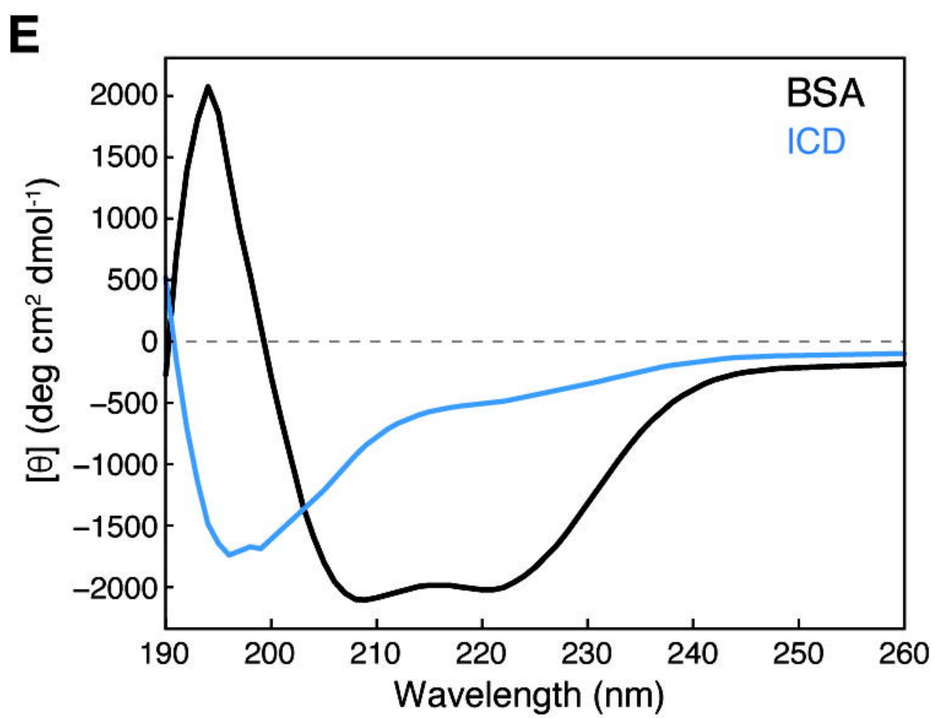

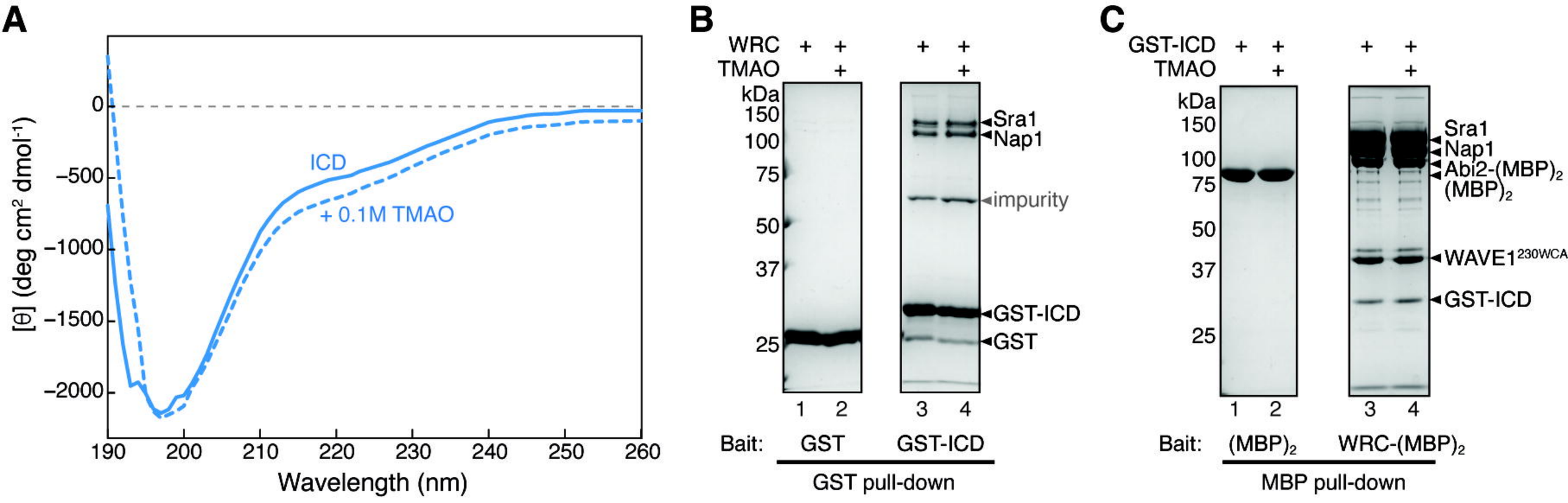
A
0
−500
−1000
−1500
−2000
[θ] (deg cm² dmol⁻¹)
ICD
+ 0.1M TMAO
190
200
210
220
230
240
250
260
Wavelength (nm)
B
WRC + +
TMAO +
kDa
150
100
75
50
37
25
Sra1
Nap1
impurity
GST-ICD
GST
1 2 3 4
Bait: GST GST-ICD
GST pull-down
C
GST-ICD + +
TMAO +
kDa
150
100
75
50
37
25
Sra1
Nap1
Abi2-(MBP)2
(MBP)2
WAVE1230WCA
GST-ICD
1 2 3 4
Bait: (MBP)2 WRC-(MBP)2
MBP pull-down

A

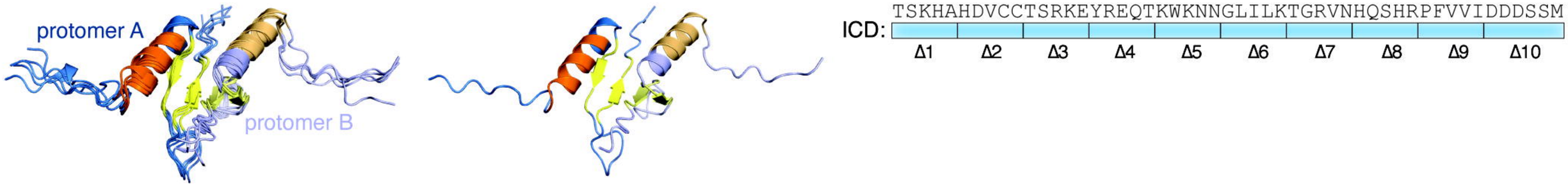

B

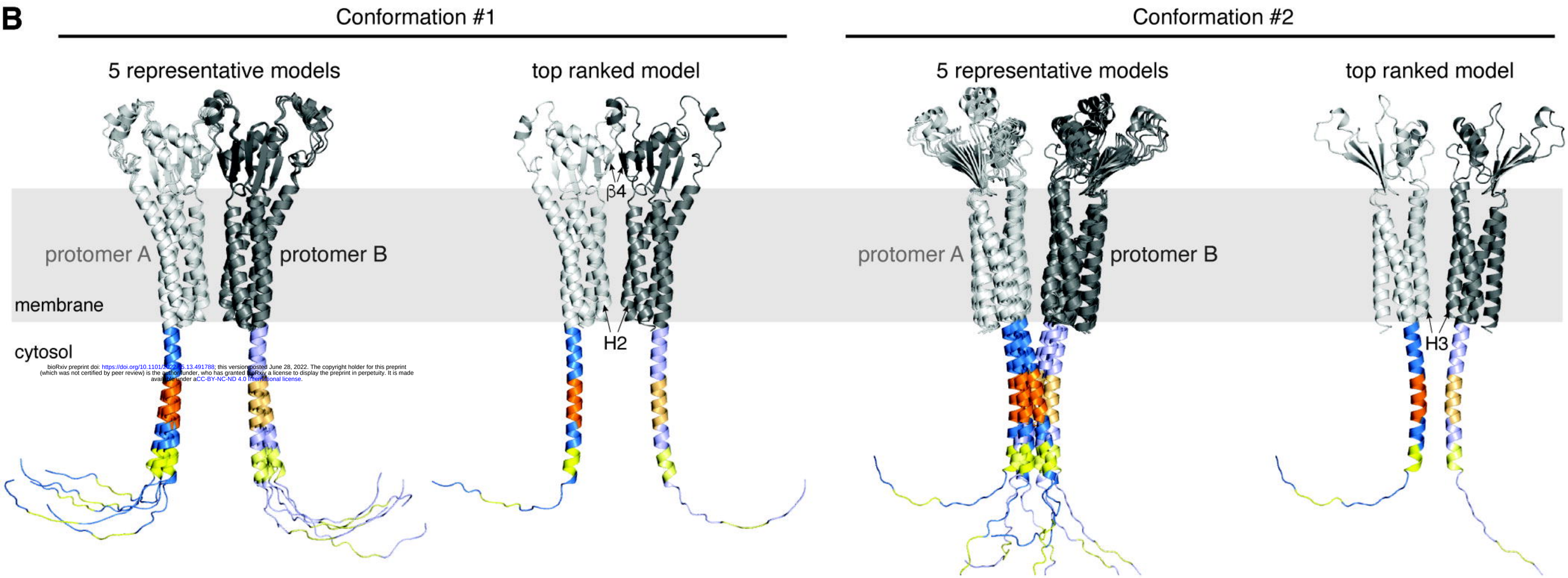

C

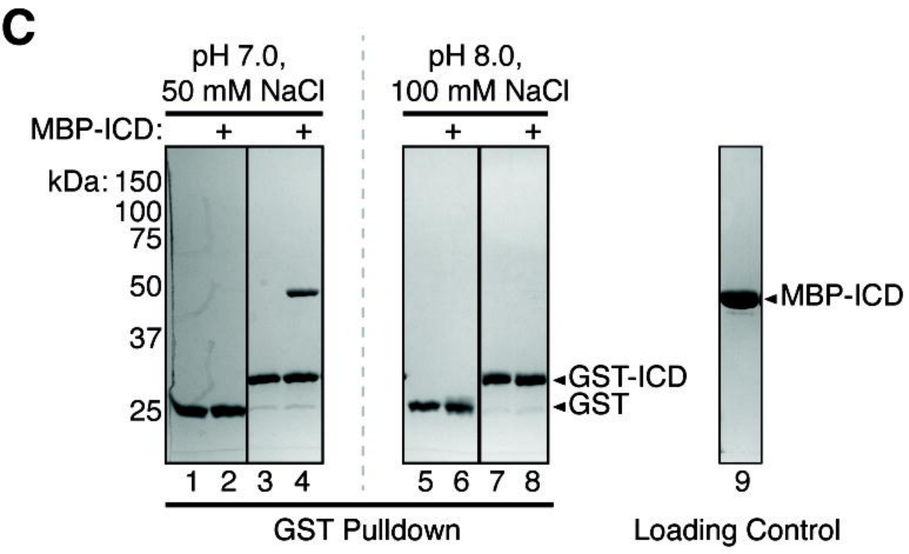

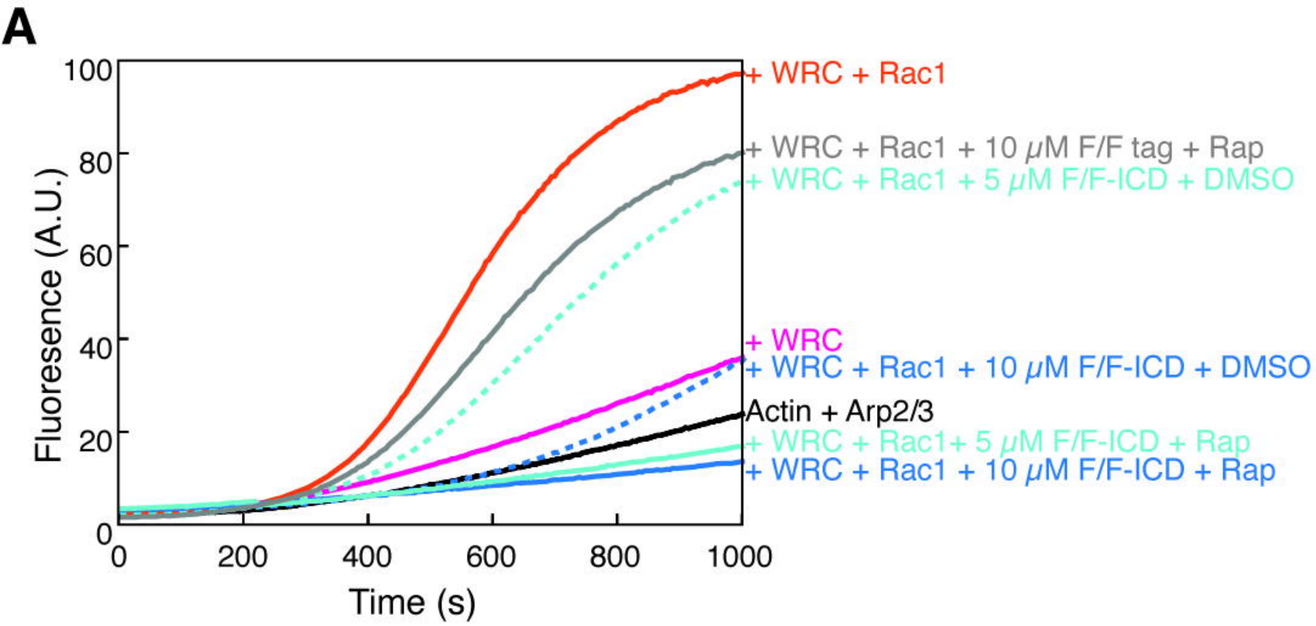

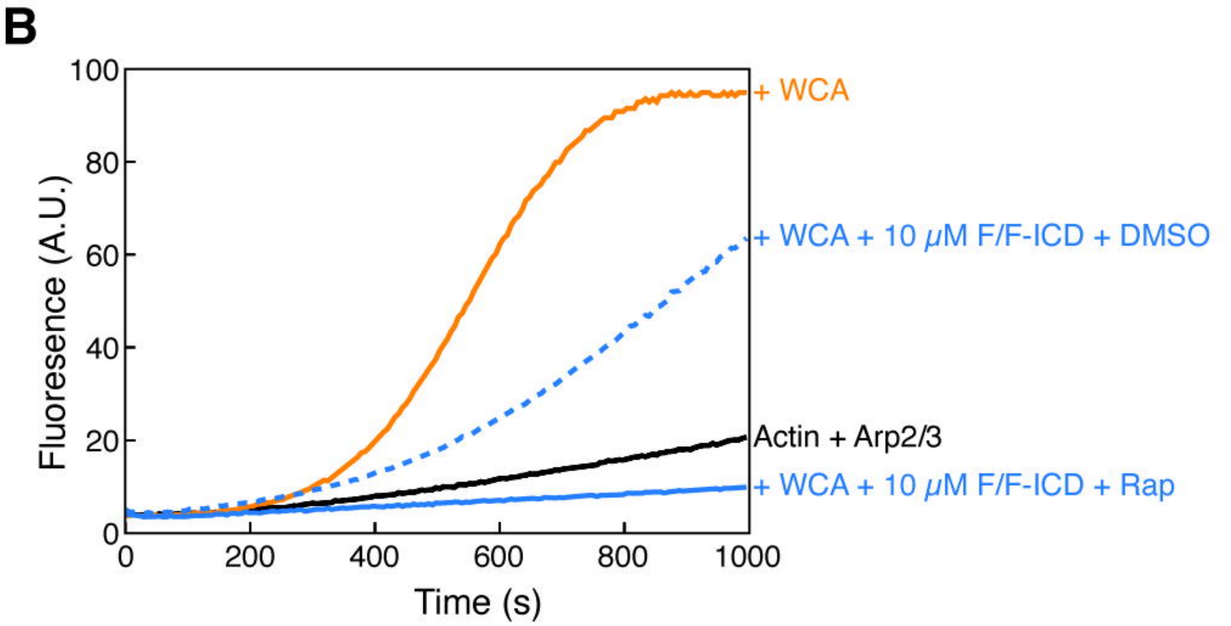

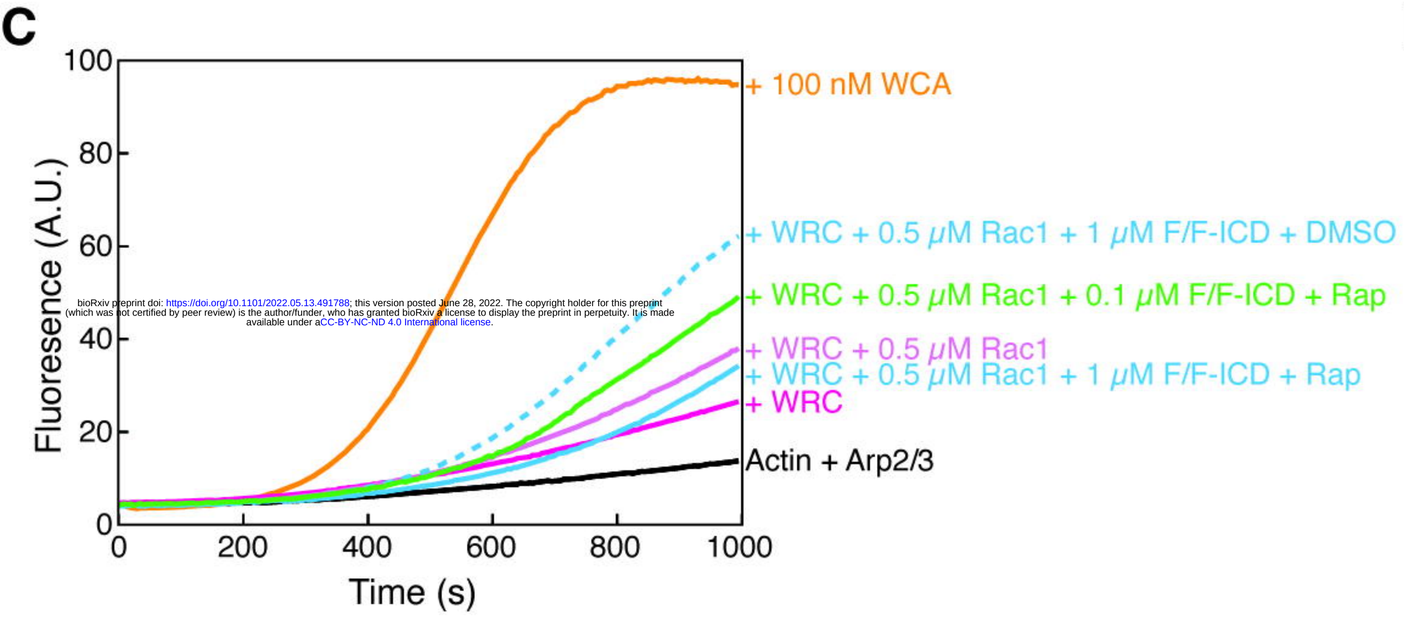

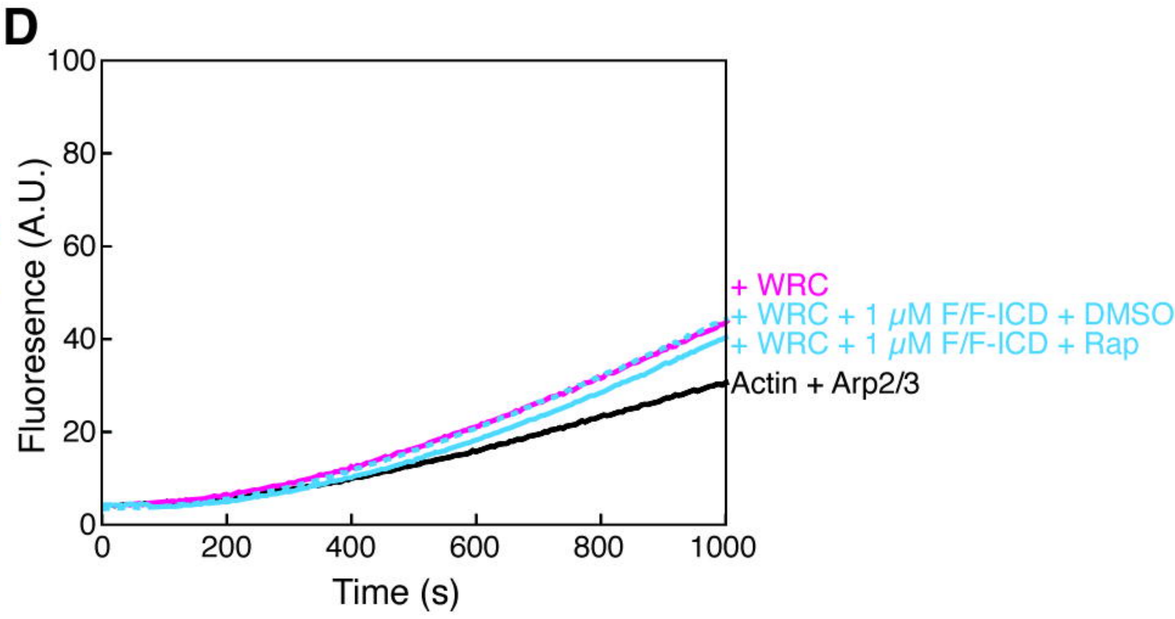

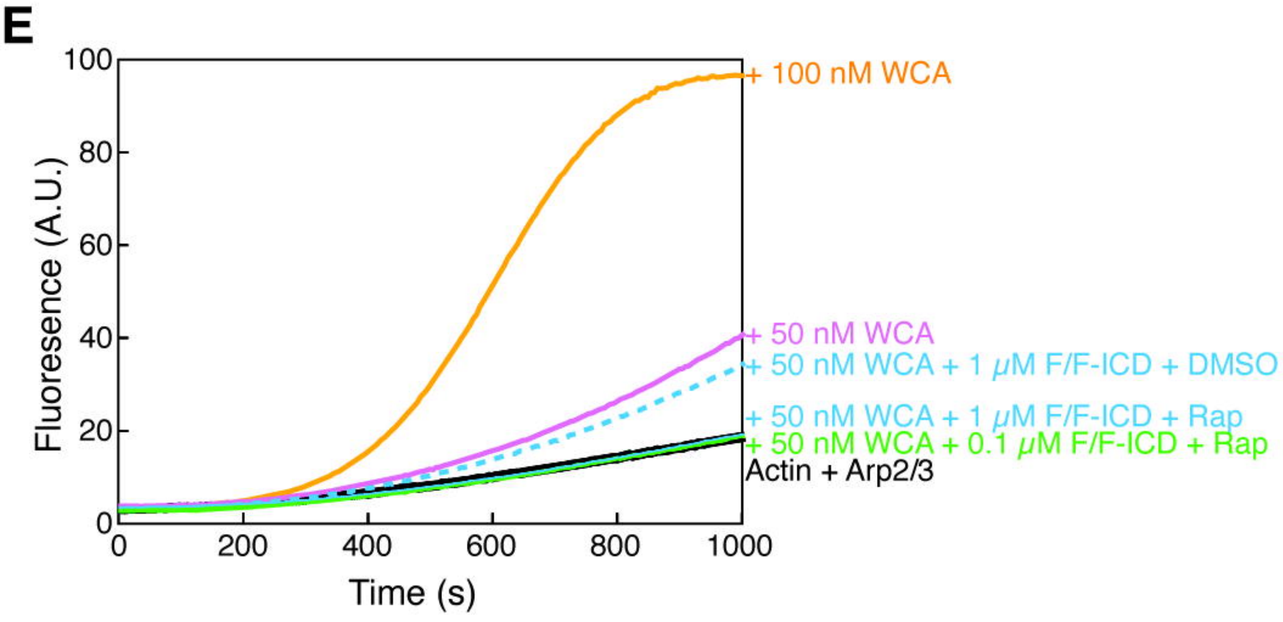

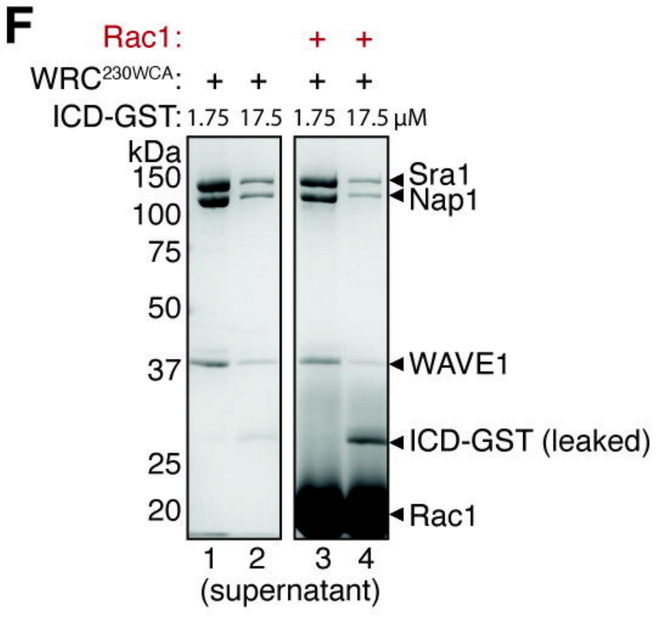

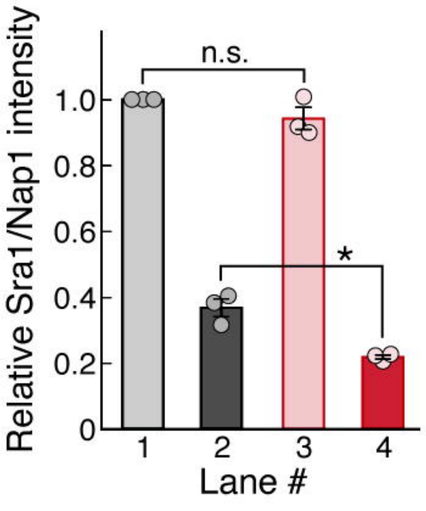

A

Buffer: (all pH 7.0 and containing 1 mM $MgCl_2$, 1 mM EGTA, 1 mM DTT)

50PDB	50PDB20G	50PDBI	50PDBI20G	50KMEI20G	50KMEI5G	50KMEH20G	50KMEH5G
10 mM HEPES 50 mM NaCl 5% glycerol	10 mM HEPES 50 mM NaCl 20% glycerol	10 mM Imidazole 50 mM NaCl 5% glycerol	10 mM Imidazole 50 mM NaCl 20% glycerol	10 mM Imidazole 50 mM KCl 20% glycerol	10 mM Imidazole 50 mM KCl 5% glycerol	10 mM HEPES 50 mM KCl 20% glycerol	10 mM HEPES 50 mM KCl 5% glycerol

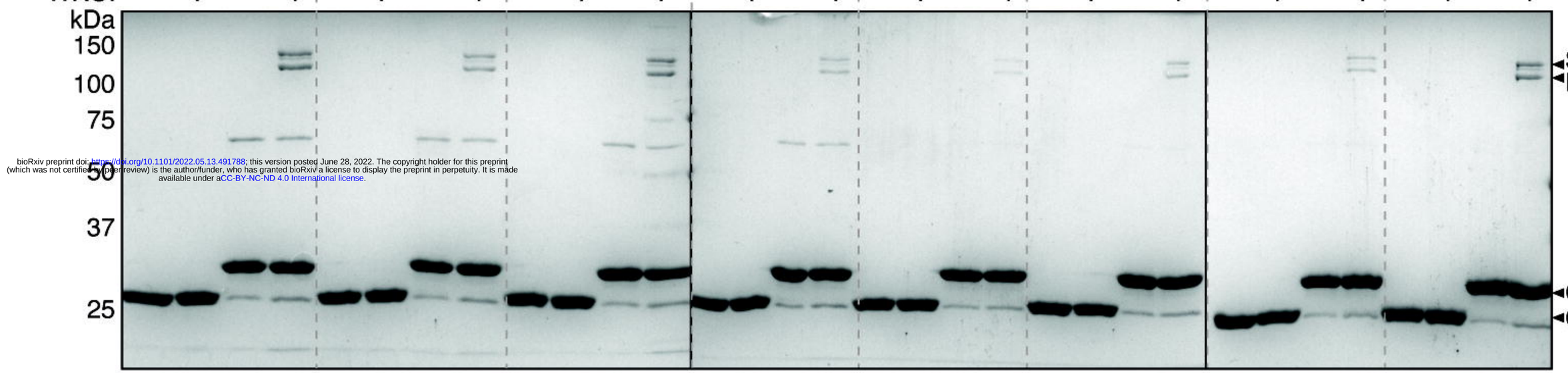

B

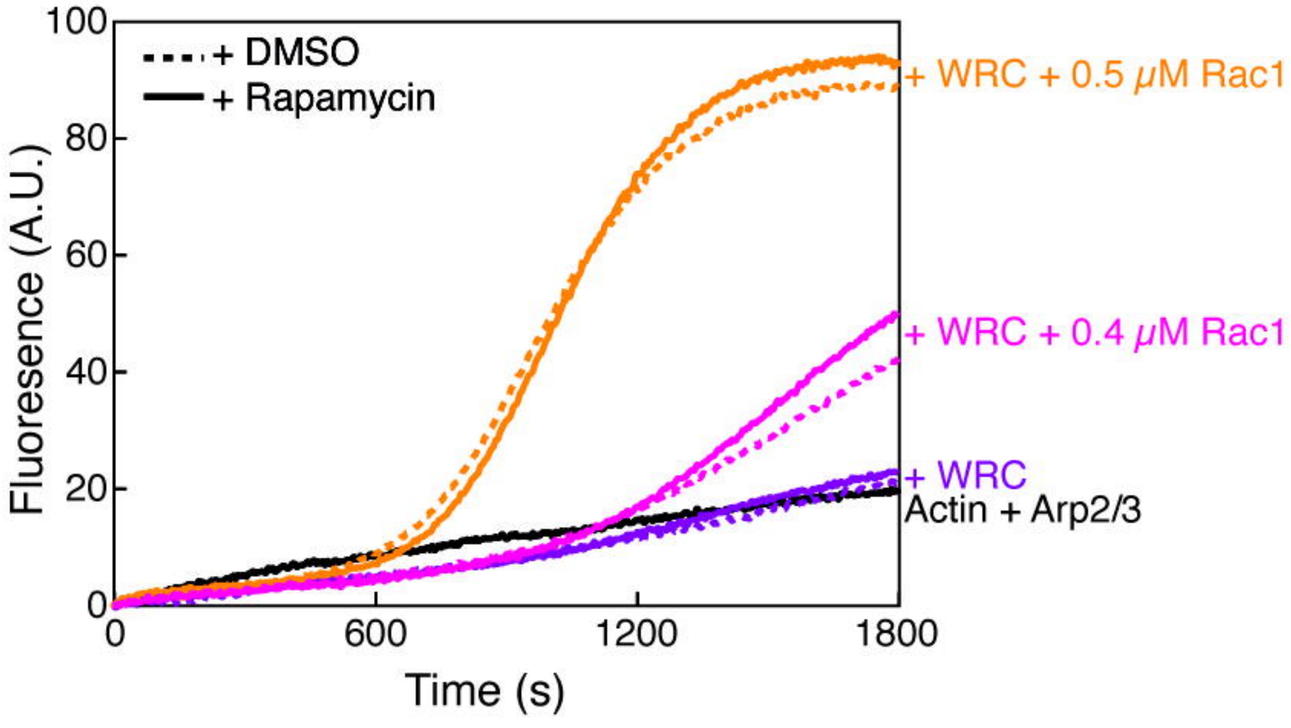

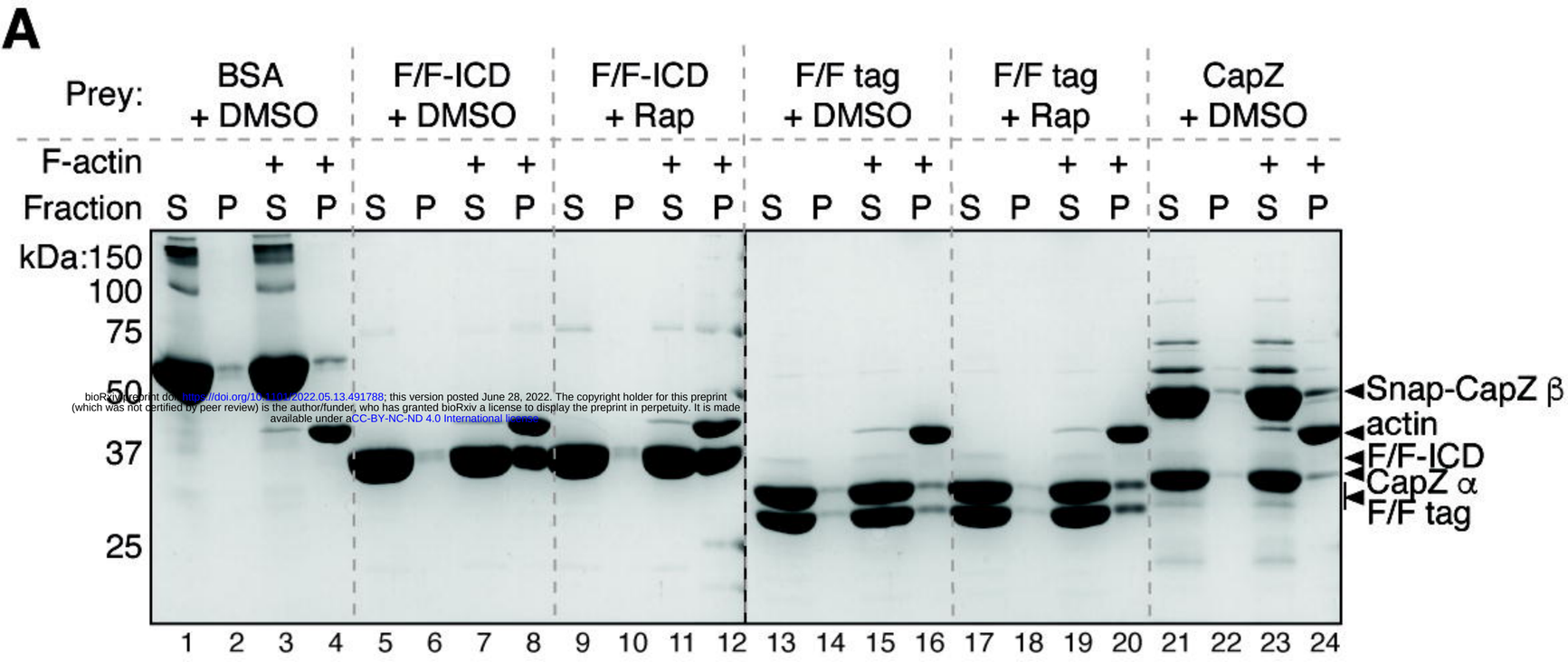

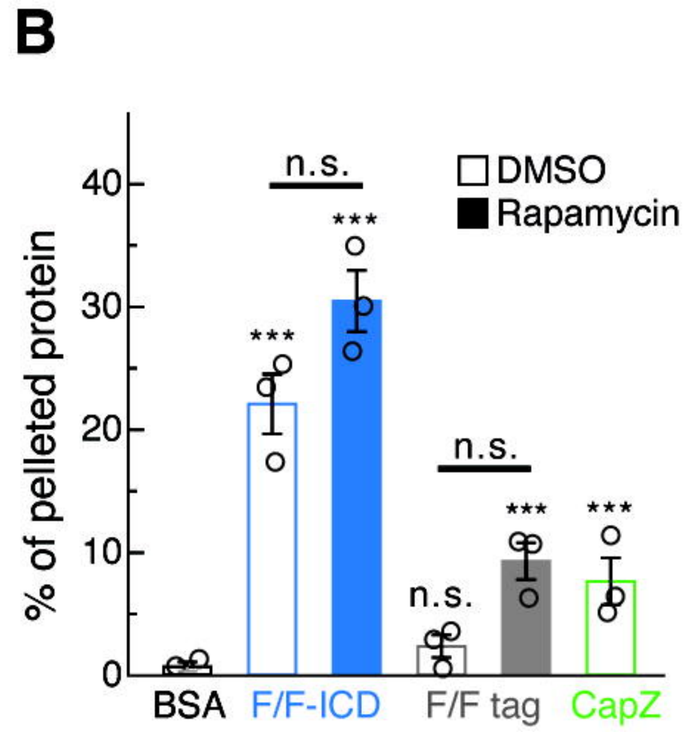

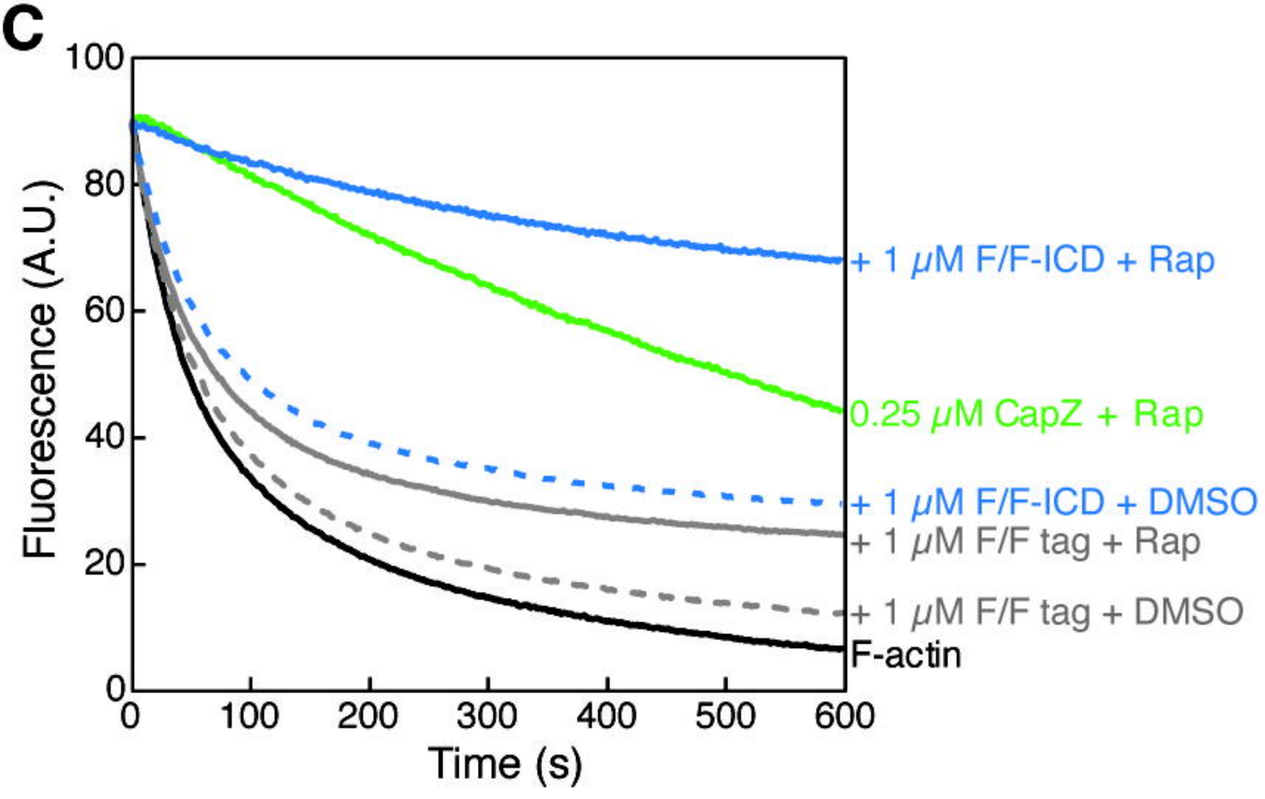

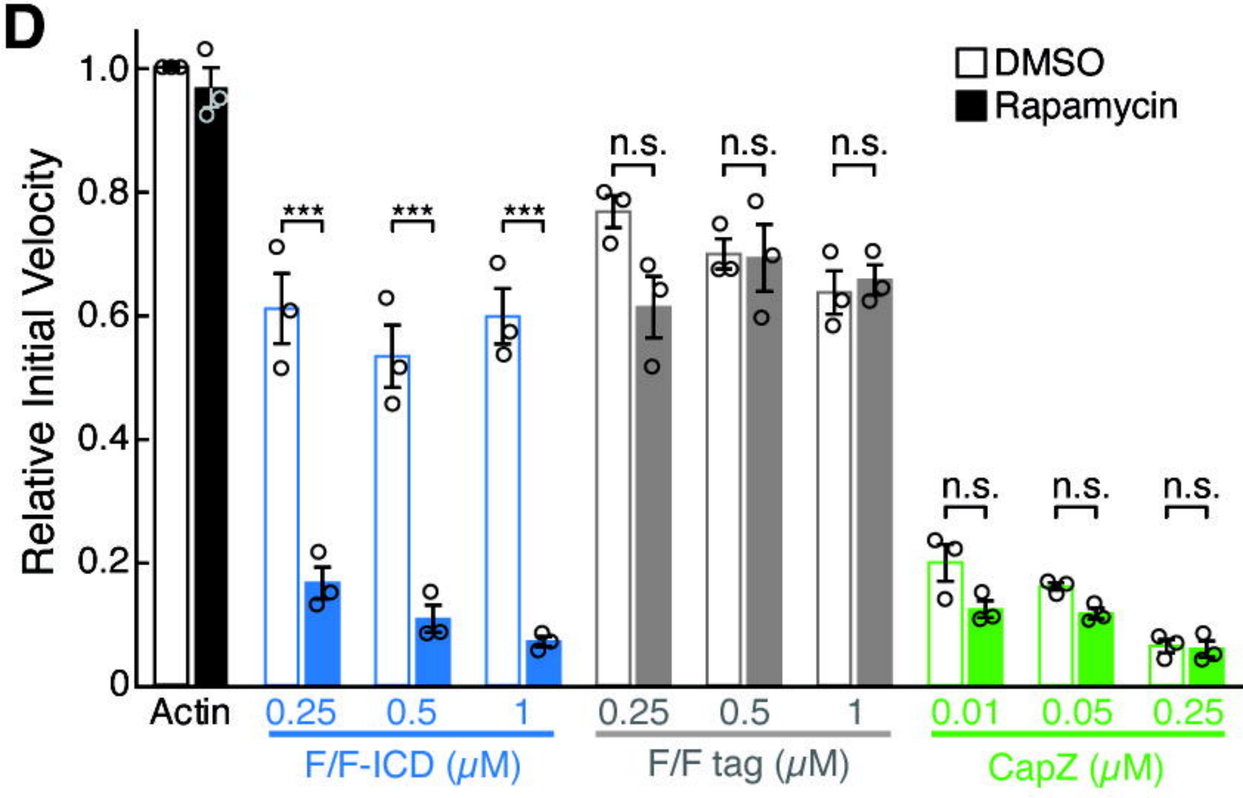

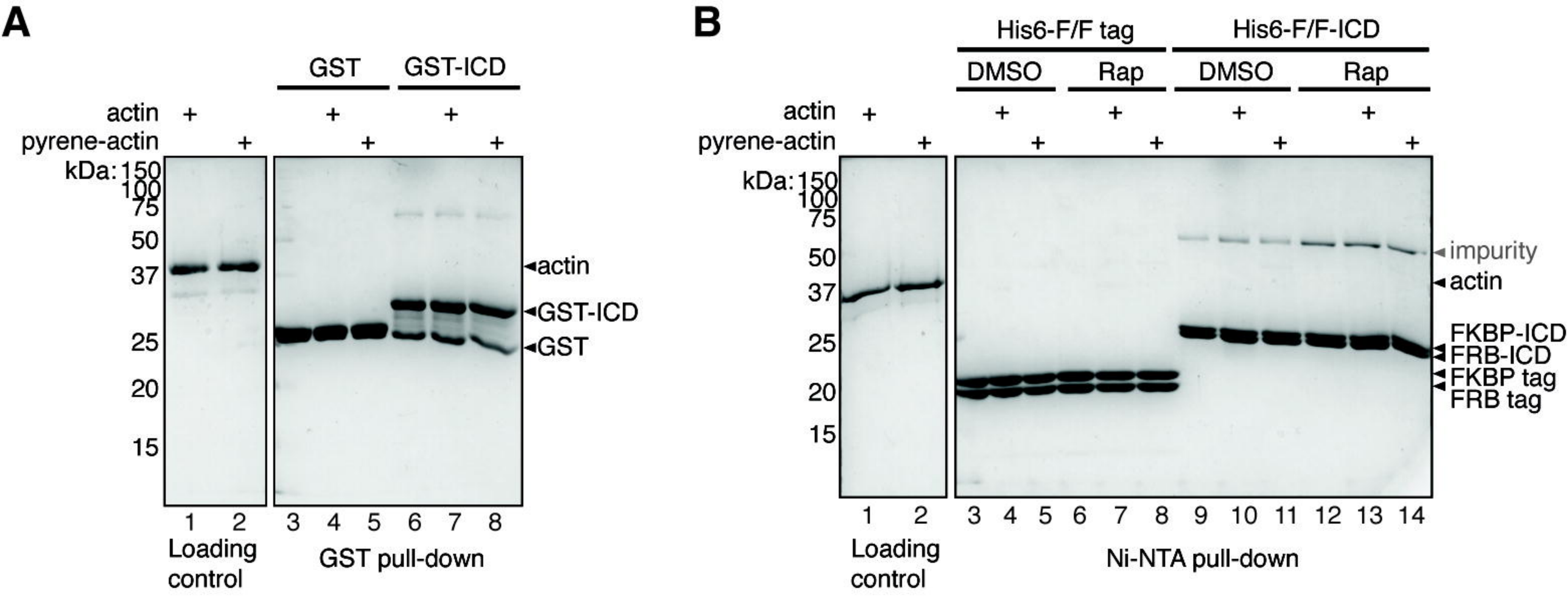
A
GST
GST-ICD
actin
pyrene-actin
kDa:
150
100
75
50
37
25
20
15
actin
GST-ICD
GST
1 2 3 4 5 6 7 8
Loading control
GST pull-down
B
His6-F/F tag
His6-F/F-ICD
DMSO
Rap
DMSO
Rap
actin
pyrene-actin
kDa:
150
100
75
50
37
25
20
15
impurity
actin
FKBP-ICD
FRB-ICD
FKBP tag
FRB tag
1 2 3 4 5 6 7 8 9 10 11 12 13 14
Loading control
Ni-NTA pull-down

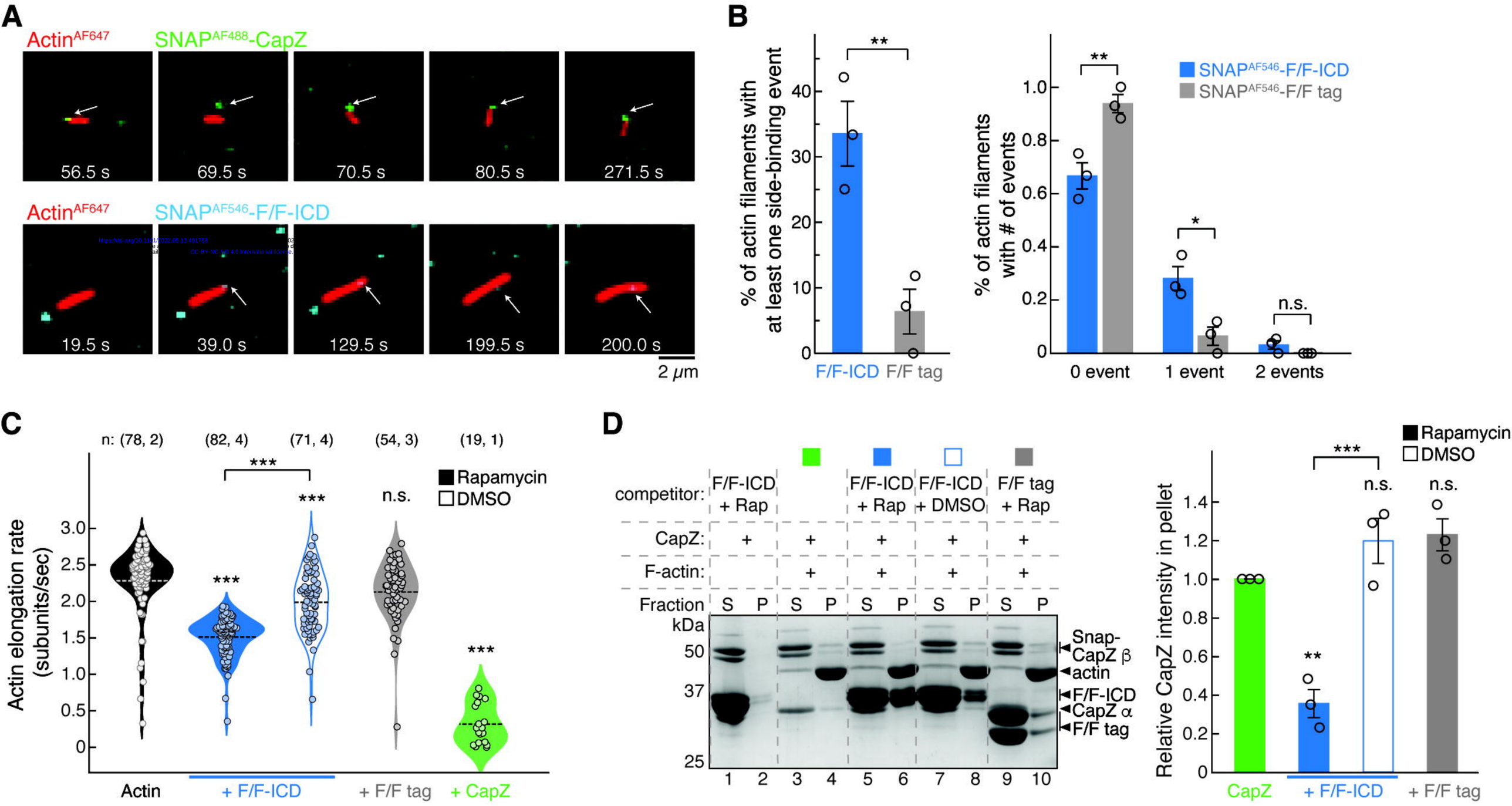
A
Actin^AF647
SNAP^AF488-CapZ
56.5 s
69.5 s
70.5 s
80.5 s
271.5 s
Actin^AF647
SNAP^AF546-F/F-ICD
19.5 s
39.0 s
129.5 s
199.5 s
200.0 s
2 μm
B
% of actin filaments with at least one side-binding event
F/F-ICD
F/F tag
% of actin filaments with # of events
SNAP^AF546-F/F-ICD
SNAP^AF546-F/F tag
0 event
1 event
2 events
n.s.
C
n: (78, 2) (82, 4) (71, 4) (54, 3) (19, 1)
Rapamycin
DMSO
Actin elongation rate (subunits/sec)
Actin
+ F/F-ICD
+ F/F tag
+ CapZ
D
competitor:
F/F-ICD + Rap
F/F-ICD + Rap
F/F-ICD + DMSO
F/F tag + Rap
CapZ:
F-actin:
Fraction
kDa
Snap-CapZ β
actin
F/F-ICD
CapZ α
F/F tag
Relative CapZ intensity in pellet
CapZ
+ F/F-ICD
+ F/F tag

A

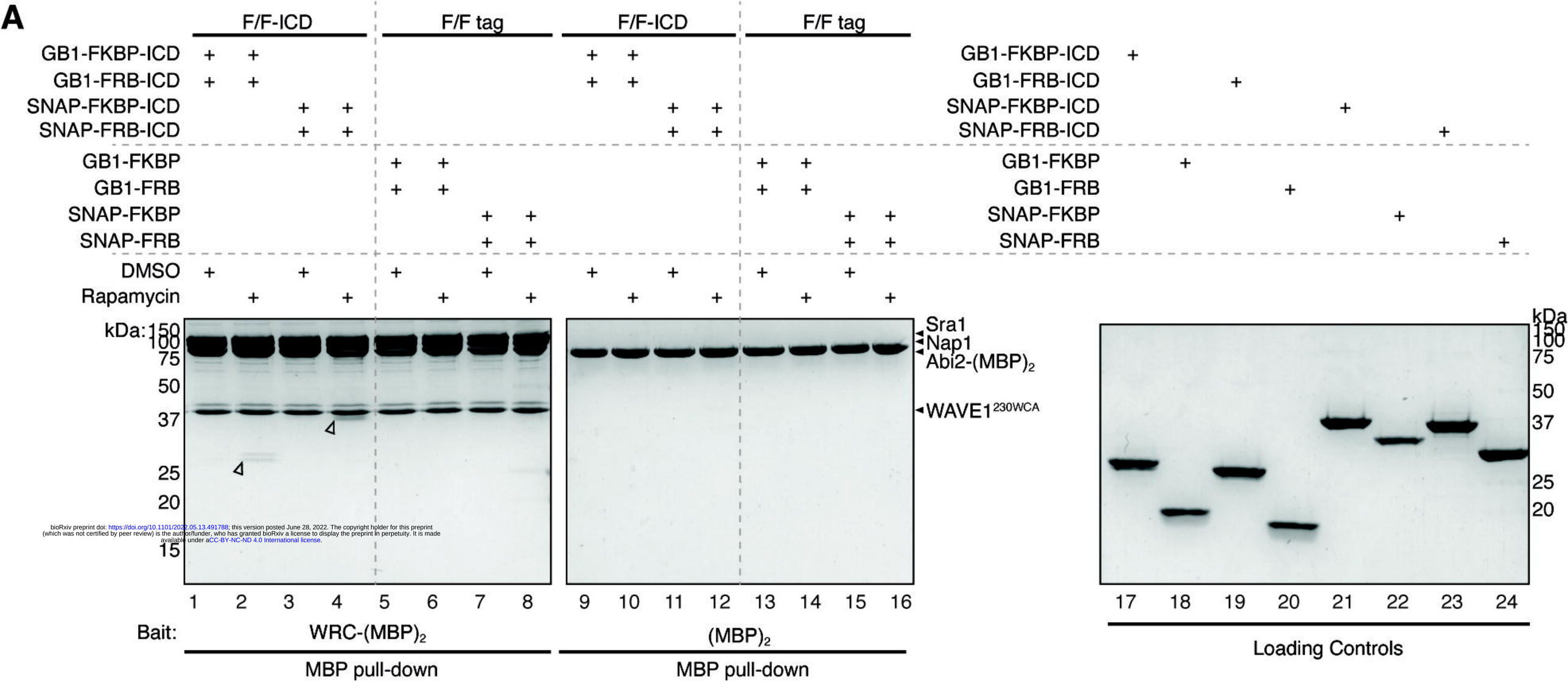

B

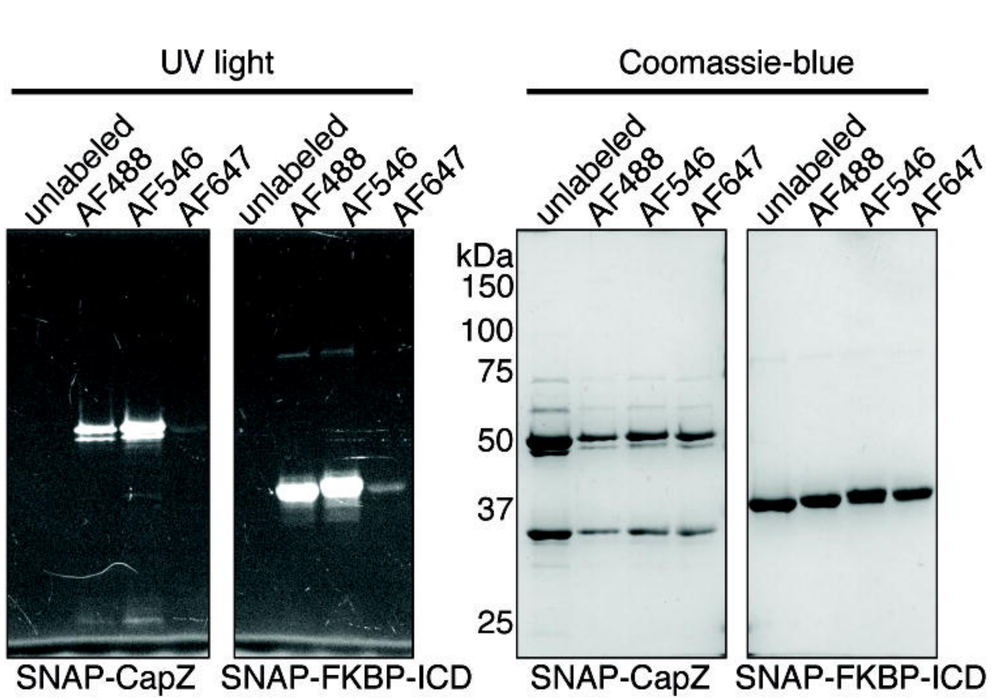

C

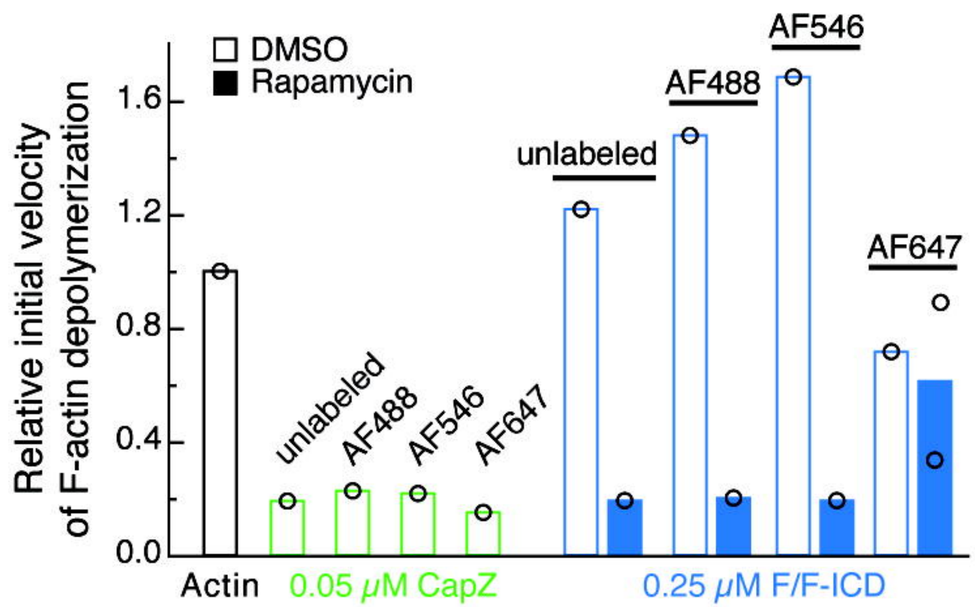

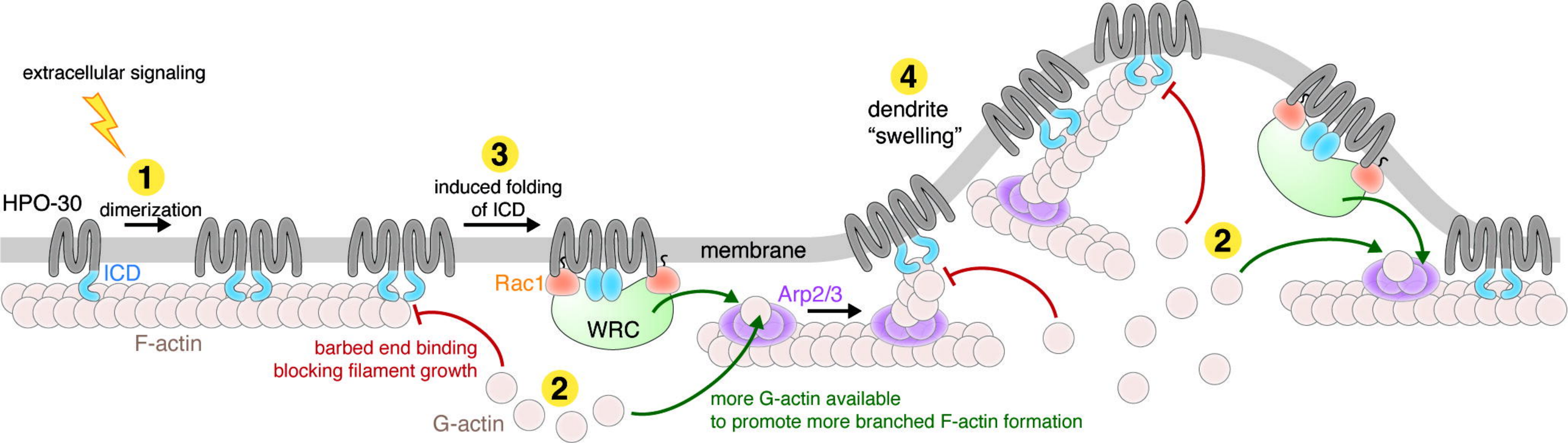
extracellular signaling
1
HPO-30
dimerization
ICD
F-actin
3
induced folding
of ICD
Rac1
WRC
membrane
barbed end binding
blocking filament growth
2
G-actin
Arp2/3
more G-actin available
to promote more branched F-actin formation
4
dendrite
"swelling"
2